Polyacrylonitrile-based Carbon Nanofibers for Gas Adsorption and Separation - Impacts of Thermal Stabilization and KOH Activation

Polyacrylnitrilbasierte Kohlenstoffnanofasern für die Gasadsorption und -trennung - Einflüsse der thermischen Stabilisierung und KOH Aktivierung

Von der Fakultät für Mathematik und Naturwissenschaften der RWTH Aachen University zur Erlangung des akademischen Grades eines Doktors der Naturwissenschaften genehmigte Dissertation

vorgelegt von

Tom Fischer, M.Sc.

aus

Simmerath

Berichter:
Univ.-Prof. Dr. rer. nat. Rüdiger-A. Eichel
Univ.-Prof. Dr.-Ing. Matthias Wessling

Tag der mündlichen Prüfung: 19.12.2025

Diese Dissertation ist auf den Internetseiten der Universitätsbibliothek verfügbar.

Eidesstattliche Erklärung

Ich, Tom Fischer, erkläre hiermit, dass diese Dissertation und die darin dargelegten Inhalte meine eigenen sind und selbständig, als Ergebnis der eigenen originären Forschung, generiert wurden.

Hiermit erkläre ich an Eides statt

1. Diese Arbeit wurde vollständig oder größtenteils in der Phase als Doktorand dieser Fakultät und Universität erbracht;
2. Sofern irgendein Bestandteil dieser Dissertation zuvor für einen akademischen Abschluss oder eine andere Qualifikation an dieser oder einer anderen Institution verwendet wurde, wurde dies klar angezeigt;
3. Wenn immer andere eigene oder die Veröffentlichungen Dritter herangezogen wurden, wurden diese klar benannt;
4. Wenn aus anderen eigenen oder den Veröffentlichungen Dritter zitiert wurde, wurde stets die Quelle hierfür angegeben. Diese Dissertation ist vollständig meine eigene Arbeit, mit der Ausnahme solcher Zitate;
5. Alle wesentlichen Quellen von Unterstützung wurden benannt;
6. Wenn immer ein Teil dieser Dissertation auf der Zusammenarbeit mit anderen basiert, wurde von mir klar gekennzeichnet, was von anderen und was von mir selbst erarbeitet wurde;
7. Ein Teil dieser Arbeit wurde zuvor veröffentlicht. Eine Übersicht der Veröffentlichungen findet sich auf Seite III;

Ort, Datum Tom Fischer

Publications

Parts of this thesis were previously published in the following publications:

- **Post-Treatment Strategies for Pyrophoric KOH-activated Carbon Nanofibres**

  Tom Fischer, Ansgar Kretzschmar, Victor Selmert, Sven Jovanovic, Hans Kungl, Hermann Tempel and Rüdiger-A. Eichel, RSC Adv., 2024, **14**, 3845

  As first author T. Fischer developed the concept of the study in close collaboration with A. Kretzschmar. T. Fischer conducted the experiments and the data processing. He drafted the manuscript and edited it during the internal review. S. Jovanovic conducted the Raman measurements. All co-authors were involved in manuscript discussion and proof-reading.

- **The Impact of Thermal Stabilization Temperature and Duration on the Pore Structure of Polyacrylonitrile-based Carbon Nanofibers**

  Tom Fischer, Maya Pagel, Ansgar Kretzschmar, Victor Selmert, Hans Kungl, Hermann Tempel and Rüdiger-A. Eichel, Carbon Trends, 2025, **21**, 100559

  T. Fischer conceptualized the study and conducted parts of the experimental work as well as parts of the data evaluation. During her Master thesis under guidance of T. Fischer, M. Pagel conducted main parts of the experimental work and contributed to the data evaluation. T. Fischer drafted and edited the manuscript during the internal review. All co-authors were involved in discussion of the results and reviewing of the manuscript.

Danksagung

Zur erfolgreichen Umsetzung dieser Dissertation haben eine Vielzahl an Menschen auf verschiedene Weise beigetragen.
Ein großer Dank gilt meinem Doktorvater Prof. Rüdiger-A. Eichel für die Möglichkeit meine interessante Forschung an seinem Institut durchführen zu können und Prof. Matthias Wessling für die Bereitschaft die Funktion des Zweitgutachters meiner Arbeit zu übernehmen.
Außerdem danke ich unserem Abteilungsleiter Dr. Hermann Tempel und unserem ehemaligen Abteilungsleiter Dr. Hans Kungl für die spannende Arbeit in ihrer Abteilung und ihre fortlaufende Unterstützung.
Mein Interesse an den Gasadsorptionseigenschaften von Kohlenstoffnanofasern ist im Verlauf meiner Masterarbeit entstanden und hat mich zu meiner Doktorarbeit auf diesem Forschungsgebiet bewogen. Während der gesamten Zeit war mein Day-to-Day supervisor Dr. Ansgar Kretzschmar immer ein offener Anlaufpunkt für Fragen, Diskussionen und Unterstützung. Vielen Dank, Ansgar!
Außerdem danke ich meiner Masterandin, Maya Pagel, für ihre hervorragende Arbeit und die Möglichkeit selbst einen Einblick in die Perspektive des Betreuenden zu bekommen.
Natürlich gilt auch allen weiteren Kolleginnen und Kollegen aus der Adsorptionsgruppe ein besonderer Dank für wissenschaftliche Diskussionen, neue Ideen und Unterstützung. Es hat Spaß gemacht mit euch, Ansgar, Victor, Maya, Paula, Niklas, Carl und Sebastian, zusammenzuarbeiten. Neben den Kollegen aus der Gruppe, danke ich auch allen weiteren Kolleginnen und Kollegen im IET-1, die mich immer in wissenschaftlichen, technischen und organisatorischen Fragen unterstützt haben.

Abseits der Hilfe im direkten Arbeitsumfeld, möchte ich mich außerdem bei meinen Eltern bedanken, die mich immer auf meinem Weg unterstützt und begleitet haben. Vielen Dank für eure Unterstützung und die Möglichkeit meinen Weg zu gehen!
Neben meinen Eltern, gilt ein großer Dank meiner Freundin Gina, die mich durch die Hoch- und Tiefphasen dieser Arbeit begleitet hat und immer eine großartige Unterstützung und Motivation gewesen ist.

Abstract

The synthesis of polyacrylonitrile based carbon nanofibers consists of the steps of electrospinning, thermal stabilization, carbonization and frequently an optional activation. This work focusses on the impacts of thermal stabilization and KOH activation on the pore structure and the CO_2 adsorption properties of carbon nanofibers. Thermal stabilization parameters such as duration, temperature and atmosphere are investigated. A significant impact of these on the pore structure and thus the gas adsorption properties of the carbon nanofibers is found. Using several characterization techniques, such as infrared spectroscopy, elemental analysis and Raman spectroscopy, the incorporation of oxygen and the cyclization degree during stabilization are identified as key parameters, which affect the pore structure of the resulting carbon nanofibers.

Besides thermal stabilization, KOH activation is thoroughly studied. Two O_2-flow post-treatment conditions are applied to freshly KOH-activated samples directly after their activation to study potassium oxidation reactions. At high O_2-flow, comparable to ambient air, vigorous oxidation causing an intense carbon combustion reaction is triggered. By application of a low O_2-flow, the potassium oxidation was controlled and the carbon combustion reaction suppressed. Samples treated at low O_2-flow conditions showed a distinct improvement of the gas adsorption properties.

A series of KOH-activated carbon nanofibers at different degrees of activation is synthesized using low O_2-flow post-treatment. The activation conditions result in a significant increase of narrow micropore volume and thus improved gas adsorption properties. The sample series is investigated in dynamic sorption experiments to study the separation of CO_2 in binary CO_2/N_2 mixture at typcial flue gas conditions. For higher KOH:Fiber activation degrees the CO_2 selectivity decreased, resulting in a trade-off between adsorption capacity and selectivity. Besides the selectivity, the working capacity and cycle stability are evaluated in a simplified pressure swing adsorption cycle. All KOH-activated carbon nanofibers showed a sufficient stability and especially the most KOH-activated sample offers a highly improved working capacity compared to the pristine material at high adsorptive pressures.

Overall, the work offers an important contribution to a more profound understanding of the possibilities for tailoring PAN-based carbon nanofibers for gas separation processes.

Zusammenfassung

Die Synthese von Kohlenstoffnanofasern auf Polyacrylnitrilbasis beinhaltet das Elektrospinning, die thermischen Stabilisierung, die Carbonisierung und eine optionale Aktivierung. Diese Arbeit fokussiert sich auf die Auswirkungen der thermischen Stabilisierung und der KOH-Aktivierung auf die Porenstruktur und die CO_2 Adsorptionseigenschaften von Kohlenstoffnanofasern. Es werden die thermischen Stabilisierungsparameter Dauer, Temperatur und Atmosphäre untersucht. Es zeigt sich ein signifikanter Einfluss auf die Porenstruktur und somit die Gasadsorptionseigenschaften der Kohlenstoffnanofasern. Mithilfe verschiedener Charakterisierungsmethoden wie der Elementaranalyse und Infrarot- und Ramanspektroskopie wurden die Sauerstoffaufnahme und der Zyklisierungsgrad während der Stabilisierung als Haupteinflussfaktoren auf die Porenstruktur der Kohlenstoffnanofasern identifiziert. Neben der thermischen Stabilisierung wird auch die Aktivierung mit KOH untersucht. Zwei Nachbehandlungen mit verschiedenen O_2-Flussraten werden direkt im Anschluss an die Aktivierung angewendet, um die Kaliumoxidationsreaktion zu untersuchen. Bei hohen O_2-Flussraten, vergleichbar mit der Umgebungsluft, wird eine starke Oxidationsreaktion beobachtet, die eine intensive Kohlenstoffverbrennungsreaktion verursacht. Bei niedrigen O_2-Flussraten wird die Kaliumoxidation kontrolliert und die Kohlenstoffverbrennungsreaktion unterdrückt. Proben, die bei niedrigem O_2-Fluss behandelt wurden, zeigen deutlich verbesserte Gasadsorptionseigenschaften. KOH-aktivierte Kohlenstoffnanofasern mit unterschiedlichen Aktivierungsgraden wurden mit Nachbehandlung bei niedrigen O_2-Flussraten synthetisiert. Höhere Aktivierungsgrade führen zu einem Anstieg des Mikroporenvolumens und somit verbesserten CO_2 Adsorptionseigenschaften. In dynamischen Sorptionsexperimenten wurde die Abtrennung von CO_2 aus binären CO_2/N_2-Gemischen bei typischen Rauchgaszusammensetzungen untersucht. Bei höheren Aktivierungsgraden nahm die CO_2-Selektivität ab. Dies führt zu einem Kompromiss zwischen Adsorptionskapazität und Selektivität. Die Arbeitskapazität und die Zyklenstabilität sind in einem idealisierten Druckwechseladsorptionszyklus bestimmt worden. Alle KOH-aktivierten Kohlenstoffnanofasern zeigten eine ausreichende Stabilität und insbesondere die am stärksten KOH-aktivierte Probe bietet bei hohen Adsorptionsdrücken eine stark verbesserte Arbeitskapazität. Insgesamt leistet die Arbeit einen wichtigen Beitrag zu einem tieferen Verständnis der Möglichkeiten, PAN-basierte Kohlenstoffnanofasern für Gastrennprozesse maßzuschneidern.

Contents

1. Motivation **1**

2. Fundamentals **3**
2.1. Carbon capture technologies 3
2.2. Solid adsorbents for CO_2 capture 4
2.3. Carbon Nanofiber Synthesis 6
2.3.1. Electrospinning 6
2.3.2. Thermal stabilization 8
2.3.3. Carbonization and Graphitization 10
2.3.4. KOH Activation 11
2.4. Gas adsorption fundamentals 13
2.4.1. Terminology and pore classification 13
2.4.2. Physisorption isotherms 15
2.4.3. Isotherm models 16
2.4.4. Pore size analysis 18
2.4.5. Ideal Adsorbed Solution Theory 19
2.4.6. Isosteric enthalpy of adsorption 21
2.4.7. Static gas adsorption experiments 21
2.4.8. Dynamic sorption experiments 22

3. Scope of thesis **27**

4. Experimental **29**
4.1. Synthesis of pristine carbon nanofibers 29
4.2. Synthesis of KOH-activated carbon nanofibers 30
4.2.1. Synthesis of reference materials 32
4.3. Characterization of the carbon nanofibers 32
4.3.1. Elemental analysis 32
4.3.2. Simultaneous thermal analysis 33
4.3.3. Infrared spectroscopy 33

4.3.4. Raman spectroscopy 34
4.3.5. ICP-OES 35
4.3.6. Electron microscopy 35
4.3.7. Static gas adsorption 35
4.3.8. Dynamic gas adsorption 37

5. Impact of the thermal stabilization parameters on the pore structure of carbon nanofibers 41
5.1. Preface 41
5.2. Impact of the stabilization duration 41
5.2.1. Characterization 41
5.2.2. Impact on the pore structure 48
5.3. Impact of the stabilization temperature 50
5.3.1. Characterization 51
5.3.2. Impact on the pore structure 56
5.4. Impact of the stabilization atmosphere 59
5.4.1. Characterization 59
5.4.2. Impact on the pore structure 64
5.5. Correlations between stabilization and pore structure 66

6. Control of oxygen-flow during post-treatment of KOH-activated carbon nanofibers 69
6.1. Preface 69
6.2. Oxygen flow conditions during post-treatment 69
6.3. High O_2-flow treatment 71
6.4. Low O_2-flow treatment 73
6.5. Comparison of high O_2-flow and low O_2-flow 74
6.5.1. Mass balances 75
6.5.2. Raman spectroscopy 76
6.5.3. Electron microscopy 77
6.5.4. Gas adsorption properties 78
6.6. Potential triggers of a carbon combustion reaction 82

7. Characterization of KOH-Activated carbon nanofibers 87
7.1. Preface 87
7.2. Electron microscopy 87

7.3. Elemental composition 88
7.4. Pore characterization 89
7.4.1. Ar adsorption 89
7.4.2. CO_2 adsorption 91
7.4.3. H_2O adsorption 95

8. Separation of a CO_2/N_2 mixture on KOH-activated carbon nanofibers 97
8.1. Preface 97
8.2. Determination of CO_2/N_2 selectivity based on the ideal adsorbed solution theory 97
8.3. Determination of experimental CO_2/N_2 selectivity 101
8.4. Discussion of CO_2/N_2 selectivities determined by IAST and breakthrough experiments 104
8.5. Working capacity and cycle stability of the adsorbents 107

9. Conclusion 111

Bibliography 115

A. Appendix 133
A.1. ICP-OES 133
A.2. Raman spectra fits 134
A.3. Calcium oxalate calibration of the mass spectrometer 137

1. Motivation

Already today, the global surface temperature is 1.1 °C increased compared to the late 19th century due to the anthropogenic climate change. Consequences of this temperature increase, like an increasing number of wild fires, floodings and droughts, were unequivocally observed in the recent decades [1]. Main drivers of the global warming are anthropogenic greenhouse gas emissions, which were at 59 Gt-CO_{2eq} in 2019 [1]. Among these, CO_2 is a main contributor with a global emission of 37 Gt [2]. Since 1850 the global CO_2 concentration rose from 280 ppm to 410 ppm in 2019, which is mainly caused by anthropogenic emissions [1]. Therefore, joint actions are required to reduce global green house gas and in particular CO_2 emissions to mitigate climate change.

This can be achieved by abandoning CO_2 emitting processes, e.g. by phasing out fossil fuels. However, particular processes are difficult to be transformed into CO_2 free processes, such as cement production. Therefore, efficient CO_2 capture technologies are required. In principle, carbon capture processes can either be realized as direct air capture or point source capture technologies. The first captures CO_2 directly from ambient air at low CO_2 concentrations of approximately 400 ppm, coming at comparatively high cost. The latter, directly captures CO_2 at the emitting point source using the advantage of a high CO_2 concentration in the flue gas, making it more cost efficient [3]. The captured CO_2 could be permanently stored in geological formations, like exploited natural gas deposits, in gaseous state or chemically bound as carbonate (carbon capture and storage, CCS). Besides CCS, a usage of the captured CO_2 as feedstock for the chemical industry is possible (Carbon capture and utilization, CCU). The captured CO_2 is converted into chemicals, such as alcohols or fuels, using electrolysis processes [4–6]. Both carbon capture technologies require well-tailored adsorbents to be efficient and a variety of materials is under investigation. The present work investigates the potential of carbon nanofibers as adsorbent focussing on the impacts of the synthesis steps thermal stabilization and KOH activation on pore structure and resulting CO_2 adsorption properties.

2. Fundamentals

2.1. Carbon capture technologies

To achieve a circular carbon economy, efficient carbon capture technologies need to be developed and brought into operation. In general, CO_2 capture technologies can be separated into the two main principles, direct air capture and point source capture. In a direct air capture process CO_2 is captured at ambient air conditions, which comes with the challenge of a very low CO_2 concentration of roughly 400 ppm. This results in demanding requirements regarding adsorbent and plant design leading to comparatively high cost of these processes [7]. Instead, flue gas capture is applied directly at the point source, having the advantage of significantly higher CO_2 concentrations in the gas stream, thus enabling a more cost-efficient CO_2 capture. Typically, flue gas concentrations of CO_2 are at 5-15 % and even higher CO_2 concentrations are present in cement industry (> 15 %) and in biogas purification (40 %) [8–11].

Both processes can be based on different separation approaches, such as amine scrubbing, membrane-based separation and physisorption on solids. Amine scrubbing is a mature technology for CO_2 removal by chemisorption processes using liquid solutions of alkanolamines, e.g. monoethanolamine. This separation technology comes with a high selectivity towards CO_2 and high purity of the captured CO_2, but suffers from energy-intense regeneration, corrosion of the equipment and toxicity as well as degradation of the used liquids [8, 12].

An alternative is the separation using membranes, which is mainly governed by the pressure gradient for CO_2 separation. They are advantageous with regard to cost and do not require energy-intense regeneration. However, a drawback of membrane separation is the comparatively low selectivity. Therefore, several separation stages are often required [8, 13].

Another technology for CO_2 separation is physisorption at solid adsorbents. In such a process the CO_2 is reversibly bound to the adsorbent due to van der Waals interactions. Typically, these processes are conducted as swing adsorption processes based

on pressure or temperature changes. In the adsorption cycle, a CO_2 containing gas stream is fed into the adsorber column until the adsorbent is fully saturated with CO_2. Subsequently, the process is switched to the desorption cycle, which is typically done by temperature increase (Temperature swing adsorption, TSA) or pressure reduction (Pressure swing adsorption, PSA). By redundant design of the adsorber columns a continuous separation of CO_2 from the feed gas is possible. Although the underlying principle appears straightforward, technical setup are quite complex. Detailed reviews on the technical setup and relevant parameters are given in the corresponding literature [14–16].

2.2. Solid adsorbents for CO_2 capture

Several material classes are studied regarding their potential for an application as adsorbent in CO_2 capture from flue gas. A broad number of studies is available on metal organic frameworks (MOFs) [17–22], zeolites [23–27], functionalized oxides [28], polymers [29] and carbonaceous materials [30–33]. All of these materials have different strengths and weaknesses. MOFs are highly versatile adsorbents since their structure and properties can be well tailored, however they are expensive and often sensitive towards moisture and impurities [34]. Zeolites adsorb high amounts of CO_2 at a high selectivity, but their regeneration is energy intensive and they often show a high competitive adsorption of H_2O. Polymer functionalized oxides show partially promising CO_2 adsorption properties, however often these functionalization is based on polyethyleneimines resulting in energy demanding regeneration due to the chemisorption of CO_2. Furthermore, these materials are typically sensitive to oxidation [35, 36]. Carbonaceous materials are advantageous regarding their high CO_2 capacities, high stability and low cost, but have often the drawback of a weak selectivity and low-pressure adsorption performance [31, 37].

Typically, carbon-based adsorbents are obtained from fossil or renewable sources. Possible renewable sources are biomass, such as bamboo [38, 39], coconut shell [40, 41] or corn cobs [42]. As fossil sources, coals, tars and synthetic polymers are commonly used. Compared to biomass derived carbons, fossil based ones show a well defined composition and thus allow more reproducible tailoring of the material. Often polymer-based precursor such as polyacrylonitrile (PAN), polypyrrolle or polyvinylidene fluoride are used [43, 44].

PAN, which is use as precursor in the present thesis, is industrial available on large scale and can be comparatively easy converted into carbon. The adsorption properties of the carbon nanofibers can be adjusted using a toolbox of modification and activation methods. Since a suitable adsorbent for CO_2 adsorption needs to fulfil a variety of parameters like high capacity, high selectivity, good regeneration conditions, moisture stability and temperature stability, the possibility to tailor and modify the adsorbent is essential [45].

To improve the adsorption capacity of carbon nanofibers, activation methods are frequently applied to increase the pore volume and accessible surface area. This is either done by templating or by physical and chemical activation methods. Templating is done using sacrificial pore forming agents, e.g. polymers, which are selectively removed during or after the synthesis. Physical activation uses pore forming gases, e.g. CO_2 or steam, which react with the carbon structure resulting in pore formation. As third approach chemical activation uses activating agents like KOH or H_3PO_4 to etch the carbon nanofibers. All three methods result in an increase of the accessible surface area promoting a higher adsorption capacity due to a higher number of adsorption sites [46]. Carbon nanofibers activated by such activation methods frequently reach adsorption capacities of 3 to 7 $mmol\,g^{-1}$ (1 bar, 273 K) [3, 33].

Besides a high capacity, a high selectivity towards CO_2 is desired. On carbon materials the selectivity is mainly governed by the pore size distribution and the number of nitrogen heteroatoms. For a high selectivity, a high number of narrow micropores below 0.7 nm is essential. These narrow micropores show high adsorption potentials and for narrow ultramicropores smaller than 0.4 nm a molecular sieving based on the kinetic diameter could occur. Undesired adsorptives, such as N_2, could be excluded due to their size [47].

Besides the pore structure, the hetero atom content, especially the nitrogen content, significantly affects the CO_2 selectivity. Nitrogen-containing functional groups, i.e. pyridinic and pyrrolic groups, interact with the CO_2 due to acid-base interactions, which increases the selectivity of the carbon. Typical CO_2 selectivities for carbon are below 30, however for well tailored materials higher selectivities were obtained [30, 31, 48].

Of course, high capacity and high selectivity are not the only required parameters for a suitable adsorbent. However, both parameters significantly affect the cost of an adsorbent. The costs per captured ton CO_2 were estimated to 38 US-$ for an adsorbent with a selectivity of 50 and a capacity of 2 $mmol\,g^{-1}$. Increasing the capacity of the adsorbent to 5 $mmol\,g^{-1}$ lowers the cost to 33 US-$. An even stronger reduction of the

CO_2 capture cost is obtained by simultaneous doubling of selectivity resulting in cost of 26 US-$ [49]. This clearly emphasizes the importance of tailoring carbon nanofibers regarding these parameters.

2.3. Carbon Nanofiber Synthesis

The synthesis of carbon nanofibers proceeds in several steps, which can be divided into electrospinning, thermal stabilization, carbonization or graphitization, and optional activation (Figure 2.1) [50–52]. Such an activation is either done simultaneously to the carbonization or in an additional step after carbonization. The present work follows the approach of a simultaneous carbonization and activation. A detailed overview on the different process steps for a PAN precursor and KOH activation is given in the following sections.

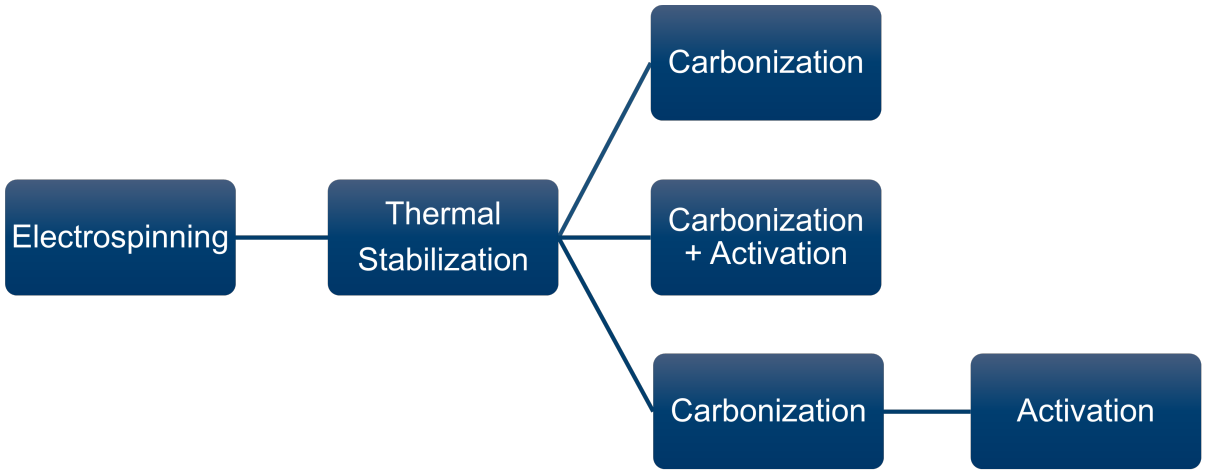


Figure 2.1. – Process steps in carbon nanofiber synthesis. After electrospinning the nanofibers undergo thermal stabilization prior to the actual carbonization and graphitization step, respectively. Additionally, activation methods, such as KOH activation, can be applied simultaneously or after the carbonization to tailor the properties of the carbon material.

2.3.1. Electrospinning

Electrospinning is a versatile method for the synthesis of thin fibers in the nanometer range and is applied in many fields, e.g. catalysis, tissue engineering and filters and textiles [53–55].
In Figure 2.2 a typical electrospinning setup is depicted, consisting of a syringe pump, a laterally moving spinneret equipped with a thin nozzle, a collector and a high voltage source. During the spinning process, the spinning solution is pumped through the system

and ejected through the thin nozzle of the spinneret. Due to the applied high voltage and thus the electric field a 'Taylor cone' is formed at the tip of the nozzle. At the top of the 'Taylor cone' a thin polymer jet is released moving towards the collecting drum. On its path to the collecting drum the polymer jet is affected by the high electric field and repulsive interactions cause an elongation of the jet due to the high charge density. The stretching of the thin polymer jet results in the formation of bending instabilities leading to the formation of random coils. Additionally, the high elongation of the polymer jet leads to fast evaporation of the solvent resulting in the deposition of solid nanofibers on the collecting drum [56].

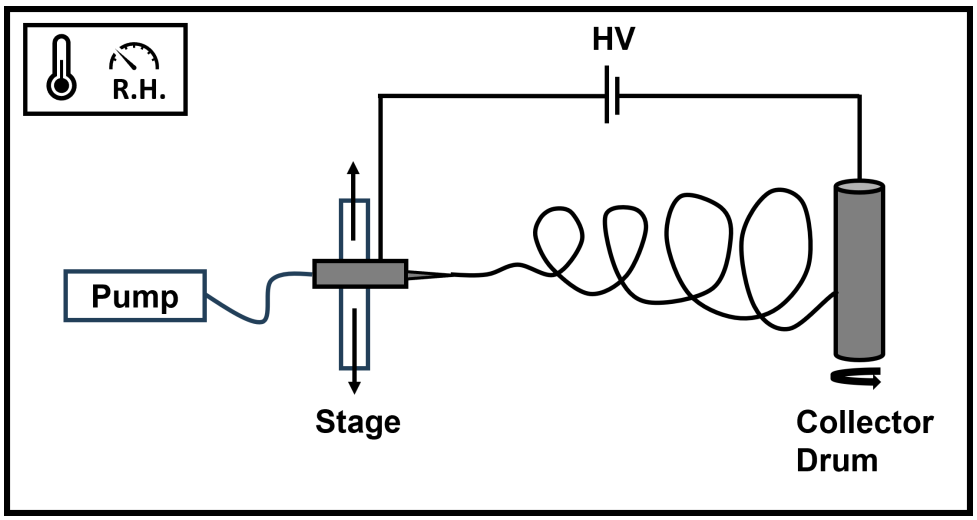


Figure 2.2. – Scheme of an electrospinning setup. The spinning solution is supplied by a pump and then spun through a thin needle mounted on a laterally moving stage under application of a high electrical field onto the collector drum. The system is enclosed in a climate chamber to control temperature and relative humidity during the electrospinning.

Electrospinning is not limited to polymer-based systems, also ceramics and metals can be used as precursor materials. The process is affected by several parameters, some depending on the used precursors, other related to the process conditions. Relevant properties for polymer-based systems are the molecular weight distribution, the viscosity and the electrical conductivity. Additionally, process parameters such as flow rate, applied voltage, atmospheric conditions and needle-collector distance, could have significant effects on the spinning process. Due to the complex interplay of different parameters on the electrospinning, the choice of the ideal spinning conditions is often empirical. More detailed reviews on electrospinning can be found in literature [55–59].

2.3.2. Thermal stabilization

Thermal stabilization is conducted prior to the carbonization to preserve dimensional stability of the nanofibers during the carbonization step. Typically, thermal stabilization is conducted at temperatures between 200 and 300 °C in air or inert atmosphere [50, 51, 60].

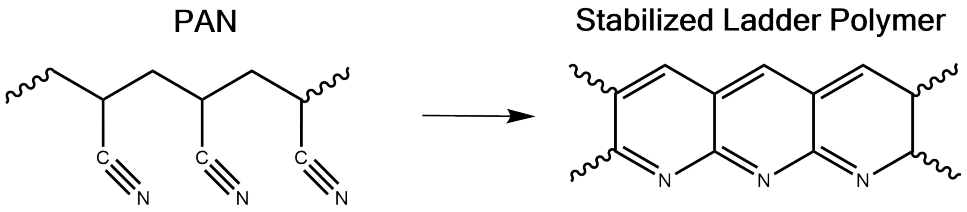


Figure 2.3. – Simplified reaction sequence of thermal stabilization. The PAN undergoes cyclization and dehydrogenation reactions resulting in the formation of an aromatic structure, which is often referred to as 'stabilized ladder polymer' [61].

During thermal stabilization the PAN nanofibers undergo several chemical reactions resulting in the formation of a stabilized ladder polymer, visible in a color change from white to dark brown (Figure 2.1). In 1950 Houtz et. al proposed a fully aromatic heterocyclic structure of the ladder polymer, formed due to cyclization reactions of the adjacent nitrile groups and dehydrogenation of the polymer backbone [61] (Figure 2.3). Since then the reactions and chemical structures of the stabilized ladder polymer have been widely discussed. Detailed reviews on the different proposed structures can be found in literature [62–64].

Today it is widely agreed that the stabilization process involves cyclization, dehydrogenation and oxidation reactions for stabilization in air and only cyclization and dehydrogenation reactions for stabilization in nitrogen.

As shown in Figure 2.4 the first reactions in thermal stabilization of PAN fibers are the cyclization and dehydrogenation. Both reactions occur simultaneously or in immediate succession. This results in the formation of the stabilized ladder polymer, which is a heterogeneous structure containing aromatic heterocycles, but also hydrocarbon and unreacted nitrile segments. If thermal stabilization is conducted in air, additional oxidation reactions could occur, resulting in the formation of oxygen functional groups such as hydroxyl, carbonyl or carboxyl groups [65–68]. The final composition of the stabilized ladder structure highly depends on the process conditions. The obtained stabilized ladder polymer is a prerequisite for preservation of the morphology in the subsequent carbonization and graphitization steps.

Many studies are present on thermal stabilization and its impact on mechanical and electrical properties of carbon nanofibers [69–71]. Far less attention received the impact

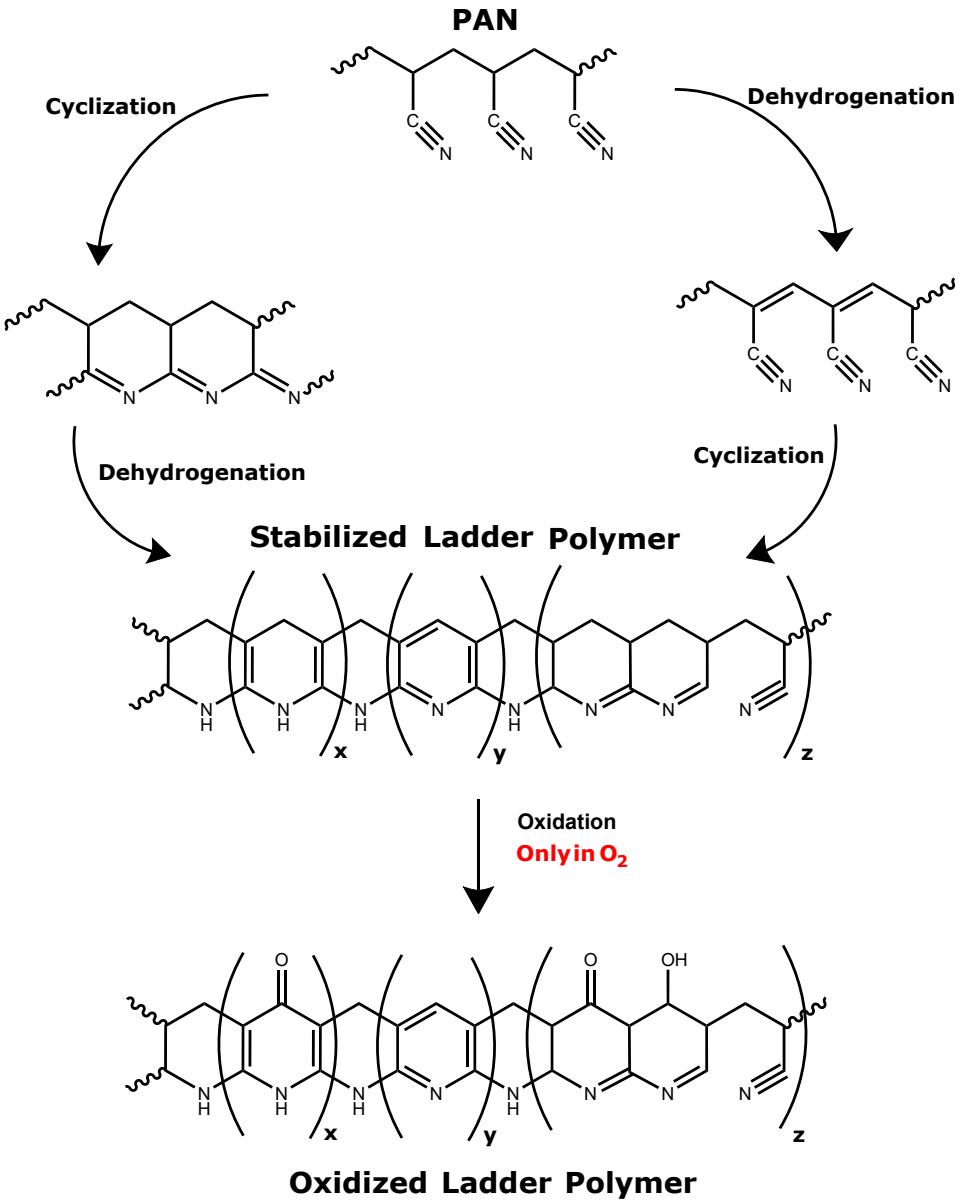


Figure 2.4. – More detailed reaction sequence of the thermal stabilization of PAN. Dehydrogenation and cyclization occur in parallel or in immediate succession and a heterogeneous stabilized ladder structure is formed. If thermal stabilization is conducted in air, oxidation of the stabilized ladder polymer resulting in the formation of oxygen-containing functional groups is observed.

of thermal stabilization on the gas adsorption properties of carbon nanofibers. Marruccia et al. investigated the impact of duration and temperature during stabilization on the CO_2 adsorption properties and claim an increase of the adsorption capacity from 2.7 mmol g^{-1} to 4.2 mmol g^{-1} by an increase of stabilization time and duration [72]. However, as time and duration are varied simultaneously no meaningful relation to the single parameters can be derived. Additionally, the work of Ojeda-López et al. varied the stabilization

temperature from 250 to 300 °C and investigated the CO_2 and CH_4 adsorption [73]. Their results of a decreasing CO_2 capacity at increasing stabilization duration contradict the findings of Maruccia et al. Overall, a comprehensive overview on the impact of thermal stabilization on the gas adsorption properties of carbon nanofibers is currently missing.

2.3.3. Carbonization and Graphitization

The thermal treatment of the stabilized nanofibers in inert atmosphere at temperatures between 600-1700 °C is called carbonization, whereas for temperatures larger than 1700 °C the term graphitization is commonly used. During carbonization the stabilized ladder polymer segments undergo inter- and intramolecular crosslinking reactions resulting in the formation of large carbon frameworks under removal of heteroatoms. The carbonization results in a significant weight loss, high shrinkage of the nanofibers and the evolution of various gases, e.g. NH_3, HCN, H_2O, CO, H_2 and CO_2 [50, 62, 64].

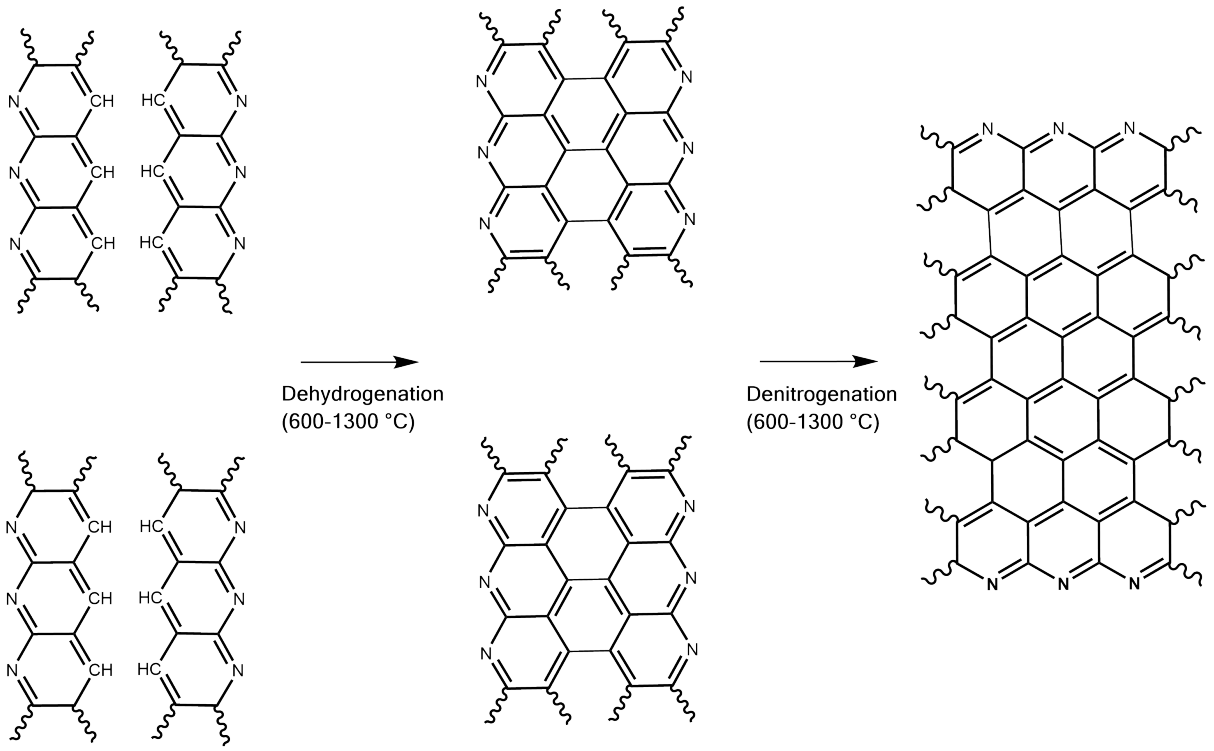


Figure 2.5. – Simplified scheme of the carbonization reactions of PAN. Growth of the carbon framework proceeds by dehydrogenation and denitrogenation reactions [62, 74].

Regarding the chemical changes, Goodhew proposed that elimination of hydrogen occurs at low carbonization temperatures of 400-600 °C, whereas the elimination of

nitrogen takes place at moderate carbonization temperatures (600-1300 °C) (Figure 2.5). Potentially occuring chemical reactions during these steps were described by Watt [64, 75].

Due to its relevance for later discussion, the condensation reaction of adjacent oxidized ladder polymers contributing to the dehydrogenation during the carbonization is shown exemplary in Figure 2.6. For nanofibers stabilized in nitrogen this reaction does not take place due to the absence of oxygen and dehydrogenation occurs just by elimination of H_2. A more detailed discussions on all proposed reactions can be found in literature [64, 75]. After carbonization black carbon nanofibers are obtained, showing a turbostratic arrangement of the carbon frameworks. At increased carbonization temperature these turbostratic arrangements partially arrange towards a graphitic structure [76].

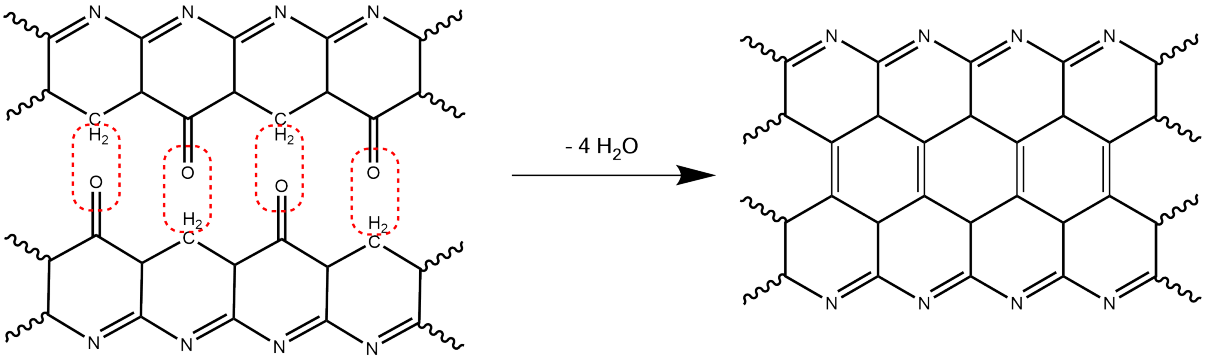


Figure 2.6. – Simplified illustration of condensation reactions between oxidized ladder polymer segments resulting in the growth of carbon frameworks during carbonization proposed by Watt [75].

2.3.4. KOH Activation

Additionally to the carbonization, several activation methods were developed to tailor the properties of carbonaceous materials. Two of these methods are physical and chemical activations. The first uses oxidizing gases, e.g. CO_2 or steam, to initiate gasification reactions of the precursor, the latter uses chemical activating agents, such as KOH or H_3PO_4 [37, 77, 78]. Chemical activation alters the carbon morphology by etching reactions. Commonly, such activations are done subsequent to the carbonization step, but simultaneous carbonization and activation steps are described as well [79–81] (Figure 2.7).

The use of KOH as activating agent was patented by Wennerberg et al. in 1978 [82]. Over the past decades KOH activation was well established and used for a large variety of carbon-based materials, e.g. coals, biomass and carbon fibers [78, 83, 84]. Typically,

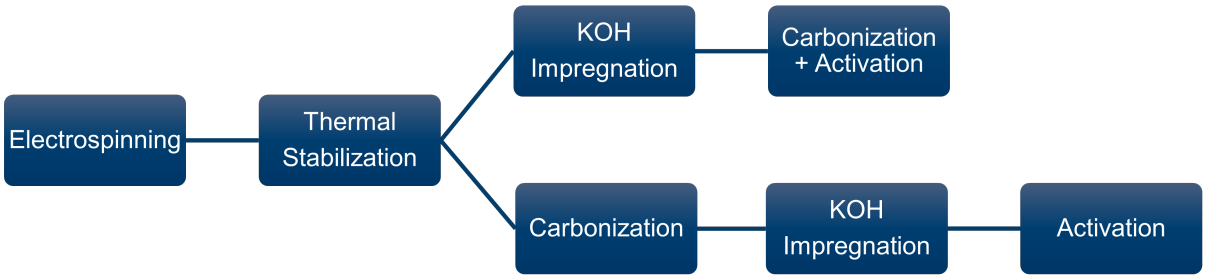


Figure 2.7. – Commonly applied synthesis routes of KOH-activated carbon nanofibers. After thermal stabilization the nanofibers are either impregnated with KOH and simultaneously activated and carbonized in a subsequent step or first carbonized and afterwards impregnated and activated.

KOH-activated carbons are characterized by a high specific surface area and a high pore volume. Frequently reported BET areas of KOH activated carbon fibers range up to 3000 $m^2\,g^{-1}$ and the pore volume easily reaches up to 2 $cm^3\,g^{-1}$ [79, 85].

Although the process is frequently used, the actual reaction sequence during the KOH activation is not fully understood. As overall reaction Equation 2.1 is frequently mentioned [52, 85–87]. However, KOH activation involves several consecutive and parallel reactions. The occuring reactions differ depending on the used precursor and the applied KOH activation conditions. For petroleum coke the dehydration of KOH into K_2O and H_2O was reported as starting reaction (Equation 2.2) [85, 86]. As the temperature increases a coal gasification reaction takes place and carbon and water are transformed into H_2 and CO (Equation 2.3). In parallel a water gas shift reaction occurs and the formed CO reacts with additional H_2O resulting in the formation of H_2 and CO_2 (Equation 2.4). The formed K_2O (Equation 2.2) reacts with present CO_2 resulting in the formation of K_2CO_3 at temperatures between 400 and 800 °C (Equation 2.5). In parallel, at reaction temperatures higher > 700 °C elemental potassium is formed due to reduction of K_2O by H_2 and carbon (Equation 2.7). The elemental potassium could intercalate into the carbon lattice [86, 88].

$$6\ \mathrm{KOH} + 2\ \mathrm{C} \longleftrightarrow 2\ \mathrm{K} + 3\ \mathrm{H_2} + 2\ \mathrm{K_2CO_3}, \quad \Delta H_R = +428\,kJ\,mol^{-1} \tag{2.1}$$

$$2\ \mathrm{KOH} \longleftrightarrow \mathrm{K_2O} + \mathrm{H_2O}, \quad \Delta H_R = +245\,kJ\,mol^{-1} \tag{2.2}$$

$$\mathrm{C} + \mathrm{H_2O} \longleftrightarrow \mathrm{H_2} + \mathrm{CO}, \quad \Delta H_R = +131\,kJ\,mol^{-1} \tag{2.3}$$

$$\mathrm{CO} + \mathrm{H_2O} \longleftrightarrow \mathrm{H_2} + \mathrm{CO_2}, \quad \Delta H_R = -41\,kJ\,mol^{-1} \tag{2.4}$$

$$\mathrm{K_2O} + \mathrm{CO_2} \longleftrightarrow \mathrm{K_2CO_3}, \quad \Delta H_R = -393\,kJ\,mol^{-1} \tag{2.5}$$

$$\mathrm{K_2O} + \mathrm{H_2} \longleftrightarrow 2\,\mathrm{K} + \mathrm{H_2O}, \quad \Delta H_R = +299\,kJ\,mol^{-1} \tag{2.6}$$

$$\mathrm{K_2O} + \mathrm{C} \longleftrightarrow 2\,\mathrm{K} + \mathrm{CO}, \quad \Delta H_R = +430\,kJ\,mol^{-1} \tag{2.7}$$

For multi-walled carbon nanotubes similar reactions were observed, starting from the formation of K_2CO_3 at temperatures of 400 °C. The formed K_2CO_3 etches the carbon framework and K_2O and CO are formed Equation 2.8. At elevated temperatures (> 700 °C) the formation of elemental potassium was observed as well [87].

$$\mathrm{K_2CO_3} + \mathrm{C} \longleftrightarrow \mathrm{K_2O} + 2\,\mathrm{CO}, \quad \Delta H_R = +565\,kJ\,mol^{-1} \tag{2.8}$$

Overall, the occuring reactions during KOH activation can be separated into three kinds of pore-forming mechanisms.

1. Redox reactions directly etching the carbon material
2. Evolution of formed gaseous products, i.e. H_2O, CO, CO_2, H_2
3. Widening of the carbon lattice due to intercalation of elemental potassium

Nevertheless, the actual reaction pathway highly depends on the applied activation parameters and the used precurors. Moreover, the structure of the precursor affects the possibility of potassium intercalation. Overall, these impact factors render the assessment of the exact occuring reaction mechanisms a difficult task [46, 89] The effects of different parameters, such as temperature, KOH:Precursor ratio and duration were thoroughly investigated by many researchers in the recent decades [90].

2.4. Gas adsorption fundamentals

2.4.1. Terminology and pore classification

The term 'adsorption' defines the enrichment of molecules at an interface or in its vincinity. Its reverse process is called 'desorption'. Molecules in the gaseous phase are defined as adsorptives. Adsorbed molecules are called adsorbates and the solid material is defined as the adsorbent [91–93].
In general, adsorption can be split into physi- and chemisorption. The latter is characterized by the formation of a chemical bond between the adsorbent and the adsorbate.

Typically, such adsorption processes show high adsorption enthalpies ($> 50\,kJ\,mol^{-1}$) and are seen as irreversible processes. Therefore, chemisorption is considered as a site specific monolayer adsorption [92].
Opposite to this, physisorption comes with a low enthalpy of adsorption as it is mainly based on van der Waals' forces. Such include London dispersion forces, ion-dipole, ion-induced dipole, dipole-dipole and quadrupole interactions [92]. Physisorption is a reversible process and could occur as multilayer adsorption. As analytical methods, chemisorption is commonly applied to study catalytic processes, whereas physisorption is used to assess surface area and porosity of materials.
Based on a IUPAC recommendation pores can be classified into three categories [93].

- Macropores with pore width larger than 50 nm
- Mesopores with pore width between 2-50 nm
- Micropores with pore width below 2 nm
  - Ultramicropores, (< 0.7 nm)
  - Supermicropores, (0.7-2 nm)

Additionally, micropores are often subdivided into super- and ultramicropores. The pore

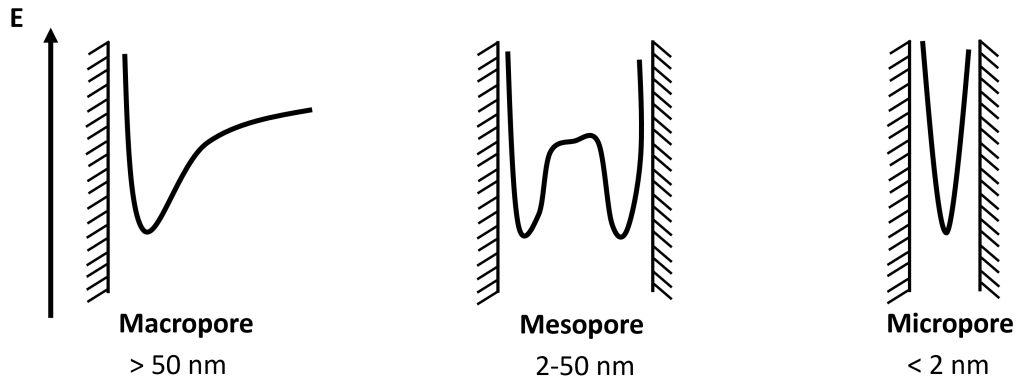


Figure 2.8. – Scheme of pore wall potentials in macropores (> 50 nm), mesopores (2-50 nm) and micropores (< 2 nm). At smaller pore width an overlapping of the pore wall interaction potentials is observed. Illustration adapted from [92].

width governs the adsorption potentials. Macropores have adsorption potentials similar to a flat surface as illustrated in Figure 2.8. For mesopores the pore potentials are partially overlapping, but are not dominating in the center of the pore. Therefore, the adsorption properties are influenced by fluid-fluid interactions and not only by fluid-wall interactions. In micropores the potentials of both pore walls fully overlap resulting in high adsorption potentials fully governed by fluid-wall interactions [92].

2.4.2. Physisorption isotherms

An adsorption isotherm is commonly given as a plot of the adsorbed amount of an adsorbate in dependence to the relative pressure or the absolute pressure. The relative pressure is defined as the absolute pressure normalized by the saturation vapor pressure of the adsorbate at the measurement temperature.

According to IUPAC, 8 adsorption isotherms can be distinguished, describing different adsorption isotherm shapes and adsorption mechanisms (Figure 2.9) [93]. Type I isotherms show a characteristic steep slope at very low relative pressures and approach a limiting value at higher relative pressures. The high adsorption capacity at very low relative pressures, is caused by the micropore filling and thus, high adsorption potentials. According to the current IUPAC recommendation type I isotherms are subdivided into type Ia and type Ib. The main difference between these two types is the initial slope. The steep slope of type Ia isotherm is obtained for microporous materials with a high degree of narrow micropores (< 1 nm), whereas slightly attenuated slope of the Ib isotherms is characteristic for microporous samples with a broader distribution of micropores or partially even narrow mesopores.

Type II isotherms show a high initial slope until the inflection point B. At the inflection point the transition from monolayer coverage into multilayer adsorption occurs. Afterwards, the slope flattens, prior to a second increase approximating the saturation vapor pressure. These isotherms are typically obtained on non-porous or macroporous adsorbents. Type III isotherms show very low adsorption at low relative pressures, but increase significantly at higher relative pressures. Such adsorption isotherms are obtained on adsorbents having low adsorbent-adsorbate interactions.

The type IV isotherm is subdivided into type IVa and type IVb. The IVa isotherm shows a high uptake at low relative pressures and has a distinct hysteresis at higher relative pressures. This hysteresis, the deviation of desorption and adsorption branch, is caused by pore condensation. Such an effect is observed in mesopores, if the adsorbed layers of two pore walls meet. The adsorptive molecules trapped inside the pore by the contact of the adsorbed layers condense to a liquid-like state below the actual saturation vapor pressure. During the desorption the adsorptive is trapped inside the pore until the adsorbed layers are receding. After the adsorbed layers receded, the gas is released and the hysteresis vanishes. Hysteresis can be classified into six types depending on the shape of the hysteresis, which are explained more in detail elsewhere [92, 93]. In contrast to type IVa, IVb isotherms do not show hysteresis and are typical for adsorbents with smaller mesopores.

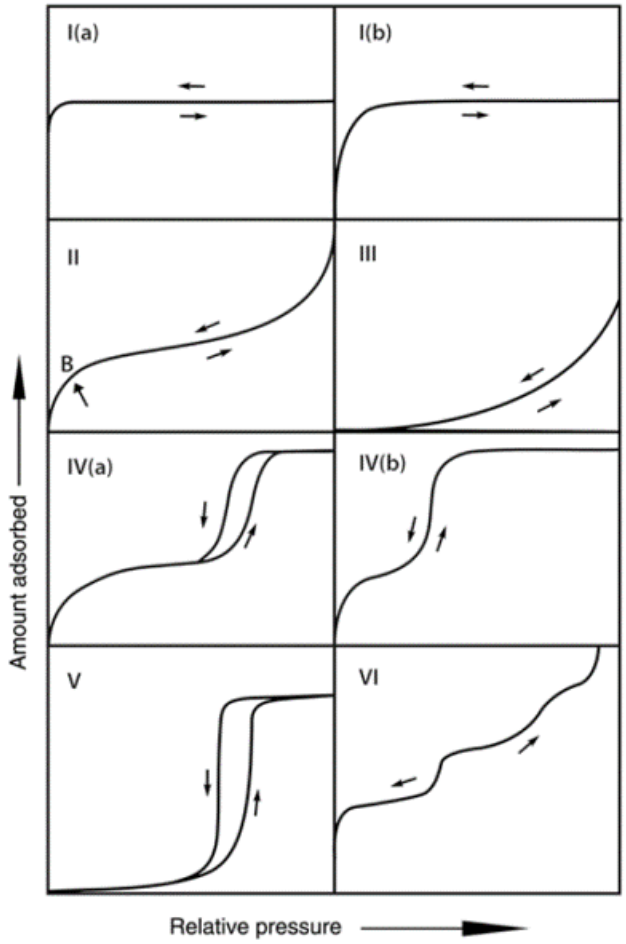


Figure 2.9. – Classification of gas adsorption isotherms into eight isotherm types according to IUPAC, ©DeGruyter, 2015 [93].

At low relative pressures type V isotherms exhibit a shape comparable to type III isotherms. However, at higher relative pressures a steep increase and a distinct hysteresis are observed. This isotherm shape is obtained due to clustering effects and is typically observed for water adsorption on hydrophobic materials. Characteristic for type VI isotherm shapes is the step-by-step increase of the adsorbed amount with increasing relative pressures. This isotherms are obtained for adsorbents showing a layer-by-layer adsorption, which normally occurs on very homogeneous and uniform non-porous surfaces [93].

2.4.3. Isotherm models

Several mathematical models have been developed to describe adsorption isotherms and extensive descriptions and their derivations are found in literature [94–96]. Due to

their relevance for this thesis, a short description on the models developed by Brunauer, Emmet and Teller (BET) and the empirical fit by Tóth is given below [97, 98].
The BET model was developed in 1938 to overcome the drawbacks of the earlier developed Langmuir isotherm model [99]. Langmuir's model was limited to monolayer coverage as it assumes a limited number adsorption sites. Therefore, multilayer adsorption as observed for type II adsorption isotherms can not be described by the Langmuir model. The BET model extents the Langmuir model by addition of adsorption layers with lower adsorption energy on top of other adsorbate molecules. Thus, the adsorbed molecules serve as adsorption sites for further adsorptives and the uppermost adsorbate is in equilibrium with the gas phase. The linear form of the BET equation is given in Equation 2.9 [92, 97].

$$\frac{1}{q \cdot (\frac{p}{p_0} - 1)} = \frac{1}{q_m \cdot C} + \frac{C-1}{q_m \cdot C} \cdot \frac{p}{p_0} \tag{2.9}$$

q Mass of the adsorbed gas
q_m Mass of the monolayer of adsorbed gas
$\frac{p}{p_0}$ Relative pressure
C BET constant

The BET model is widely used for the determination of the specific surface area of materials, which can be calculated using Equation 2.10. However, it is not valid for the description of the adsorption in micropores, since no multilayer adsorption could occur here. Nevertheless, it can be used for the approximation of the BET area of microporous adsorbents considering certain criteria [93]. The BET area of a microporous adsorbent serves more as a useful 'fingerprint', e.g. in comparison to other materials, rather than the real surface area [100, 101].

$$S_{BET} = \frac{q_m \cdot N_A \cdot A_x}{M \cdot m_{sample}} \tag{2.10}$$

N_A Avogadro constant
A_X Cross-sectional area of the adsorbate
M Molar mass of the adsorbate

Another extension of the Langmuir model was developed by Tóth (Equation 2.11). Compared to the Langmuir model an empirical heterogenity parameter t was introduced.

This parameter addresses the heterogenity of many adsorbent materials, which is not reflected in the Langmuir model [98].

$$q_{eq} = q_{max} \cdot \frac{K \cdot p}{(1 + (K \cdot p)^t)^{\frac{1}{t}}} \tag{2.11}$$

q_{eq} Adsorbed amount of adsorbate
q_{max} Maximum adsorbed amount of adsorbate
t Tòth heterogenity parameter
p Pressure
K Affinity constant

2.4.4. Pore size analysis

The gas adsorption isotherms can be used for assessment of the pore size distribution of an adsorbent. A variety of calculation models has been developed, which can in principle be divided into macroscopic and microscopic models [92]. Macroscopic models developed based on Polyani's potential theory of adsorption, e.g. Dubinin-Radushkevich (DR) and Horvath-Kawazoe (HK), are based on classical thermodynamics and give good descriptions of adsorption phenomena in macro- and mesopores. However, they lack proper description of micropore filling and thus are less accurate in the assessment of the micropore volume [92]. This drawback is overcome by modern computational methods based on density functional theory (DFT) or Monte-Carlo simulations. These methods give a proper description of the adsorbed phase on a molecular level and can describe aspects such as micropore filling accurately. This results in an improved determination of the pore size distribution from the macro- to micropore range [92].
Several approaches using different kernels for specific adsorbates and pore geometries exist for DFT calculations. Standard DFT approaches are the non-local DFT (NLDFT) or the quenched-solid DFT (QSDFT). The first, considers the adsorbent as homogeneous material with well defined geometries, the latter takes into account the heterogenity of an adsorbent material. Therefore, the latter is more accurate for the description of disordered materials, e.g. carbons. However, for an accurate pore size analysis a proper choice of the kernel is essential [102].
The Monte-Carlo approach is based on statistics. Based on predefined criteria the interaction of the adsorbate with neighbouring adsorbates and the adsorbent is described. By rotation, removal and insertion of the adsorbate at the adsorption sites the

configuration energy is minimized during the simulation. Finally, a set of isotherms is obtained and by comparison to the actual experimental data a pore size distribution is assigned.

In total, the modern microscopical approaches give accurate assessment of the pore size distribution of adsorbents, if an appropriate kernel is used. However, errors could arise, if wrong assumptions of the pore size geometry are made [92, 102].

2.4.5. Ideal Adsorbed Solution Theory

Adsorbents are commonly used to separate specific gases from gas mixtures. Therefore, the determination of mixed-gas adsorption equilibria is an important parameter. As an accurate experimental assessment is demanding, a variety of models was developed for theoretical determinations of mixture equilibria [103]. A very prominent approach is the ideal adsorbed solution theory (IAST), which was developed by Myers and Prausnitz in 1965 [104]. The determination requires only pure component isotherms of each component at the desired temperature as experimental data. Furthermore, three assumptions are made for IAST determinations:

1. The adsorbent is thermodynamically inert. Changes of the thermodynamic properties during the adsorption process are negligible.

2. The surface area of the adsorbent is equally accessible for all adsorbates. No size exclusion effects.

3. Ideal solution behavior at constant spreading pressure and constant temperature - No interaction of adsorbate molecules with each other

The spreading pressure, which can be understood as negative surface tension, can be calculated according to Equation 2.12. The experimental pure component isotherm needs to be interpolated to provide the theoretical adsorbed amount n_i^0 of the component i at the pressure p_i^0. The pressure p_i^0 is the required pressure to obtain equal spreading pressures π for all components of the mixture (Equation 2.13).

$$\pi(p_i^0) = \frac{RT}{A} \cdot \int_{t=0}^{p_i^0} \frac{n_i^0(p_i)}{p_i} dp_i \tag{2.12}$$

π Spreading pressure
R Universal gas constant
T Temperature
A Surface area of the adsorbent
K Affinity constant
p_i^0 Equilibrium pressure of pure component i
n_i^0 Adsorbed amount of pure component i in equilibrium
p_i Partial pressure of component i

$$\pi = \pi_1 = \pi_2 = \pi_i \tag{2.13}$$

The needed partial pressure of the component i in the mixture can be calculated using Equation 2.14, which is an analogue to Raoult's law. According to the law of mass conservation the molar fractions of all components in the adorbed phase and the molar fraction of all components in the gaseous phase must equal 1 (Equation 2.15) [103, 105].

$$p_i = y_i \cdot p = x_i \cdot p_i^0(\pi) \tag{2.14}$$

y_i Fraction of component i in the gas phase
x_i Fraction of component i in the adsorbed phase
$p_i^0(\pi)$ Partial pressure of component i at spreading pressure π
p Total pressure
p_i Partial pressure of component i

$$\sum_{i=1}^{n} x_i, y_i = 1 \tag{2.15}$$

These equations can be solved for a set gas composition $y_{i,j}$ and total pressure p. The obtained solutions can subsequently be used for determination of the selectivity of the adsorbent towards a component as given in Equation 2.16 [105, 106].

$$S = \frac{n_1}{n_2} \cdot \frac{y_2}{y_1} \tag{2.16}$$

The IAST gives good predictions for systems with components, which adsorb in similar amounts. However, if one component is preferentially adsorbed over the other as well as for heterogeneous adsorbents, IAST predictions could deviate distinctly from experimental selectivity values [106].

2.4.6. Isosteric enthalpy of adsorption

The adsorption of gases on a surface releases energy. The energy release is caused mainly by the change from gaseous state to the adsorbed state, which comes with a loss of molecular motion. Often the term 'heat of adsorption' is used for the released energy during adsorption. However, the term 'isosteric enthalpy of adsorption' is more accurate as it describes well the thermodynamic change of state and gives a negative ΔH_{ads} [107]. A commonly used approach to determine the isosteric enthalpy of adsorption is based on isotherm data at different measurement temperatures. The experimental isotherm data is interpolated using a suitable fit function and afterwards used for calculation of the isosteric enthalpy of adsorption according to the Clausius-Clapeyron approach (Equation 2.17) [101, 108].

$$\Delta H_{ads}(n) = -R \cdot ln(\frac{p_2}{p_1}) \cdot \frac{T_1 \cdot T_2}{T_2 - T_1} \tag{2.17}$$

2.4.7. Static gas adsorption experiments

Gas adsorption isotherms are commonly measured using static gas adsorption methods. The measurement principles can be divided into volumetric and gravimetric approaches. The volumetric approach is most frequently used [92, 101].

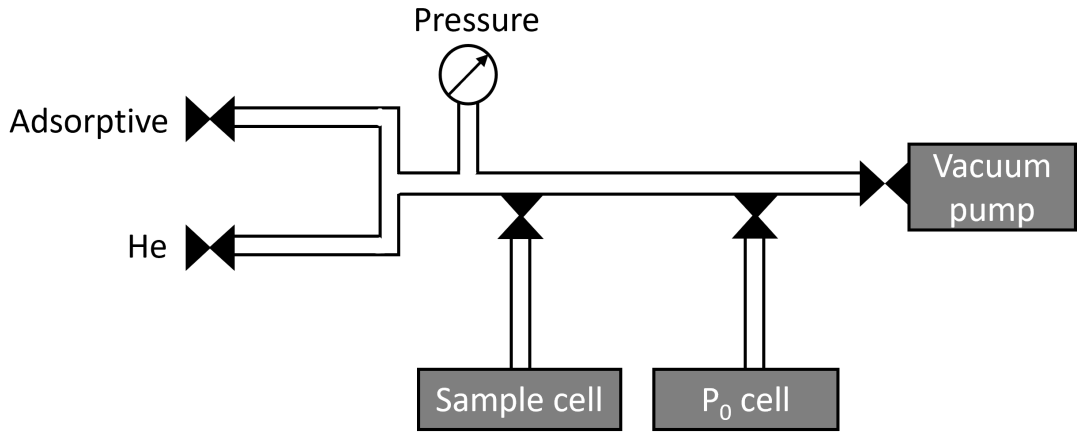


Figure 2.10. – Scheme of a volumetric static gas adsorption device. The setup consists of a calibrated manifold volume, a turbomolecular vacuum pump, several pressure transducers, gas inlets and two ports for sample and reference tube [92, 109].

A typical device consists of a manifold with a calibrated volume, high precision pressure transducers, a turbomolecular vacuum pump, gas ports for helium and the adsorptives and ports for sample and p_0 cell (Figure 2.10). Helium is used to accurately determine

the void volume prior to the measurement, which is essential to calculate the adsorbed quantities using the ideal gas law. At the start of a measurement the setup is fully evacuated. At each dose step a predefined amount of gas is added into the manifold and the pressure is determined. Afterwards the valve to sample and reference is opened and the pressure equilibrates in the total volume. At the beginning of the equilibration a sharp pressure drop is observed as the sample void volume fills, before it attenuates and slowly approaches the equilibrium. This procedure is repeated over several steps resulting in a preset pressure range. Based on the obtained data the adsorption isotherm, typically depicted as adsorbed amount of gas over the relative pressure p/p_0 can be calculated using the ideal gas law [92].

2.4.8. Dynamic sorption experiments

Breakthrough or dynamic gas adsorption experiments measure the gas adsorption on a material in dynamic flow. This allows for analysis of single and multi-component equilibria as well as adsorption kinetics.

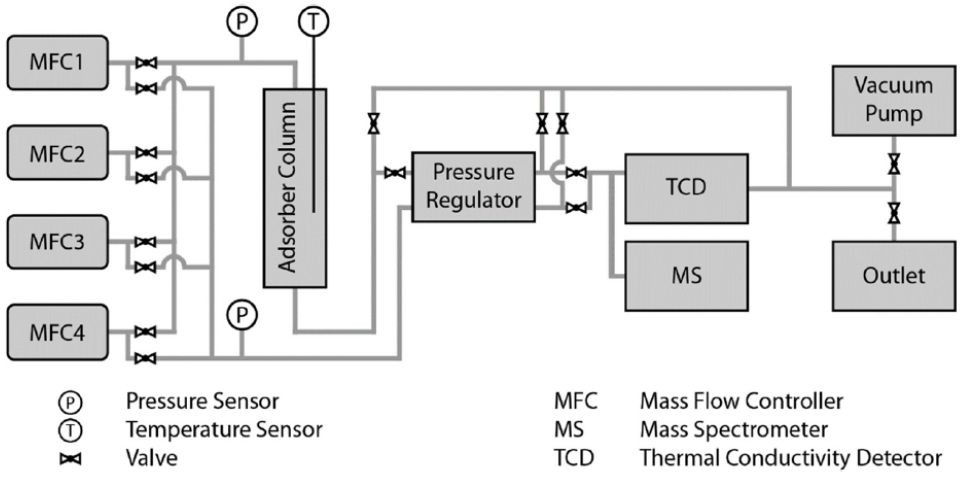


Figure 2.11. – Scheme of a dynamic sorption analyzer. Main components are the adsorber column and the bypass, several MFCs, a pressure regulator for adjustment of experimental parameters as well as a thermal conductivity detector and a mass spectrometer for analysis of the outlet gas composition [110].

A setup of a dynamic breakthrough analyzer is depicted in Figure 2.11. The inlet gas composition can be adjusted using several mass flow controllers (MFCs). Depending on the valve positions the gas mixture is either entering the adsorber column or flowing through the bypass, which allows premixing of gases without affecting the adsorbent. Both, adsorber column and bypass can be used at various pressures using the pressure

regulator. Analysis of the column outlet is done by a thermal conductivity detector or a mass spectrometer to determine the mixture composition [111, 112]. Typically, the inlet concentration and flow rates are preset and the outlet conditions are analyzed. The experiment results a time-resolved breakthrough curve of the adsorptive through the adsorber column. The detected concentration at the column outlet C is normalized to the inlet concentration C_0 (Figure 2.12a) [112]. Such a breakthrough curve can be divided into three phases. In the first phase, all adsorptive molecules are adsorbed on the adsorbent and no adsorptive concentration is detected at the column outlet. After a period of time the adsorbent starts to get saturated, which causes a rise of the adsorptive concentration at the column outlet and marks the onset of the breakthrough. Once the adsorbent is fully saturated, the outlet concentrations matches the inlet concentration.

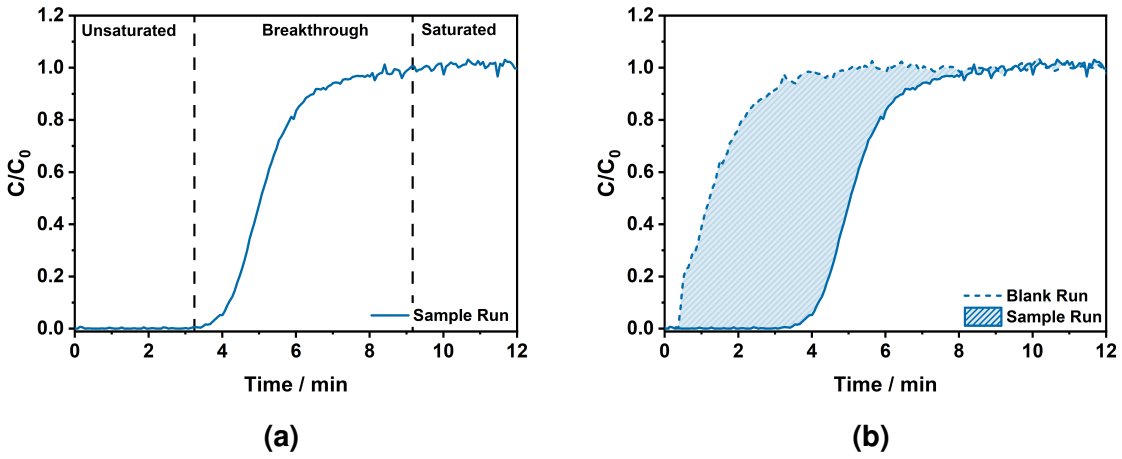


Figure 2.12. – (a) Breakthrough curve obtained in a dynamic sorption experiment normalized to the inlet concentration C_0. (b) Determination of the area between breakthrough curves of a sample and corresponding blank run for determination of the adsorbed amount.

By integration of the area between the start of the experiment and the full breakthrough the adsorbed molar amount $n_{adsorbed}$ can be calculated according to Equation 2.18 [112].

$$n_{adsorbed} = \int \dot{n}_{in}(t)\, dt - \int \dot{n}_{out}(t)\, dt \tag{2.18}$$

The molar flows $\dot{n}_{in,out}$ can be expressed as the product of volume flow $\dot{V}_{in,out}$ and the concentration $C_{in,out}$.

$$n_{adsorbed} = \int \dot{V}_{in}(t) \cdot C_{in}\, dt - \int \dot{V}_{out}(t) \cdot C_{out}\, dt \tag{2.19}$$

Using the ideal gas law the previous equation can be written as Equation 2.20, where the concentration C is written as fraction of the volume fractions $y_{in,out}$ and the molar volume V_m.

$$n_{adsorbed} = \int \dot{V}_{in} \frac{y_{in}(t)}{V_m}\, dt - \int \dot{V}_{out} \frac{y_{out}(t)}{V_m}\, dt \tag{2.20}$$

This equation simplifies for a constant inlet flow and constant adsorptive concentrations to Equation 2.21, which is commonly the case in a dynamic sorption experiment.

$$n_{adsorbed} = \frac{\dot{V}_{in} \cdot y_{in} \cdot t}{V_m} - \int \dot{V}_{out} \frac{y_{out}(t)}{V_m}\, dt \tag{2.21}$$

In highly diluted experiments using low adsorptive fractions the outgoing flow rate can be assumed as constant, resulting in Equation 2.22.

$$n_{adsorbed} = \frac{\dot{V}_{in}}{V_m}(y_{in} \cdot t - \int y_{out}(t)\, dt) \tag{2.22}$$

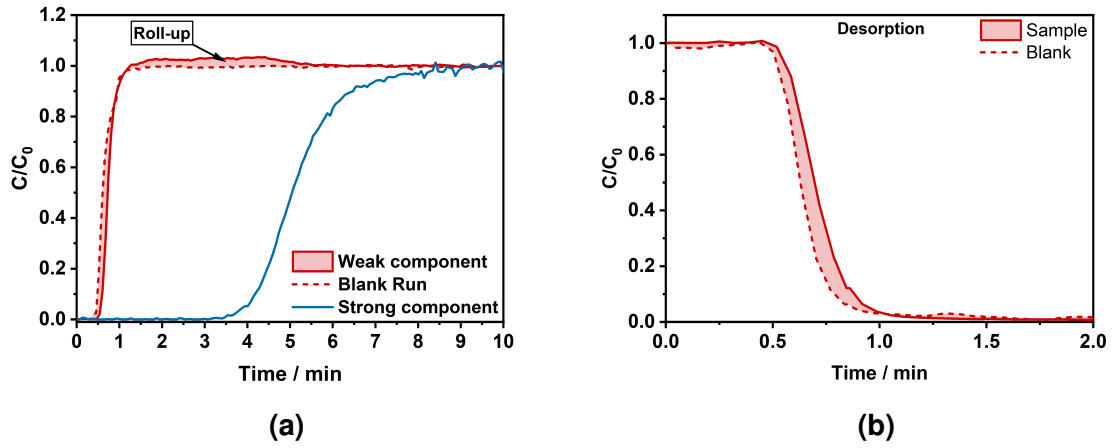


Figure 2.13. – Evaluation of the breakthrough curves of a binary mixture. Roll-up effects in the breakthrough curve of the weak adsorbing component hamper the precise determination of the adsorbed amount. Therefore, the integration of the desorption curve is used which results in a more accurate assessment.

For accurate assessment of the adsorbed amounts a substraction of the void volume of the adsorber column is necessary. The void volume is determined in a blank run experiment. During the experiment the column is filled with non-adsorbing glassbeads, which occupy the same volumetric space as the adsorbent. The blank run is substracted from the sample run and the accurate amount of $\dot{n}_{adsorbed}$ is determined as the area between both breakthrough curves (Figure 2.12b).

In case of binary mixture experiments both breakthrough curves have to be integrated. However, in the case of one very strong and one very weak adsorbing component the integration becomes challenging. The strongly adsorbing component breakthrough looks similar to a single-component breakthrough, but for the weak adsorbing component a roll-up effect is observed. Such roll-ups are assigned to the competitive adsorption of CO_2 and N_2 due to the replacement of N_2 by CO_2 [112] (Figure 2.13a). Moreover, the absence of CO_2 at the column outlet contributes to the effect. For an accurate assessment the roll-up area needs to be substracted from the area of the breakthrough. This becomes difficult for weakly adsorbing components, since both areas could be almost equal, resulting in significant errors. Therefore, it is more convenient to determine the amount of the weakly adsorbed component using the desorption curve [112] (Figure 2.13b)

3. Scope of thesis

A large number of publications on PAN-based carbon nanofibers dealing with mechanical [113], structural, electrical [114–117] as well as gas adsorption properties [76, 118–120] is already available in literature (Ref. chapter 2).
Regarding the gas adsorption properties, research is mainly focused on the impact of the carbonization conditions and different activation methods on the carbon nanofibers. It has been shown that the adsorption capacity and selectivity are tailorable by adjustment of the carbonization temperature [47, 120]. In addition, the introduction of additional pore volume and an increase of the specific surface area can be achieved by different activation methods [33, 90].
The present work focuses on three aspects, which have been scarcely considered so far: the impact of thermal stabilization, the post-treatment conditions after KOH activation and the CO_2 adsorption performance of KOH-activated carbon nanofibers from a binary CO_2/N_2 gas mixture studied in dynamic sorption experiments.

The few existing studies [72, 73], dealing with the impact of thermal stabilization on the gas adsorption properties, do not provide an in-depth understanding of the impact of different stabilization parameters. Partially, stabilization parameters are varied simultaneously, making it impossible to assess their individual impacts. Additionally, the results are partially contradicting and the impact of the stabilization atmosphere is not studied so far.
Therefore, the present work aims to provide a detailed understanding of relevant process parameters, such as stabilization duration, stabilization temperature and stabilization atmosphere, on the pore structure and corresponding gas adsorption properties of the carbon nanofibers. By combining gas adsorption measurements and chemical characterization techniques, correlations between stabilization parameters, pore structure and CO_2 adsorption properties of the carbon nanofibers shall be drawn.

KOH activation is a frequently applied activation method to adjust the pore structure of carbon nanofibers. Commonly, the freshly activated materials are directly exposed to

ambient air after KOH activation. However, since air-sensitive elemental potassium is formed during activation, an uncontrolled exposure to ambient air might cause vigorous potassium oxidation reactions, which alter the activated carbon nanofiber structure. By application of different oxygen flow conditions as post-treatment, potential impacts on the pore structure shall be studied.
The results are used to synthesize a series of KOH-activated carbon nanofibers at different KOH:Fiber weight ratios of 1:4, 2:4 and 3:4 to increase the adsorption capacity of the pristine carbon nanofibers. Comparatively mild KOH:Fiber weight ratios were chosen to preserve the high ultramicropore volume of the pristine carbon nanofibers, which is essential for their excellent selectivity [120]. The KOH-activated carbon nanofibers are fully characterized to analyze the pore structure and gas adsorption capacities.
Subsequently, the selectivity of CO_2 over N_2 on the KOH-activated carbon nanofibers is determined using the ideal adsorbed solution theory (IAST) for typical flue gas compositions (10 % CO_2 in N_2). To verify the results of the IAST selectivity determination, breakthrough experiments using a binary CO_2 in N_2 gas mixture are conducted in a dynamic sorption analyzer. The experimental selectivities are compared to the results of the IAST calculations and deviations of both are discussed. Additionally, further important adsorbent characteristics, such as working capacity and cycle stability are investigated in dynamic sorption experiments by application of an idealized vacuum pressure swing adsorption cycle.

Overall, this work shall improve the understanding of the impact of thermal stabilization on the pore structure and CO_2 adsorption properties of carbon nanofibers. Moreover, the work on post-treatment after KOH activation deals with an aspect of the commonly applied KOH activation, which is currently overlooked although potassium oxidation reactions are expected based on the proposed activation mechanism. Lastly, adsorbent characterization and the CO_2 in N_2 breakthrough experiments shall investigate the advantages and disadvantages of KOH-activated carbon nanofibers for an application in the separation of CO_2 from flue gas.

4. Experimental

4.1. Synthesis of pristine carbon nanofibers

For the synthesis of the pristine carbon nanofibers used in chapter 5, custom-made PAN-based nanofibers were supplied by Stellenbosch Nanofiber Company, South Africa. The nanofibers were synthesized using a needleless electrospinning process and were used without further modifications. The PAN-based nanofibers were thermally stabilized in a drying oven (Carbolite Gero GmbH & Co. KG., Germany) at temperatures of 200, 225, 250, 275 and 300 °C in air for 1 h. Additionally, a series of samples was heated to 250 °C in air and maintained there for 0.5, 1, 4, 8 and 15 h. The heating rate during these experiments was at 5 K min^{-1}. Moreover, thermally stabilized nanofibers were synthesized at 250 °C for a duration of 15 h in N_2 instead of air inside a tube furnace (Carbolite Gero GmbH & Co. KG, Germany). Similar to the previous experiments the heating rate was set to 5 K min^{-1}. An overview on all applied synthesis parameters is given in Table 4.1.

Table 4.1. – Investigated stabilization parameters in the temperature, duration and atmosphere series.

Temperature			**Duration**			**Atmosphere**		
Temp.	*Dur.*	*Atm.*	*Temp.*	*Dur.*	*Atm.*	*Temp.*	*Dur.*	*Atm.*
°C	h	–	°C	h	–	°C	h	–
200	1	Air	250	0.5	Air	250	15	Air
225	1	Air	250	1	Air	250	15	N_2
250	1	Air	250	4	Air			
275	1	Air	250	8	Air			
300	1	Air	250	15	Air			

After thermal stabilization all samples were carbonized for 3 h at 800 °C in an Ar flow of 105 L h^{-1} inside a tube furnace (Carbolite Gero GmbH & Co. KG, Germany) using a heating rate of 5 K min^{-1}.

The pristine carbon nanofibers discussed in chapter 7 and chapter 8 were based on inhouse synthesized PAN nanofibers. Solutions of 10 wt.-% PAN in *N,N*-dimethylform-

amide (DMF) were prepared by adding 8 g PAN (150.000 g mol^{-1}, BOC Science, USA) to 72 g DMF (VWR Chemicals, Germany). The solutions were stirred for 48 h at room temperature under protection from direct light. Afterwards the solution was electrospun on an electrospinning device (IME Technologies, Netherlands) under constant climate conditions of 25 °C and 30 % relative humidity. The acceleration voltage was set to 25 kV and the polymer solution was supplied at a flow rate of 120 µL min^{-1} through a 4-tip spinning needle. The needle was fixed on a spinneret moving with 20 mm s^{-1} over a range of 120 mm at a turn delay of 500 ms. The spun nanofibers were collected on a drum collector with a diameter of 90 mm rotating at a speed of 1000 rpm. The electrospinning was conducted for 3 h until a total volume of 21.6 mL was obtained. Afterwards oxidative stabilization was conducted at 250 °C for 15 h using a heating rate of 5 K min^{-1} in air in a drying cabinet (Binder GmbH, Germany). Finally, the samples were carbonized for 3 h at 800 °C in an Ar flow of 105 L h^{-1} inside a tube furnace (Carbolite Gero GmbH & Co. KG, Germany) at a heat rate of 5 K min^{-1} (Table 4.2).

Table 4.2. – Overview of the used spinning parameters used for the synthesis of the inhouse carbon nanofibers.

Parameter	Value
Flow rate	120 µL min^{-1}
Voltage	25 kV
Nozzle-Collector distance	140 mm
Inner nozzle diameter	0.8 mm
Lateral range	120 mm
Spinneret speed	20 mm s^{-1}
Collector diameter	90 mm
Collector Speed	1000 min^{-1}

4.2. Synthesis of KOH-activated carbon nanofibers

The KOH-activated carbon nanofibers discussed in chapter 6, chapter 7 and chapter 8 were electrospun according to the procedure for the inhouse spinning process described in section 4.1. Afterwards, oxidative stabilization was conducted at 250 °C for 15 h using a heating rate of 5 K min^{-1} in air in a drying cabinet (Carbolite Gero GmbH & Co. KG., Germany). Then 200 mg of the stabilized nanofibers were impregnated with 10 ml KOH solution. The KOH activation solutions were prepared in advance at concentrations of 0.09, 0.18, 0.26 mol L^{-1} KOH in H_2O, corresponding to KOH:Fiber weight ratios of 1:4,

2:4 and 3:4. After 2 h soaking time the KOH impregnated nanofibers were dried in a drying cabinet (Carbolite Gero GmbH & Co. KG., Germany) at 85 °C for a duration of 3 h.

For the results presented in chapter 6 the carbonization and activation process was conducted inside a thermogravimetric analyzer coupled to a mass spectrometer (STA 449 F1 Jupiter coupled to QMS 403D Aëlos, Netzsch GmbH, Germany (TGA-MS)). A 5 mL Al_2O_3-beaker was filled with 200 mg of the KOH impregnated stabilized nanofibers. Prior to the simultaneous carbonization and activation the furnace was purged trifold with Ar to obtain an inert atmosphere. Subsequently, the carbonization and activation was conducted at 800 °C for 3 h at a flow of 40 mL min^{-1} Ar (5.2, Air Products, France) using a heat rate of 300 K h^{-1}. After the temperature was maintained at 800 °C for 3 h, the sample was cooled down to 40 °C at a cooling rate of 200 K h^{-1}. As soon as a temperature of 40 °C was reached, the atmosphere was switched to a mixture of N_2:O_2. Two different mixture compositions were used as post-treatments. One labelled as 'low O_2 flow condition' at an O_2-flow rate of 4 mL min^{-1} in 16 mL min^{-1} N_2 and a second labelled as 'high O_2 flow condition' at 175 mL min^{-1} O_2 and 75 mL min^{-1} N_2. All post-treatments were conducted for 45 minutes. Finally, the obtained KOH-activated carbon nanofibers were neutralized by washing with distilled water to remove potassium compounds until a neutral pH value was achieved.

Additionally, experiments were conducted in a horizontal tube furnace (REST-E 400/6, Carbolite Gero GmbH Co. KG, Germany) to ensure comparability of the measurements in the TGA-MS to the commonly used synthesis in the tube furnace. An alumina boat containing 200 mg of the KOH impregnated nanofibers was put into the tube furnace, which was trifold purged with Ar. The simultaneous carbonization and activation step was conducted at 800 °C for 3 h at a heating rate of 5 K min^{-1}. After cool down to 40 °C the atmosphere was switched to N_2:O_2. Comparable to high O_2-flow conditions the samples were directly exposed to ambient air, whereas low O_2-flow conditions were applied by addition of compressed air at 2 L h^{-1}. Afterwards the samples were neutralized by washing with distilled water until a neutral pH value was achieved.

The KOH-activated carbon nanofibers discussed in chapter 7 and chapter 8 were all carbonized in the tube furnace and low O_2-flow conditions were applied as post-treatment. After neutralization and drying the KOH-activated carbon nanofibers were transformed into pellets according to the process described in patent WO002024-170630A1 [121]. First, the material was milled in a knife mill (IKA-Werke, Germany) for 5 runs at 60 s. The obtained nanofiber powder was afterwards mixed with a binder (PAN)

yielding a highly viscous carbon nanofiber dispersion. This dispersion was extruded into cylindrical strings, which were dried at 60 °C for 1 h with subsequent vacuum drying overnight. Subsequently, the carbon nanofiber strings were cut into cylindrical pellets of an average length of 4 mm and a diameter of 2 mm. Finally, an additional carbonization step was conducted at 800 °C for 3 h in Ar.

4.2.1. Synthesis of reference materials

Several reference materials were tested in chapter 6 regarding an impact of the applied post-treatment conditions. All reference experiments were conducted inside the TGA-MS. KOH impregnation and activation were conducted according to the procedure described in section 4.2. All experiments were conducted at high O_2-flow conditions as post-treatment. Below a summary on the reference materials is given (Table 4.3). The carbon papers obtained from Freudenberg Performance Materials and Toray CFE were pyrolyzed prior to the experiment at 1000 °C for removal of flourine residues. The coconut shells were carbonized at 500 °C prior to the impregnation following the process described in [40, 122].

Table 4.3. – Overview on reference materials used for investigations discussed in chapter 6.

Material	Dimension	Supplier	Pretreatment
PAN powder	Bulk material	BOC Sciences	Therm. stabilization
Coconut shell	Bulk material	Inhouse	Pre-Carb. at 500 °C
Toray Paper	Microfiber	Toray CFE	Pyrolyzed at 1000 °C
Freudenberg Paper	Microfiber	Freudenberg Performance Materials	Pyrolyzed at 1000 °C
PAN-based nanofibers	Nanofiber	Stellenbosch Nanofiber Company	Therm. stabilization
PAN-based nanofibers	Nanofiber	Inhouse	Therm. stabilization

4.3. Characterization of the carbon nanofibers

4.3.1. Elemental analysis

A varioELcube elementar analyser (Elementar, Germany) was used for determination of the C,H,N and O content of the samples. The C,H,N content was determined by a triple determination with 2 mg each. The O content was determined by a single determination for the results in chapter 5 and chapter 7 and by calculating the difference between

the CHN content to the total composition for the results presented in chapter 6. The elemental analysis was conducted by the Central Institute of Engineering and Analytics (ZEA-3) of Forschungszentrum Jülich GmbH.

4.3.2. Simultaneous thermal analysis

An STA 449 F1 Jupiter (Netzsch GmbH, Germany) coupled to a mass spectrometer (QMS 403, Aëlos, Netzsch GmbH, Germany) was used for performing simultaneous TGA and differential scanning calorimetry (DSC) measurements using the MS for residual gas analysis.

The thermal treatment for the results presented in chapter 6 is given in the synthesis section (section 4.2). The emitted reaction products were detected by the MS. The measurements were conducted in multiple ion detection (MID) mode. All relevant gases were identified with a scan measurement for m/z 0-100 in an additional run prior to the actual measurements. The MID runs were normalized to a reference run, to correct contamination of the device caused by the formation of soot particles during the reaction. For data evaluation the peak area of the detected components was determined by integration. The obtained weight normalized peak area is converted into the molar amount of CO_2 based on a calibration using $CaC_2O_4\,x\,H_2O$ [123]. For the calibration masses of 50, 75, 100, 125 and 150 mg of $CaC_2O_4\,x\,H_2O$ were transferred into the TGA crucible and afterwards heated to 1000 °C. Based on the obtained results, a relation of the peak area CO_2 to the molar amount could be drawn. A more detailed description of the calibration and the calibration data are shown in section A.3.
For determination of the emitted reaction heats in the DSC experiments the device was calibrated using a sapphire disc. The DSC measurements were conducted using an equal heat treatment as for the experiments in the TGA beaker. The sample mass of KOH impregnated nanofibers was at 20-30 mg.
The results in chapter 5 were obtained in the temperature range 30-450 °C at a heating rate of 5 $K\,min^{-1}$ in artificial air (40 $mL\,min^{-1}$ N_2 and 10 $mL\,min^{-1}$ O_2). Similar to the previous DSC measurements 20-30 mg of the PAN-based nanofibers were used.

4.3.3. Infrared spectroscopy

Infrared (IR) spectra were recorded on a SpectrumOne FT-IR (PerkinElmer, USA) using an attenuated total reflexion (ATR) setup with a diamond/ZnSe composite crystal and

a HgCdTe detector. The measurements were conducted at 32 scans and a resolution of 4 cm^{-1}. Prior to each measurement a background scan was obtained. All spectra were baseline corrected and the observed absorption bands were evaluated. Based on the absorption band height of the nitrile valence vibration at 2244 cm^{-1} and the $-C=N-/-C=C-$ valence vibration at 1590 cm^{-1} the cyclization index CI was calculated according to Equation 4.1. The cyclization index is used as an assessment of the progress of the stabilization. For the calculations the absorptivity constant n was set to 0.29 according to the work of Collins et al. [124, 125].

$$CI = \frac{n \cdot Abs_{\nu_{1590cm^{-1}}}}{n \cdot Abs_{\nu_{1590cm^{-1}}} + Abs_{\nu_{2244\,cm^{-1}}} \cdot 100} \tag{4.1}$$

CI	Cyclization index
n	Absorptivity constant
$Abs_{\nu_{2244\,cm^{-1}}}$	Absorption band height of the valence vibration of the $-C\equiv N$ groups
$Abs_{\nu_{1590\,cm^{-1}}}$	Absorption band height of the valence vibration of the $-C=N-$ groups

4.3.4. Raman spectroscopy

The Raman measurements discussed in chapter 5 were conducted on an Alpha R Raman microscope (WITec GmbH, Germany). The Raman spectra were acquired at a laser wave length of 532 nm and a laser power of 2 mW. For the evaluation a baseline corrected average spectrum of 5 measurements was used. The averaged spectra were fitted by 5 Gaussian fits, orienting close to the recommendations in literature [126, 127], labelled as D_1, D_2, D_3, D_4 and G band. Based on the obtained peak area of the D_1 and G band the D_1/G ratio as a measure for the degree of structural order was calculated.

The results presented in chapter 6 were obtained on an Alpha R Raman microscope (WITec, Germany) using a 532 nm laser at a power of 2mW. For each sample, high and low O_2-flow, Raman spectra were acquired for a total of 30 s measurement time at five different, representative surface locations. All spectra were baseline corrected. For the determination of the D/G ratio of the overlapping carbon D and G bands, the spectra were fitted using LMFIT version 0.9.14 for Python [128], employing a non-linear least-squares algorithm. Due to the signal shape, the D band was fitted using two Gauss peaks and the G band and $2D$ band by one Gauss peak.

4.3.5. ICP-OES

Inductively coupled plasma optical emission spectroscopy (ICP-OES) was performed on an iCAP 7600 analyser (ThermoFisher Scientific, USA). Two parallel digestions of 100 mg sample each were prepared in a furnace with 250 mg lithium borate. The samples were heated to 1050 °C during 3 h and maintained for 30 minutes at this temperature. The obtained melt was diluted in 50 ml 5 % HNO_3 and filled up to 100 ml. The obtained solutions were analyzed in the ICP-OES. The ICP-OES measurements were conducted at the Central Institute of Engineering and Analytics (ZEA-3) of Forschungszentrum Jülich GmbH.

4.3.6. Electron microscopy

Scanning electron microscopy (SEM) images were recorded using a Quanta FEG650 microscope (FEI, USA) equipped with an Everhart-Thornley detector. The acceleration voltage was set to 20 kV for the results in chapter 6 and to 5 kV for the results in chapter 7, respectively. Proper fixation of the carbon nanofibers on the sample holder was ensured by the use of adhesive carbon tape.

4.3.7. Static gas adsorption

Several static gas adsorption analyzers and adsorptives were used during this thesis. A list of the used adsorptives is given in in Table 4.4.

Table 4.4. – Overview on the used adsorptives for static gas adsorption experiments.

Adsorptive	Supplier	Purity
Ar	Air Products	6.0
He	Air Products	6.0
CO_2	Air Products	4.5
N_2	Air Products	5.2
H_2O	–	–

Evaluation of the gas adsorption data was done using Asiqwin 5.0 (Quantachrome, USA) and pyGaps 4.5.0 [129]. Asiqwin was used for isotherm plotting, determination of the BET area and calculation of the pore size distributions. Based on the Ar adsorption data, the pore size distributions were calculated using a QSDFT method with a kernel for slit pores on carbon. CO_2 adsorption data was used to determine pore size distributions

using Monte-Carlo calculations with a kernel for slit pores on carbon. IAST calculations and the determination of the isosteric enthalpies of adsorption was conducted using pyGaps 4.5.0 [129]. Determination of the isosteric enthalpy of adsorption was done using the Clausius-Clapeyron approach.
The used devices are listed separately for each chapter below:

- **Chapter 5: Impact of the thermal stabilization parameters on the pore structure of carbon nanofibers**

  The gas adsorption results were obtained on a Micro 300 (3P Instruments GmbH & Co. KG., Germany) using Ar at 87 K, CO_2 and N_2 at 273 K. 50-100 mg of the sample were weight into the sample tubes and outgassed for 15 h at 150 °C prior to the measurements. The temperature for Ar isotherm measurements was adjusted using Cryotunes (3P Instruments GmbH & Co. KG., Germany) and a water bath for the CO_2 and N_2 measurements.

  The H_2O isotherms of the thermally stabilized nanofibers were measured on a gravimetric vapor sorption analyzer at 298 K (DVS Vacuum, Surface Measurement Systems, United Kingdom). For each sample 15-25 mg were weight into the sample crucibles. Prior to the measurement the samples were outgassed at 70 °C for 4 h.

- **Chapter 6: Control of oxygen flow during post-treatment of KOH-activated carbon nanofibers**

  The static gas adsorption isotherms were measured on a Micro 300 (3P Instruments GmbH & Co. KG, Germany). Prior to each measurement the samples were outgassed for 15 h at 150 °C. 25-50 mg of the sample were used for the measurements. Ar isotherms were recorded at 87 K and CO_2 isotherms at 273 K. The temperature was controlled using Cryotunes (3P Instruments GmbH & Co. KG., Germany) for Ar measurements and a water bath for CO_2 and N_2 measurements.

  An Autosorb IQ 2 (Quantachrome, USA) was used to determine the CO_2 kinetics. A single point isotherm at 50 mbar and 298 K was measured using the VectorDose™ mode.

  A Quadrasorb Evo (Quantachrome, USA) was used for determination of the CO_2 adsorption isotherms at 273, 283 and 293 K for the calculation of the isosteric

enthalpy of adsorption. Adjustment of the temperature was done using a water bath.

- **Chapter 7: Characterization of KOH activated carbon nanofibers**

  The static gas adsorption isotherms were measured on a Micro 300 (3P Instruments GmbH & Co. KG, Germany). Prior to each measurement the samples were outgassed for 15 h at 150 °C. 100-150 mg of the sample were used for the measurements. Ar isotherms were recorded at 87 K and CO_2 isotherms at 273 and 298 K. The H_2O adsorption isotherms were measured on an AutoSorb IQ2 at a temperature of 298 K. All measurement temperatures were controlled by a water bath.

- **Chapter 8: Separation of a binary CO_2/N_2 mixture on KOH activated carbon nanofibers**

  The static gas adsorption isotherms were measured on a Micro 300 (3P Instruments GmbH & Co. KG, Germany). Prior to each measurement the samples were outgassed for 15 h at 150 °C. 100-150 mg of the sample were used for the measurements. CO_2 and N_2 isotherms were measuread at 298 K using a water bath for temperature control.

4.3.8. Dynamic gas adsorption

The breakthrough experiments were conducted using a mixSorb SHP (3P Instruments, Germany). The outlet flow was analyzed by a mass spectrometer (GSD 350, Pfeiffer Vacuum, Germany). The adsorber columns were made from stainless steel with an inner diameter of 4.0 and 8.0 mm and a length of 15 cm. Approximately 0.4 g of the samples were added into the adsorber column. After mounting the adsorber column a leak test at 7 bar was performed and the pressure drop of the column at 5 bar was determined. Prior to the measurements the samples were pretreated at 300 °C at 20 $mL\,min^{-1}$ He flow for 1 h. The inlet gas mixture composition was adjusted using the MFCs. An overview of the experimental parameters for the breakthrough experiments is given in Table 4.5. All experiments were conducted at 298 K. A void volume correction was done for all experiments based on a blank run with an adsorber column filled with non-adsorbing

glassbeads covering the same volume as the adsorbents. For determination of the needed amount of glassbeads, He pycnometry was used for density determination of the adsorbents.

Table 4.5. – Overview on the experimental parameters of the conducted breakthrough experiments.

Experiment	Column	$\dot{V}_{Carrier}$	$\dot{V}_{CO_2}$	$\dot{V}_{N_2}$	P_{total}	P_{ads}	CO_2:N_2
	mm	mL min^{-1}	mL min^{-1}	mL min^{-1}	bar	bar	%
Selectivity at 1 bar	8.0	80	2	18	5	1	10:90
N_2 Isotherms at 10 bar	4.0	95-50	–	5-50	20	1-10	0:100
Working Capacity at 10 bar	4.0	0	5	45	10	10	10:90

The breakthrough curves were evaluated using the software mixSorb manager (3P Instruments, Germany). The MS data file was attached to the mixSorb manager data file and an offset correction was performed using implemented methods of the software. For each breakthrough curve the base- and topline was adjusted manually. The baseline was set to 0 and the top line is set to the the mean value of the outlet concentration. Afterwards integration of the breakthrough curves was conducted. Such an integration was conducted for the adsorption cycle and the desorption cycle, since the assessment of weakly adsorbing components is more accurate in the desorption cycle due to roll-up effects in the adsorption cycle (see subsection 2.4.8). For determination of the accurate adsorbed amount the area of the blank run is substracted from the area of the sample run.

- **Selectivity determination**

  The CO_2 selectivity of the adsorbents in a 10:90 CO_2:N_2 mixture was determined at an adsorptive pressure of 1 bar. Non-adsorbing helium was used as carrier gas resulting in total pressures of 5 bar. The adsorbed amounts of CO_2 and N_2 as well as the partial pressures of the adsorptives were used for determination of the selectivity according to Equation 4.2.

$$S_{CO_2} = \frac{n_{CO_2} \cdot p_{N_2}}{n_{N_2} \cdot p_{CO_2}} \tag{4.2}$$

S_{CO_2} Selectivity of CO_2 over N_2
n_{CO_2} Adsorbed amount of CO_2
n_{N_2} Adsorbed amount of N_2
p_{CO_2} Partial pressure of CO_2
p_{N_2} Partial pressure of N_2

- **Working capacity and cycle stability**

  The working capacity and cycle stability were determined in binary mixture experiments at a total pressure of 10 bar. The $\dot{V}_{CO_2}$ was at 5 mL min^{-1} and The $\dot{V}_{N_2}$ was at 45 mL min^{-1} reflecting a 10 % CO_2 in N_2 composition. The experiments were conducted using a simplified pressure swing adsorption cycle with an adsorption cycle of 20 minutes followed by a 20 min desorption cycle. Desorption was conducted at technical vacuum conditions. The experiment was conducted over a total of 20 cycles to give a first assessment of cycle stability.

- **High pressure N_2 isotherms**

  The N_2 isotherms at pressures up to 10 bar were determined in a binary mixture of N_2 in He. The total pressure was set to 20 bar. Stepwise the partial pressure of N_2 was increased from 5 up to 50 %, reflecting a 1 bar pressure increase each step. After each step a desorption cycle was conducted.

5. Impact of the thermal stabilization parameters on the pore structure of carbon nanofibers

5.1. Preface

This chapter discusses the impact of stabilization duration, temperature and atmosphere on the gas adsorption properties of electrospun carbon nanofibers. For each parameter, a detailed chemical characterization is conducted prior to the discussion of its impact on the pore structure and gas adsorption properties. The results of this chapter were obtained in collaboration with Maya Pagel, who conducted the experimental work and parts of the data processing during her Master thesis under supervision of Tom Fischer [130]. Elemental analysis was performed by the Central Institute of Analytics at Forschungszentrum Jülich GmbH. Raman measurements were conducted by Sebastian Speer and evaluated by Tom Fischer. Main parts of this chapter have been previously published under a CC BY 4.0 license in Carbon Trends [131].

5.2. Impact of the stabilization duration

The thermal stabilization was conducted at 250 °C in air at durations of 0.5, 1, 4, 8 and 15 h. Additionally, carbon nanofibers without any stabilization treatment were prepared (0 h).

5.2.1. Characterization

During thermal stabilization the white PAN nanofibers underwent a distinct color change to dark brown or black, respectively. At durations of 0.5 to 1 h the stabilized nanofibers turned dark brown, whereas at durations larger than 4 h a black color was obtained

(Figure 5.1). The color change is typical for PAN fibers during thermal stabilization and is assigned to the conjugated π-network of the stabilized ladder polymer [132].

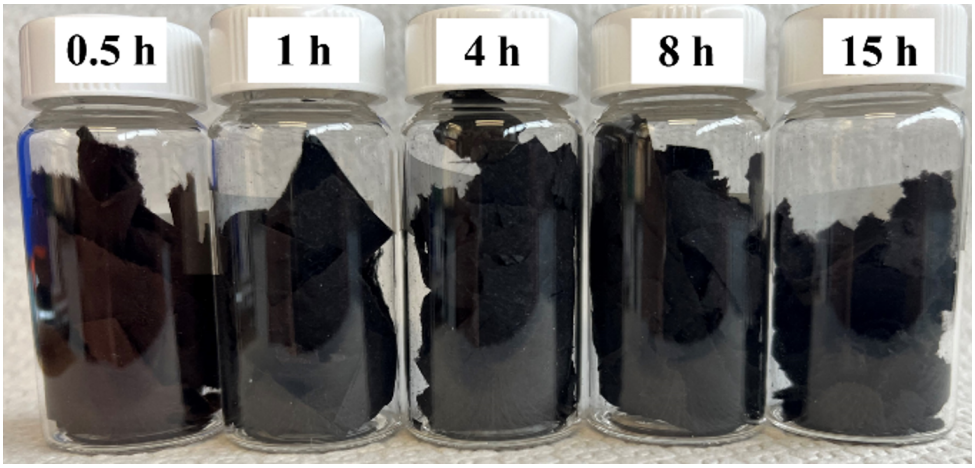


Figure 5.1. – PAN-based nanofibers after thermal stabilization at 250 °C in air for 0.5, 1, 4, 8 and 15 h. A color change from white to dark brown or black was observed.

Infrared Spectroscopy

In-depth characterization of the ongoing chemical changes was conducted by FT-IR spectroscopy (Figure 5.2a). The non-stabilized PAN nanofibers (0 h) spectrum shows four distinct absorption bands. At 2931 cm^{-1} CH_2 valence vibrations (ν_{CH_2}) are observed, which are assigned to the backbone CH_2 groups of PAN. Additionally, deformation vibrations of these groups (δ_{CH_2}) are visible at 1454 cm^{-1}. The sharp absorption band at 2243 cm^{-1} is caused by the valence vibration of the nitrile groups ($\nu_{C\equiv N}$). The fourth absorption band at 1662 cm^{-1} is related to carbonyl valence vibrations ($\nu_{C=O}$), which are not directly related to PAN, but can be assigned to additives or impurities of the precursor.

At increasing stabilization duration, a significant decrease of $\nu_{C\equiv N}$ as well as a vanishing of ν_{CH_2} is observed. Simultaneously, new absorption bands at 1590, 1334, 1240 and 801 cm^{-1} arise. The vibrations at 1590 cm^{-1} are assigned to $-C=N-$ and $-C=C-$ valence vibrations ($\nu_{C=C/C=N}$) of the stabilized ladder polymer, whereas the vibrations at 1334 cm^{-1} are deformation vibrations of CH groups (δ_{CH}) in the cyclized structure [71, 133, 134]. The absorption at 1240 cm^{-1} is most likely related to oxygen containing functional groups, e.g. carbonyl or hydroxyl groups. Additionally, the signal at 801 cm^{-1} is assigned to out-of-plane vibrations (δ_{oop}) of the aromatic hydrogen atoms [134]. Furthermore, a broad absorption band between 2300 and 3700 cm^{-1} arises in

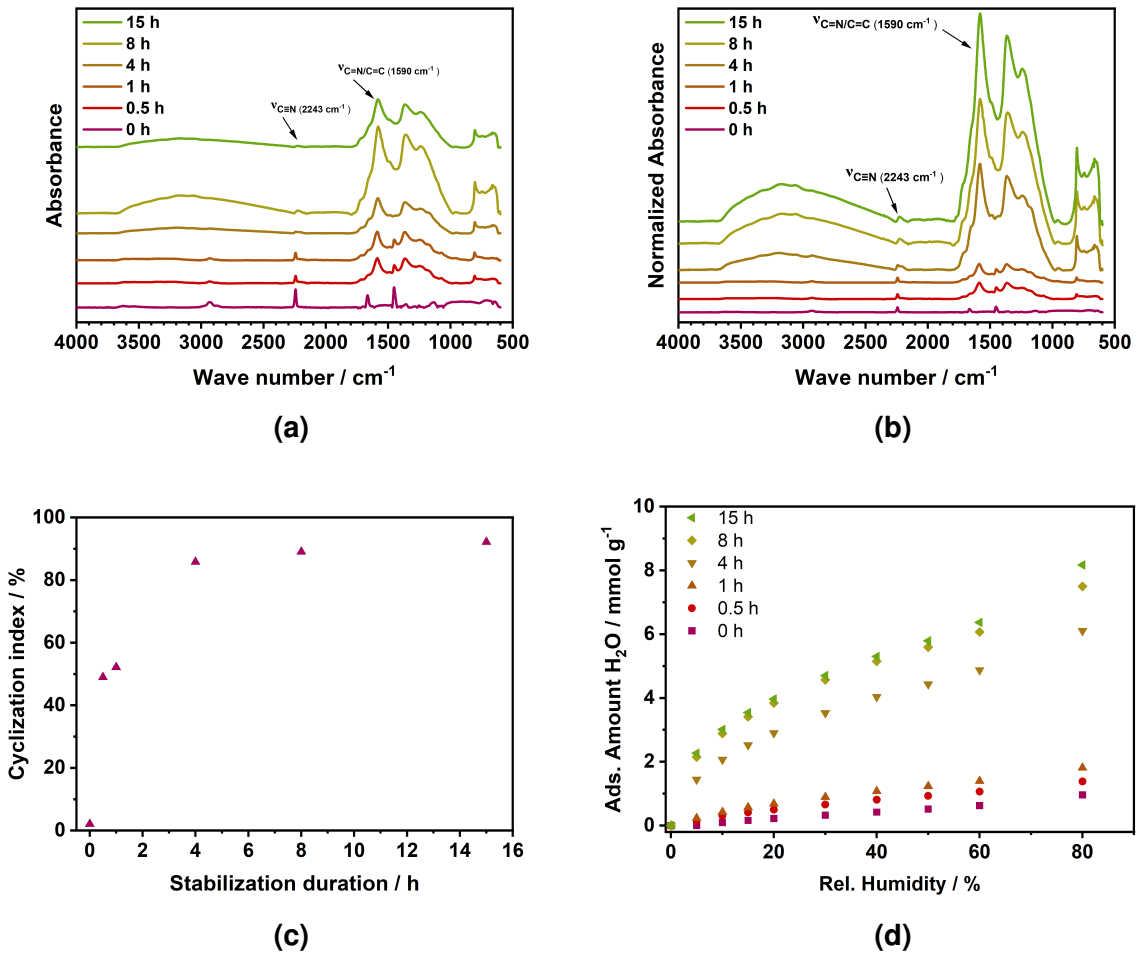


Figure 5.2. – (a) IR spectra of thermally stabilized PAN-based nanofibers. Stabilization was conducted at 250 °C in air for 0.5, 1, 4, 8 and 15 h. Non-stabilized PAN nanofibers are shown as 0 h. (b) IR spectra normalized to the height of the nitrile valence vibration band of non-stabilized sample to ensure comparability between the samples. (c) Cyclization index for the stabilized nanofibers, which was calculated using Equation 4.1 and the normalized absorption band heights of the nitrile and $-C=N-/-C=C-$ valence vibrations. (d) H_2O vapor isotherms at 298 K on PAN-based nanofibers stabilized at 0-15 h duration.

the spectra of the stabilized nanofibers at durations $\geq$ 4 h. This is assigned to ν_{O-H} of adsorbed water. The H_2O adsorption on these samples was investigated in vapor sorption experiments (Figure 5.2d). An increase of the H_2O adsorption with prolonged stabilization duration was observed, which is assigned to the higher polarity of these stabilized nanofibers. This is caused by an increased number of polar surface groups due to oxygen incorporation. After a stabilization duration of 4 h, $\nu_{C\equiv N}$ almost disappeared, whereas $\nu_{C=C/C=N}$ increased steadily, which indicates a high progress of the cyclization reactions.

To assess the progress of stabilization, the cyclization index based on the absorption band height of $\nu_{\mathrm{C\equiv N}}$ at 2243 cm^{-1} and $\nu_{\mathrm{C=C/C=N}}$ at 1590 cm^{-1} was calculated (Equation 4.1). To ensure comparability, the spectra were normalized to the height of $\nu_{\mathrm{C\equiv N}}$ of the non-stabilized nanofibers (0 h) (Figure 5.2b). Within the first hour of stabilization a steep rise to 52 % is obtained, which further increases up to 87 % for 4 h stabilization duration (Figure 5.2c). At longer stabilization durations only a small additional rise of the cyclization index to a maximum of 92 % is determined. These calculated cyclization indices match well to the qualitatively discussed changes in the FT-IR spectra and show the impact of the stabilization duration on the chemical structure of PAN nanofibers.

Elemental Analysis

Additionally, elemental analysis was conducted to determine changes in the elemental composition for all PAN-based nanofibers after stabilization and after carbonization (Figure 5.3).

After stabilization a reduction of the C fraction from 65.6 wt.-% to 52.5 wt.-% with increasing stabilization duration is observed (Figure 5.3a). This decrease is mainly caused by the incorporation of oxygen into the stabilized ladder structure due to oxidation reactions. The incorporation of oxygen is clearly visible in the continuous increase of the oxygen fraction from 2.8 to 24.3 wt.-%, which approaches a limiting value at stabilization durations longer than 4 h. Simultaneously, a decrease of the N fraction from 26.0 wt.-% to 19.9 wt.-% is observed. This is most likely caused by the oxygen incorporation, since no significant nitrogen elimination during thermal stabilization is expected [75]. The reduction of the H fraction from 6.0 wt.-% to 3.1 wt.-% indicates ongoing dehydrogenation reactions. However, it is affected by the parallelly occurring reactions and therefore cannot be seen as a reliable measure for the dehydrogenation reactions.

After carbonization, the differences in elemental composition between the samples are diminished compared to the samples, which were only stabilized. In particular, the removal of heteroatoms is observed. This reduction in heteroatom content is evident in the decreased oxygen fraction after the carbonization (Figure 5.3b). In contrast to the measurements performed after stabilization, the oxygen fraction increases just from 8.3 wt.-% to 11.6 wt.-% with increasing stabilization duration. The oxygen:carbon ratio decreased about 60 % for carbonized samples, which were stabilized $\geq$ 4 h, compared to after stabilization (Figure 5.3c). The removal of oxygen during carbonization could occur via condensation reactions between adjacent stabilized ladder polymers [75]. The increase of the oxygen:carbon ratio for carbonized samples, which were stabilized $\leq$ 4 h,

compared to the oxygen:carbon ratio after stabilization is caused by the small degree of oxygen incorporated during stabilization.

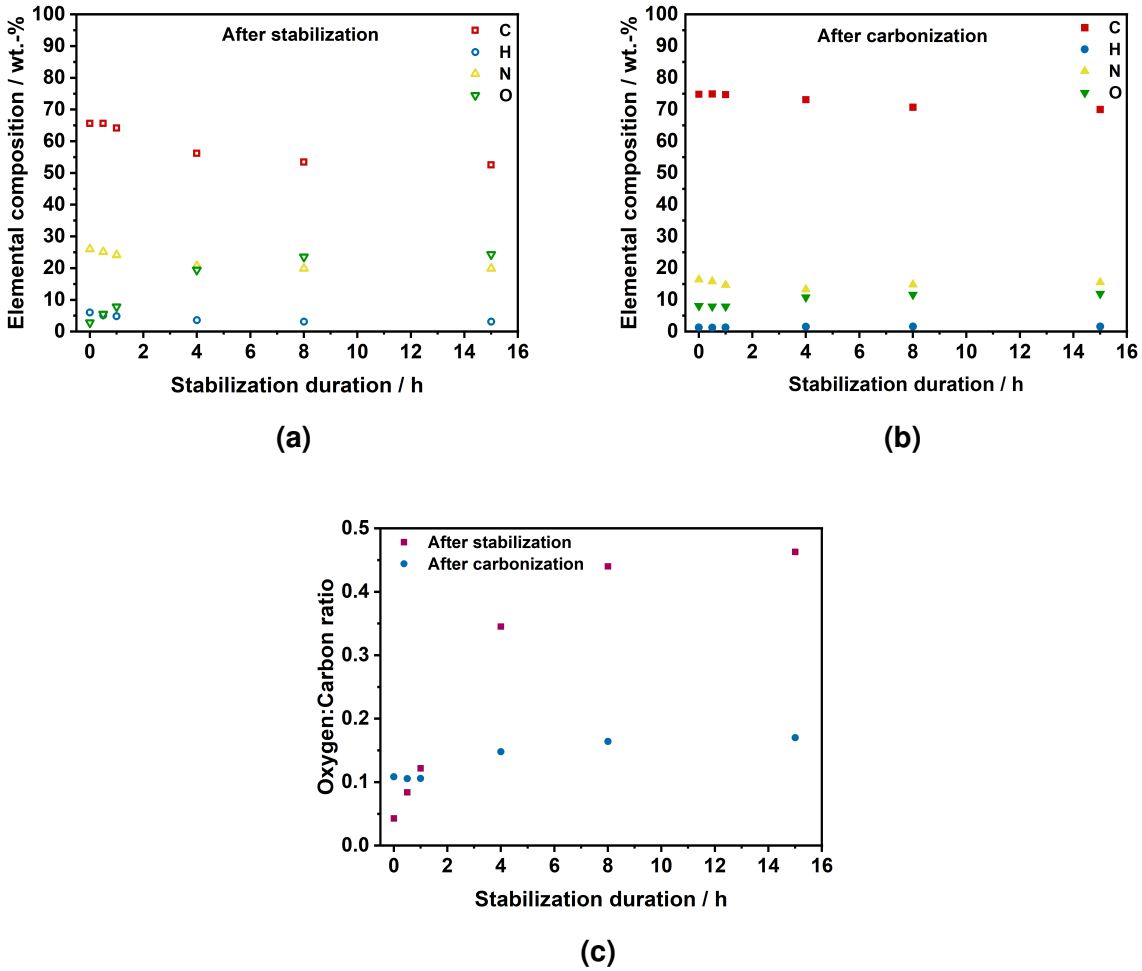


Figure 5.3. – C, H, N, O elemental analysis of PAN-based nanofibers measured (a) after stabilization and (b) after carbonization. The stabilization duration was varied for 0, 0.5, 1, 4, 8 and 15 h at 250 °C in air. Subsequent carbonization was conducted at 800 °C in Ar for 3 h. (c) Oxygen:Carbon ratio of the carbon nanofibers after stabilization and after carbonization.

Thus, the removal of carbon surpasses the removal of oxygen during carbonization. Similar to the oxygen fraction, a slight reduction of the H and N fractions is obtained after carbonization. This is expected due to N elimination and dehydrogenation reactions during carbonization. Within the sample series, only a slight decrease with longer stabilization durations is visible. Due to the removal of heteroatoms during carbonization the carbon fraction increases by 10 to 18 wt.-% compared to the stabilized nanofibers. The resulting carbon fraction is at 74.7 wt.-% for the non-stabilized carbon nanofibers and decreases slightly to 70.0 wt.-% after 15 h stabilization duration.

Raman Spectroscopy

Due to the higher stabilization progress at long durations, larger stabilized ladder polymers are expected. These and additional crosslinking reactions via condensation due to the increased oxygen content, could result in the growth of larger carbon frameworks during the carbonization step. Such larger carbon frameworks potentially result in a higher degree of structural order in the carbon nanofibers. To assess the degree of structural order the D_1/G ratio of the carbon nanofibers was determined by Raman spectroscopy (Figure 5.4).

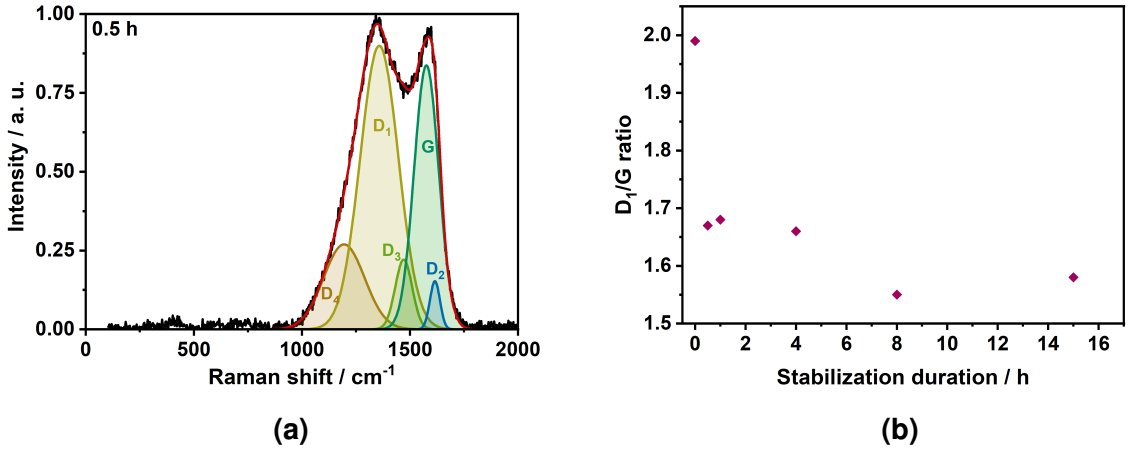


Figure 5.4. – (a) Raman spectrum of carbon nanofibers stabilized at 0.5 h in air with subsequent carbonization for 3 h at 800 °C in Ar. The D and G bands were fitted using 5 Gaussian peaks D_1, D_2, D_3, D_4 and G. (b) D_1/G ratio of the carbon nanofibers stabilized between 0 and 15 h obtained by integration of the area of D_1 and G band.

The characteristic G band of a carbon material at 1580 cm^{-1} is related to the E_{2g} vibrations of the graphite crystal lattice, whereas the D band at 1360 cm^{-1} is related to defects and disorder in the amorphous regions [127, 135]. Five Gaussian fits were used to fit the D and G region of the carbon nanofibers. One Gaussian fit was used for the G band and the D band was fitted using four fits assigned to D_1, D_2, D_3 and D_4 defects (Figure 5.4a) [126, 127]. The Raman fits for all samples are attached in appendix section A.2.

At 0 h stabilization duration the D_1/G ratio is at 1.99. After 0.5 h stabilization a steep decrease to 1.67 is observed, reflecting an increased structural order of the carbon nanofibers. The decrease of the D_1/G ratio continuous at an attenuated course to a value of 1.58 after 15 h stabilization duration (Figure 5.4b). Considering the results of the IR and elemental analysis, this increased structural order of carbon nanofibers stabilized at long durations can be related to the growth of larger stabilized ladder

structures during thermal stabilization. The formation of larger stabilized structures results in larger carbon frameworks after carbonization. In addition to the increased size of the stabilized ladder structures, the increased incorporation of oxygen could result in additional crosslinking reactions through the condensation of carbonyl groups, accompanied by the elimination of H_2O during carbonization [51, 75]. Both, the larger stabilized ladder structures and the additional crosslinks would impact the developed carbon framework and thus influence the structural order of the carbon nanofibers.

Scanning Electron Microscopy

The carbonized nanofibers were investigated by SEM to assess the dimensional stability of the nanofibers and changes in orientation and thickness (Figure 5.5). The SEM images show randomly arranged carbon nanofibers without any visible trend at increased stabilization duration. The fiber diameter varies between the single fibers of one sample, but no growth or shrinkage in relation to the duration time was found. Therefore, a sufficient stabilization was achieved on all samples. The variation in fiber diameter is caused by the needleless electrospinning process of the PAN fibers and neither caused by the stabilization or the carbonization process.

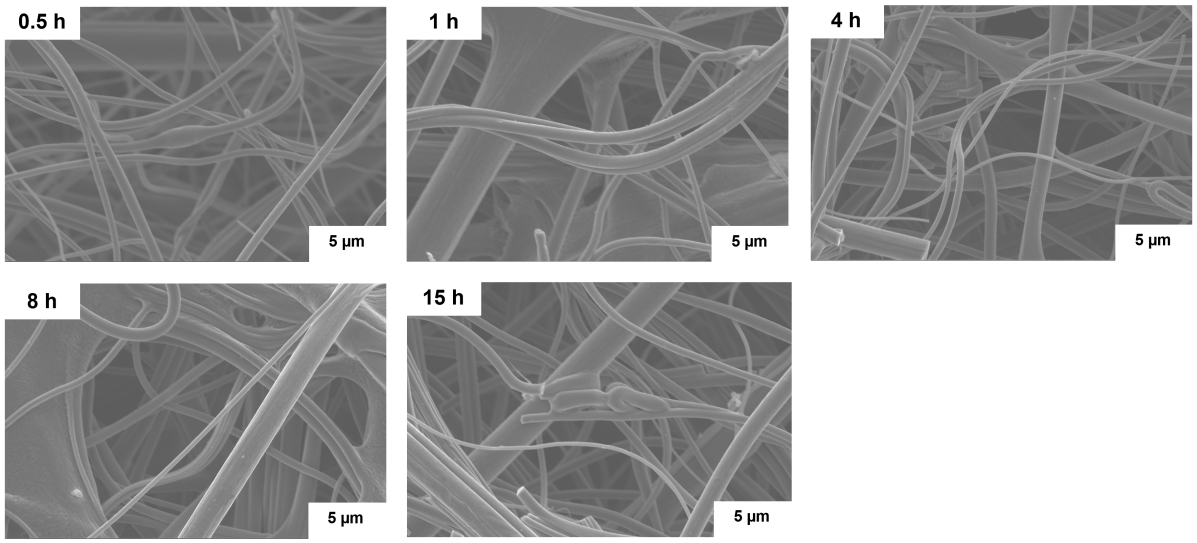


Figure 5.5. – SEM images of carbon nanofibers stabilized at 250 °C for durations of 0.5, 1, 4, 8 and 15 h in air. Subsequently, all carbon nanofibers were carbonized for 3 h at 800 °C. The images were recorded after carbonization.

5.2.2. Impact on the pore structure

To analyse the impact of the stabilization duration on the pore formation of the carbon nanofibers, Ar and CO_2 adsorption isotherms were recorded and evaluated. All isotherm measurements were conducted on carbonized samples.

For all samples the Ar adsorption isotherms show a type II shape with less than 0.5 mmol g^{-1} Ar capacity (Figure 5.6a). These isotherms are typical for non-porous adsorbents or adsorbents with pores inaccessible for the used adsorptive [93]. No trends between the stabilization duration and the Ar adsorption isotherms of the samples are observed. Based on the Ar isotherms the BET area was determined, which is between 3 to 7 m^2 g^{-1} on all samples (Table 5.1). Additionally, the isotherm data was used to calculate the pore size distribution by QSDFT calculations using a kernel for slit pores on carbon (Figure 5.6b, Table 5.1). Negligible cumulative pore volumes of less than 0.011 cm^3 g^{-1} were obtained. Both, BET area and pore size distribution, match well the expectations based on the isotherm shape.

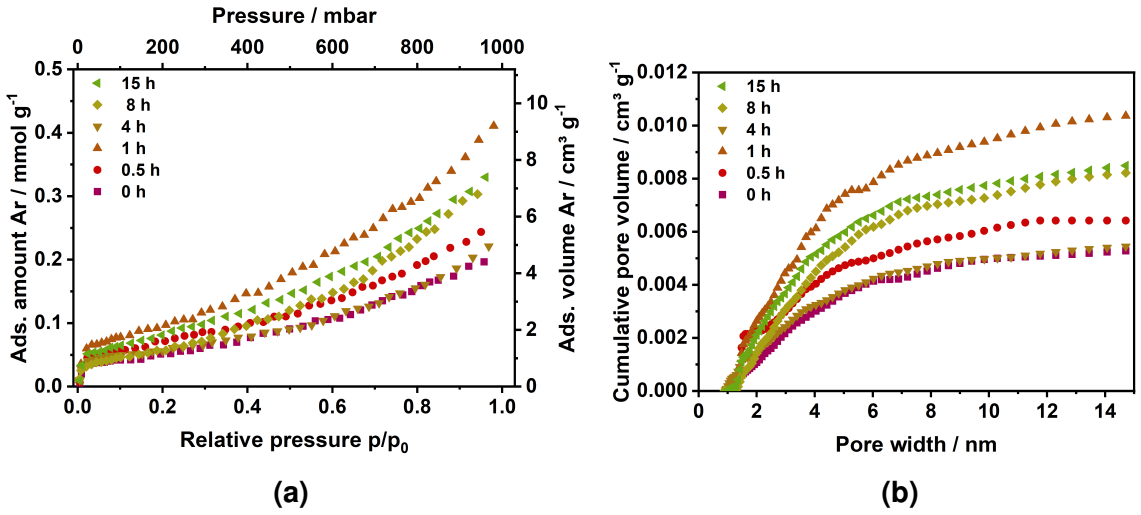


Figure 5.6. – (a) Ar isotherms measured at 87 K on carbon nanofibers stabilized at durations of 0, 0.5, 1, 4, 8 and 15 h. (b) Cumulative pore size distribution calculated by QSDFT calculations using a kernel for slit pores on carbon.

To assess the supermicropore (V_{Super}) and ultramicropore volume (V_{Ultra}) of the carbon nanofibers, CO_2 adsorption isotherms at 273 K were measured. For non-stabilized carbon nanofibers (0 h) the isotherm shows an almost linear course with a negligible CO_2 uptake at relative pressures < 0.01 (Figure 5.7a). At higher relative pressures the capacity increases to 0.37 mmol g^{-1}. At longer stabilization durations the shape of the CO_2 adsorption isotherm changes significantly. Already after 0.5 and 1 h stabilization duration the isotherm slope in the low-pressure region (< 0.01) rises and the adsorption

capacity at 1 bar increases to 1.36 (0.5 h) and 1.88 mmol g^{-1} (1 h). For stabilization durations exceeding 4 h this trend continues, and the adsorption isotherms turn into a type I shape. Such isotherm shapes are characteristic for highly microporous adsorbents. The CO_2 adsorption capacity at 1 bar approaches a limiting value of 2.86 mmol g^{-1} on carbon nanofibers stabilized for 8 and 15 h.

Table 5.1. – BET area, ultramicropore volume (V_{Ultra}), supermicropore volume (V_{Super}), mesopore volume (V_{Meso}), DFT pore volume (V_{DFT}) and Monte-Carlo pore volume (V_{MC}) for carbon nanofibers stabilized at 250 °C for durations of 0, 1, 4, 8 and 15 h in air. Subsequently, a carbonization was conducted at 800 °C for 3 h in Ar.

Duration	BET Area	V_{DFT}	V_{MC}	V_{Ultra}	V_{Super}	V_{Meso}
h	$m^2\,g^{-1}$	$cm^3\,g^{-1}$	$cm^3\,g^{-1}$	$cm^3\,g^{-1}$	$cm^3\,g^{-1}$	$cm^3\,g^{-1}$
0	3.2	0.005	0.034	0.001	0.034	0.004
0.5	4.7	0.006	0.103	0.053	0.050	0.004
1	6.7	0.011	0.116	0.079	0.038	0.008
4	3.9	0.005	0.152	0.098	0.054	0.004
8	4.4	0.008	0.152	0.118	0.035	0.008
15	5.9	0.008	0.164	0.110	0.055	0.007

Based on the CO_2 adsorption isotherms the pore size distribution was determined using Monte-Carlo calculations with a kernel for slit pores on carbon (Figure 5.7b, Table 5.1). On carbon nanofibers without thermal stabilization (0 h) a negligible V_{Ultra} is present. Between 0.7 and 0.9 nm a steep increase of the pore volume to 0.039 $cm^3\,g^{-1}$ is visible. At larger pore widths the pore volume remains almost constant. For longer stabilization durations V_{Ultra} of the carbon nanofibers significantly increases to 0.118 $cm^3\,g^{-1}$ (8 h). Since Ar and CO_2 pore size distributions cover only particular pore width regions, both were combined to give a holistic description of the pore size distributions (Figure 5.7c). V_{Ultra} is taken from Monte-Carlo calculations, whereas V_{super} is a combination of Monte-Carlo (CO_2) and QSDFT (Ar) calculations and the V_{Meso} is solely based on the QSDFT calculations. As discussed previously, a distinct increase of V_{Ultra} is obtained at longer stabilization durations. However, far less changes are observed in V_{Super} and V_{Meso}. The V_{super} of the non-stabilized carbon nanofibers (0 h) was at 0.034 $cm^3\,g^{-1}$ and increased to 0.055 $cm^3\,g^{-1}$ for 15 h stabilization duration. However, no clear correlation to the increasing stabilization duration is visible. V_{Meso} stays on a negligible level and varies between 0.004 $cm^3\,g^{-1}$ for 0.5 h and 0.007 $cm^3\,g^{-1}$ for 15 h stabilization without a significant influence of the duration (Table 5.1). Overall, a high impact of the stabilization duration on the pore formation of the carbon nanofibers is found. Especially, the formation of V_{Ultra} highly depends on the progress of the stabilization reactions.

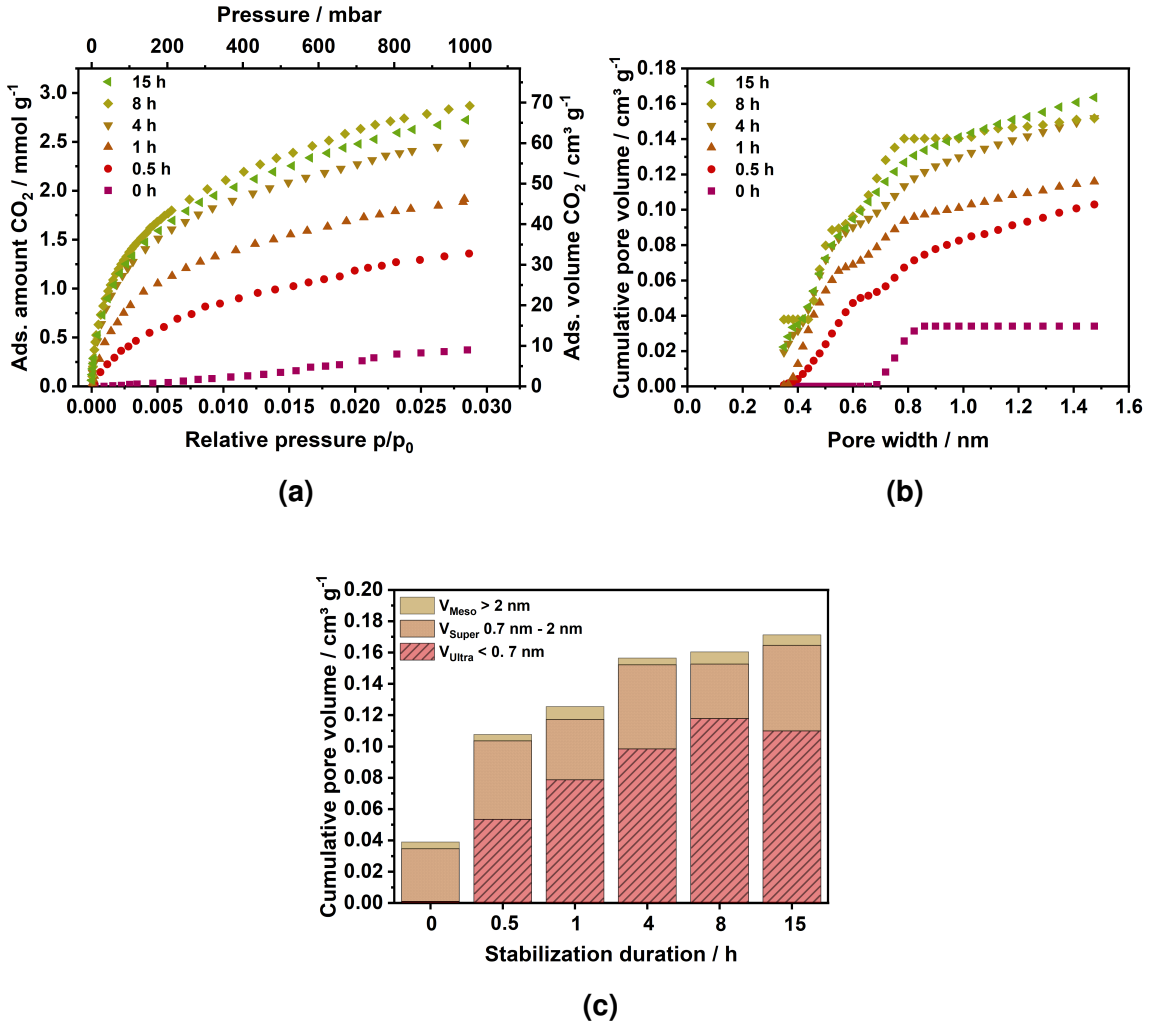


Figure 5.7. – (a) CO_2 isotherms measured at 273 K at carbon nanofibers stabilized at durations of 0, 0.5, 1, 4, 8 and 15 h. (b) Cumulative pore size distribution calculated using Monte-Carlo calculations with a kernel for slit pores on carbon. (c) Cumulative pore size distribution for carbon nanofibers stabilized at durations from 0 to 15 h divided into V_{ultra}, V_{meso} and V_{super}. The shown data is a combination of QSDFT calculations using Ar isotherms and Monte Carlo simulations using CO_2 adsorption isotherms.

5.3. Impact of the stabilization temperature

As a further process parameter, the stabilization temperature and its impact on the pore structure of the carbon nanofibers was investigated. In the course of the experiments, the temperature was varied from 200 to 300 °C in intervals of 25 °C and the stabilization duration was fixed to 1 h. The stabilized nanofibers were characterized and afterwards carbonized at 800 °C for 3 h in Ar. Finally, the carbon nanofibers were characterized and analyzed regarding their pore structure.

5.3.1. Characterization

Similar to the variation of stabilization duration, a color change from white to brownish was observed during thermal stabilization. Depending on the stabilization temperature a color change from light brown to dark black is observed. At 200 °C a light brown color is obtained, turning into dark brown at 250 °C and almost into black at 300 °C. Compared to the coloration by variation of the stabilization duration the variation in color is more pronounced. This indicates a stronger effect of the stabilization temperature on the stabilization process. In total, the observations are in good agreement to literature and the color change can be related to the formation of the conjugated double bonds due to cyclization reactions [132].

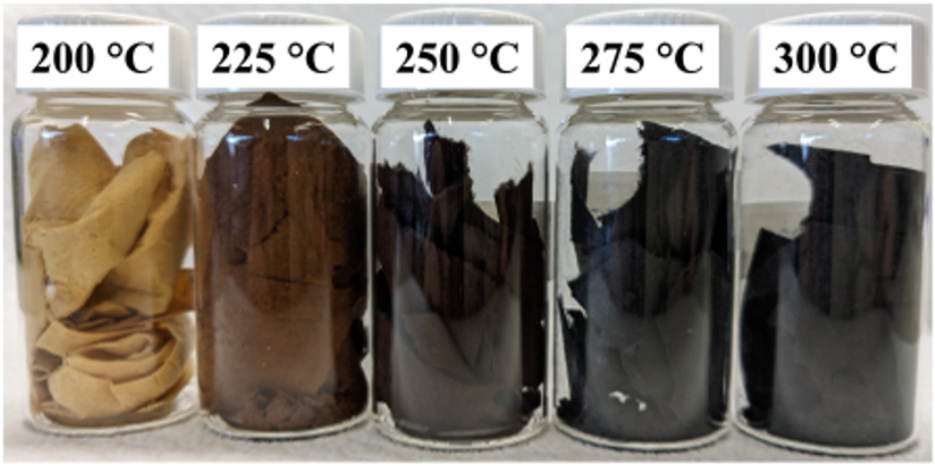


Figure 5.8. – Thermally stabilized PAN-based nanofibers at temperatures ranging from 200-300 °C at intervals of 25 °C. A color change from light brown to dark black with increase of stabilization temperature is visible.

IR Spectroscopy

The chemical changes of the PAN structure depending on the stabilization temperature were investigated by FT-IR spectroscopy (Figure 5.9a). The nanofibers stabilized at 200 °C show a sharp nitrile absorption band $\nu_{\mathrm{C\equiv N}}$ at 2243 cm^{-1}. Additionally, the $\nu_{\mathrm{CH_2}}$ and $\delta_{\mathrm{CH_2}}$ vibrations of the polymer backbone are visible at 2930 cm^{-1} and 1454 cm^{-1}, respectively. At increased stabilization temperatures the intensity of $\nu_{\mathrm{C\equiv N}}$ decreases and the $\delta_{\mathrm{CH_2}}$ vibrations are increasingly overlapped by several absorption bands in the region of 1700-1000 cm^{-1}. As already discussed in the chapter on the stabilization duration, these arise from δ_{CH} vibrations of the cyclized structures as well as absorption bands related to oxygen containing functional surface groups, e.g. hydroxyl, carbonyls.

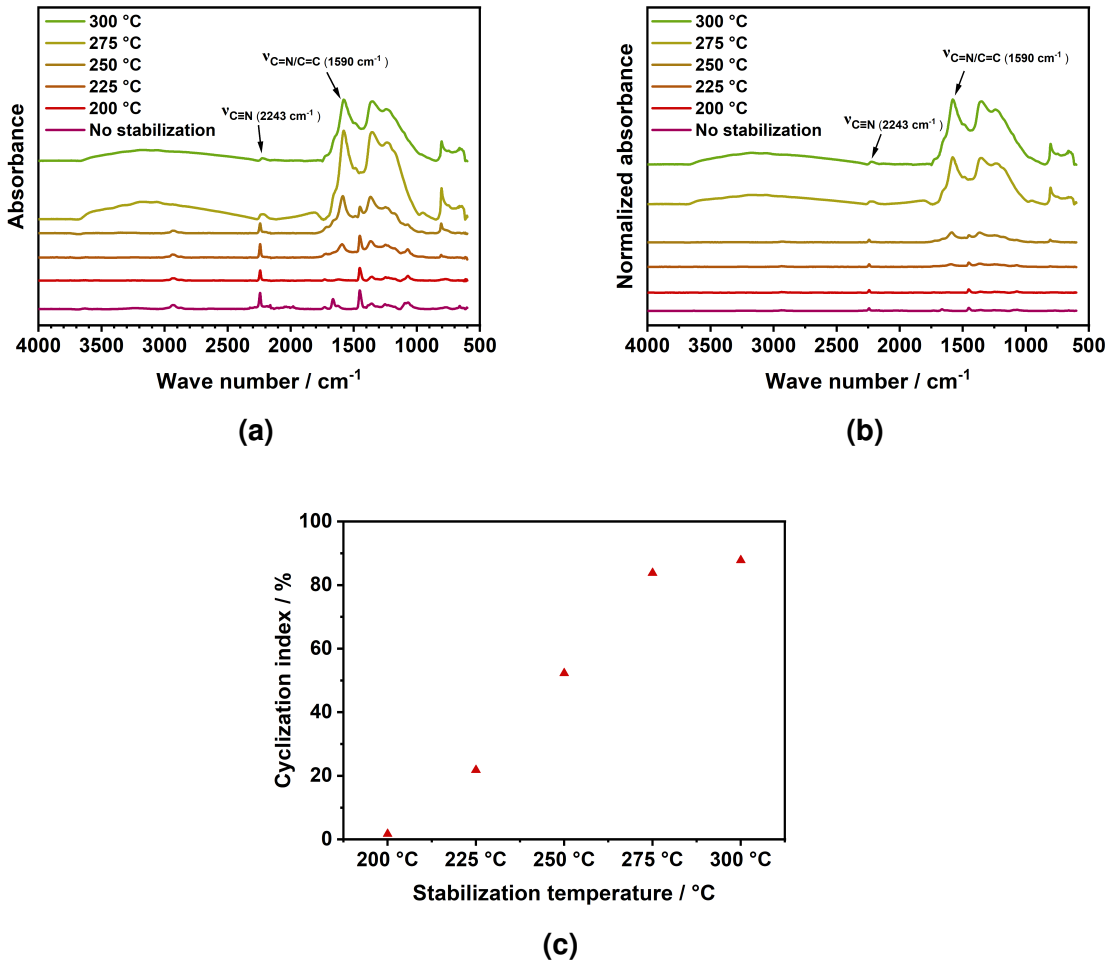


Figure 5.9. – (a) FT-IR ATR spectra of PAN-based nanofibers stabilized at temperatures of 200, 225, 250, 275 and 300 °C for 1 h in air. (b) Cyclization index calculated from absorption band height of nitrile valence vibration and C=N/C=C valence vibrations.

Additionally, a narrow absorption band at 801 cm^{-1} reflecting the out-of-plane vibrations of the aromatic-H is visible on samples stabilized at temperatures higher than 250 °C. Moreover, a broad absorption band between wave numbers of 2200-3700 cm^{-1} is observed.

This is assigned to ν_{O-H} of adsorbed water attracted by an increased number of polar surface groups due to oxygen incorporation. This increased water adsorption was confirmed for the samples at long stabilization durations (Figure 5.2d).

As measure of the stabilization progress, the cyclization index was calculated based on Equation 4.1. To ensure comparability all spectra were normalized to the maximum height of the nitrile valence vibration band ($\nu_{C\equiv N}$) of the non-stabilized sample (Figure 5.9b). At 200 °C a low cyclization index of just 2.6 % was determined (Figure 5.9c).

At higher stabilization temperatures, this index increases steadily and reaches a value of 53.3 % at a stabilization temperature of 250 °C. Afterwards, it approaches a maximum of 85-87 % at stabilization temperatures of 275 and 300 °C. The determined cyclization indices agree well to the qualitative discussion of the IR spectra and clearly show the distinct impact of the stabilization temperature on the formation of the stabilized ladder polymer.

Elemental Analysis

To determine changes in the elemental composition, the C, H, N and O fractions of the stabilized nanofibers and the carbon nanofibers were analyzed (Figure 5.10). The carbon fraction of the stabilized nanofibers decreased with increasing stabilization temperatures from 66.1 wt.-% (200 °C) to 54.7 wt.-% (300 °C) (Figure 5.10a). Simultaneously, the N fraction decreased by 5.7 wt.-% from 26.2 wt.-% to 20.5 wt.-% and the H fraction from 6.0 wt.-% to 3.0 wt.-%. Contrarily, a significant increase of the oxygen fraction from 1.9 wt.-% to 21.5 wt.-% was observed. This significant increase of the oxygen fraction is caused by the incorporation of oxygen into the stabilized ladder polymer resulting in carbonyl, carboxyl and hydroxyl functional groups [65]. The high oxygen incorporation causes the relative decrease of the C, N and H fractions. Additionally, the decrease of the H fraction is caused by the dehydrogenation reactions during stabilization.
Comparing the influence of stabilization temperature and duration on the elemental composition, similar effects were observed for longer duration as well as higher temperatures. This indicates comparable impacts of duration and temperature on the stabilization reactions.
After carbonization the C fraction of the carbon nanofibers stabilized at different temperatures lies between 70.9 and 74.7 wt.-%, decreasing slightly at higher stabilization temperatures (Figure 5.10b). The N and H fractions remain almost constant between 14.1 to 16.3 wt.-% and 1.2 to 1.6 wt.-%, respectively. In contrast, the O fraction is increased for higher stabilization temperatures from 7.3 to 15.0 wt.-%. Compared to the elemental composition after stabilization a 10 to 15 wt.-% increase of the carbon fraction is obtained on the carbonized samples. This increase and the simultaneous decrease of the heteroatom content was expected due to the reactions during carbonization, which involve the removal of heteroatoms. Thus, the high amount of oxygen, which was incorporated during stabilization at stabilization temperatures > 250 °C, almost vanished after carbonization. This is assigned to a high number of crosslinking condensation reactions between the stabilized ladder polymers. The high removal of oxygen during carboniza-

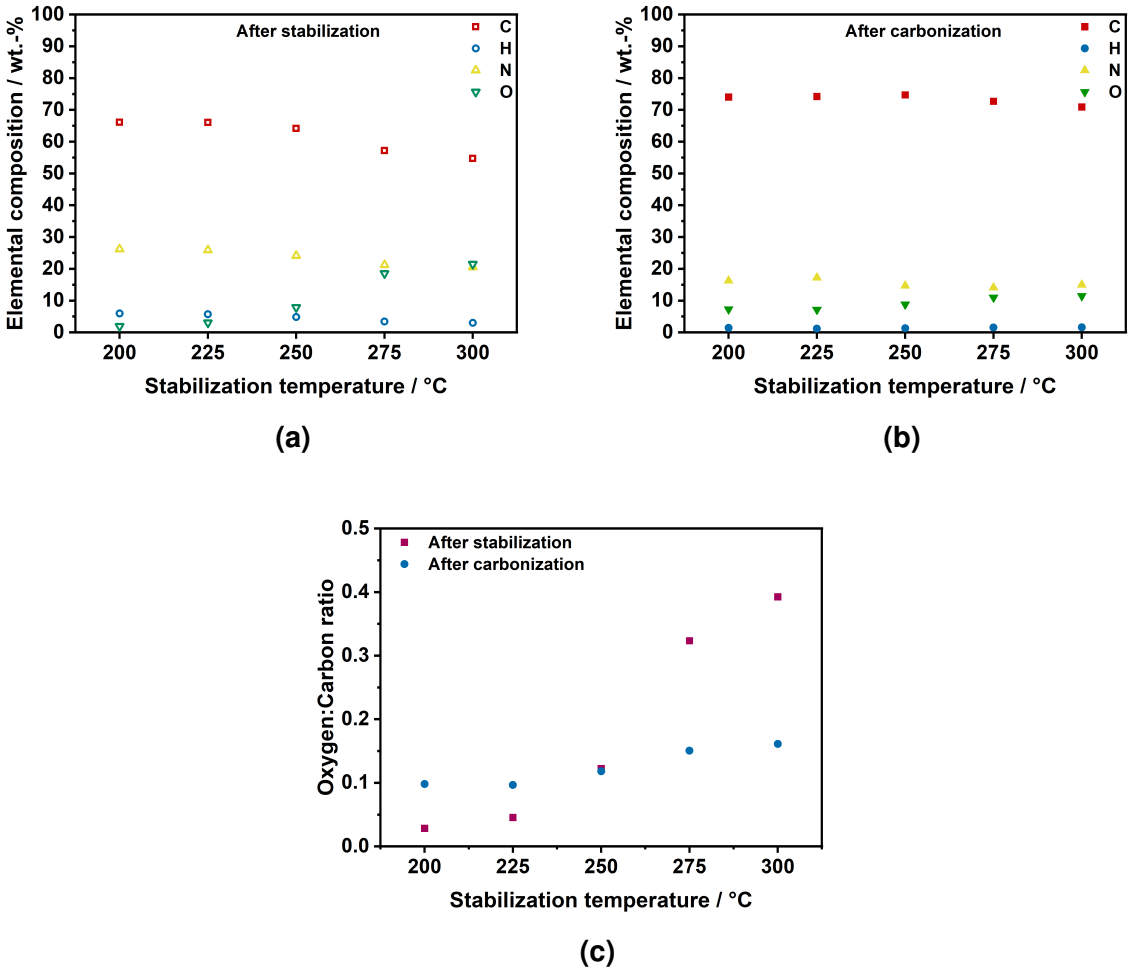


Figure 5.10. – (a) CHNO elemental analysis of PAN-based nanofibers stabilized at 200, 225, 250, 275 and 300 °C for 1 h in air. Measured directly after stabilization. (b) CHNO elemental analysis of PAN-based carbon nanofibers stabilized at 200, 225, 250, 275 and 300 °C for 1 h in air. Measured after carbonization at 800 °C in Ar for 3 h. (c) Oxygen:Carbon ratio after stabilization and after carbonization of the investigated carbon nanofibers.

tion is reflected in a distinct decrease of the oxygen:carbon ratio (Figure 5.10c). On samples stabilized at temperatures lower than 250 °C the nanofibers contain only small fractions of oxygen, thus the oxygen removal is surpassed by carbon removal during carbonization. This explains the increased oxygen:carbon ratio after carbonization.

Raman Spectroscopy

The larger stabilized ladder polymers and the proposed higher number of condensation reactions between the stabilized ladder polymers during carbonization might result in the formation of larger carbon frameworks, as observed for the samples stabilized at different durations. Therefore, Raman spectroscopy was used to assess the degree of

structural order by evaluation of the D_1/G ratio. In Figure 5.11a the characteristic D and G band region of the Raman spectrum of the carbon nanofibers is depicted. Five Gaussian fits, D_1, D_2, D_3, D_4 and G are used and by integration of the D_1 and the G peak area, the D_1/G ratio was determined. In Figure 5.11b a decrease of the D_1/G

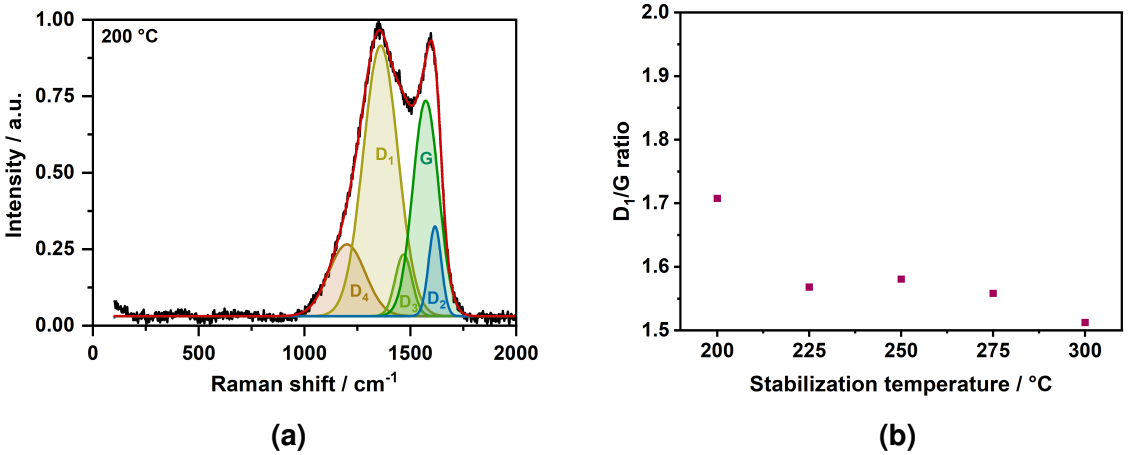


Figure 5.11. – (a) D and G band region of carbon nanofibers with 5 Gaussian fits for D_1, D_2, D_3, D_4 and G peak. (b) D_1/G ratio to determine the degree of structural order. All Raman measurements were conducted after carbonization.

ratio from 1.71 to 1.51 at increasing stabilization temperature is visible. This is assigned to an increased structural order for carbon nanofibers stabilized at higher temperatures. As the carbonization conditions were kept constant for all samples, the differences in the structural order are related to the stabilization process and the stabilization temperature, respectively.

Scanning Electron Microscopy

The thermal stabilization of PAN nanofibers is seen as essential step to keep the dimensional stability during carbonization. To identify potential insufficient stabilization conditions, changes of the carbon nanofiber morphology were investigated using SEM (Figure 5.12).

All carbon nanofiber samples showed randomly aligned carbon nanofibers without any preferred orientation, independent of the applied stabilization temperatures. For each sample a broad distribution of the fiber diameter is observed ranging from 200 nm to roughly 1 µm. However, no variation of the fiber diameter in relation to the stabilization temperatures was identified. Therefore, the variation in fiber diameter is related to

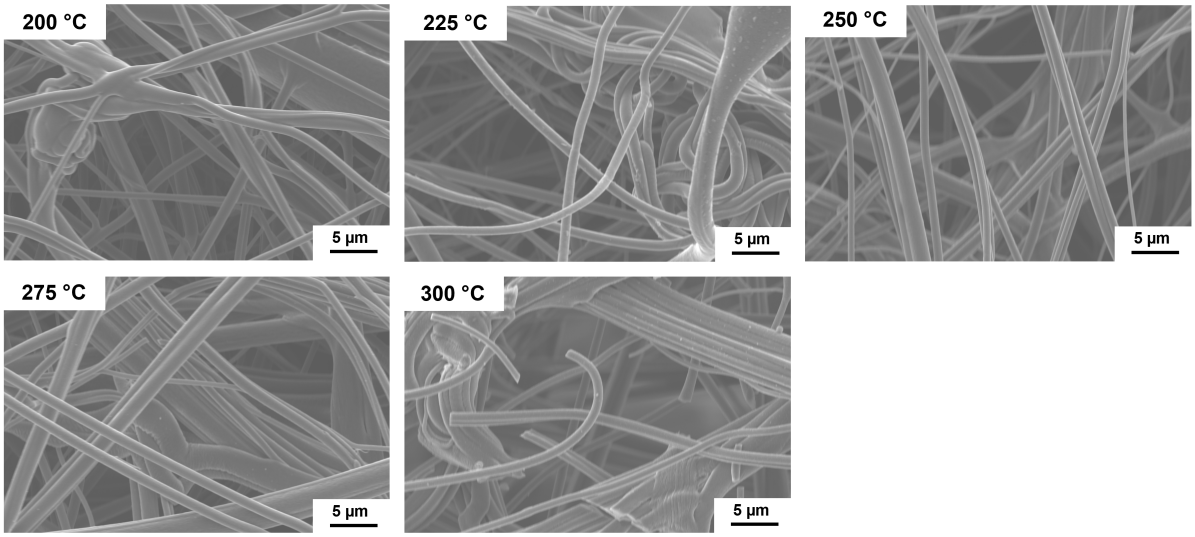


Figure 5.12. – SEM images of carbon nanofibers stabilized at 200, 250 and 300 °C for 1 h in air. The differences in fiber diameter are attributed to the electrospinning process and not to the applied stabilization conditions.

the used needleless electrospinning process. Such a spinning process allows higher production rates, but often yields less homogeneous fiber diameters [136].
Nonetheless, at all stabilization temperatures proper carbon nanofibers were obtained after carbonization. Thus, no effect of stabilization temperature on the dimensional stability during the carbonization was found.

5.3.2. Impact on the pore structure

The results of the previous chapters, indicate significant changes of the pore structure and the gas adsorption properties of the carbon nanofibers. Therefore, Ar and CO_2 were used to determine the gas adsorption properties and yield information on the pore size distribution of the materials.
In Ar adsorption measurements, all samples showed type II isotherms with capacities less than 0.5 mmol g^{-1} at 1 bar (Figure 5.13a). Within the sample series no trends with respect to the stabilization temperature were observed. Based on the Ar isotherms the BET area was determined, which was below 7 $m^2 g^{-1}$ for all samples (Table 5.2). Additionally, the pore size distribution was calculated based on a QSDFT model for slit pores on carbon. Negligible cumulative pore volumes of up to 0.011 $cm^3 g^{-1}$ were determined (Figure 5.13b, Table 5.2). Overall, the isotherm shape, the low Ar capacities, the small BET area and the negligible cumulative pore volume are typical for a non-porous adsorbent or an adsorbent with pores inaccessible for the adsorptive.

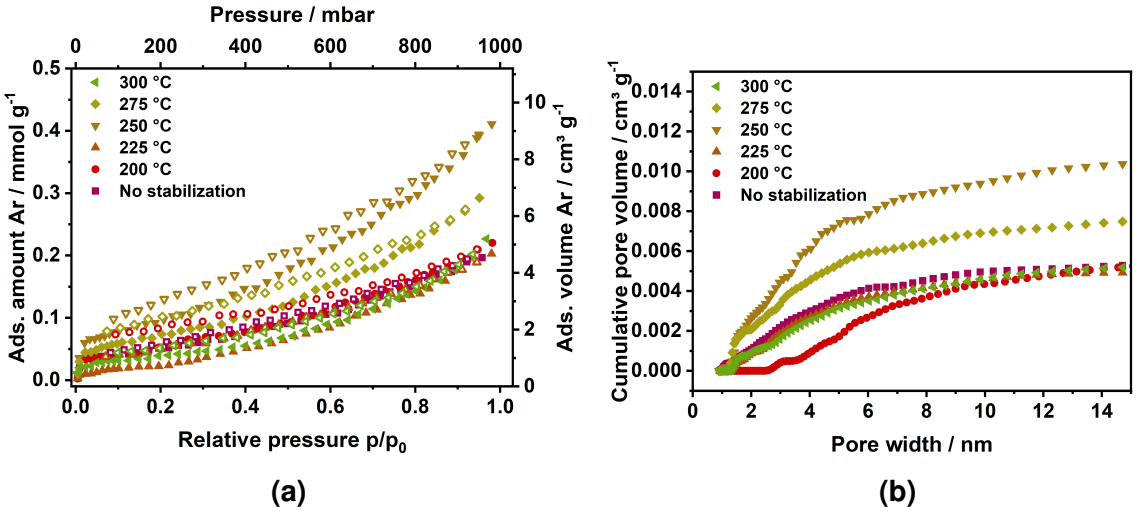


Figure 5.13. – (a) Ar adsorption isotherms measured at 87 K of carbon nanofibers stabilized at 200, 225, 250, 275 and 300 °C for 1 h in air and carbonized for 3 h in Ar at 800 °C. (b) Pore size distribution based on the isotherm data determined by QSDFT calculations using a kernel for carbon on slit pores.

Table 5.2. – BET area, ultramicropore volume (V_{Ultra}), supermicropore volume (V_{Super}), mesopore volume (V_{Meso}), DFT pore volume (V_{DFT}), Monte-Carlo pore volume (V_{MC}) and total pore volume (V_{Tot}) for carbon nanofibers stabilized at temperatures of 200, 225, 250, 275 and 300 °C for 1 h in air. Subsequently, carbonization was conducted for 3 h in Ar at 800 °C.

Temperature	BET Area	V_{DFT}	V_{MC}	V_{Ultra}	V_{Super}	V_{Meso}	V_{Tot}
°C	$m^2\,g^{-1}$	$cm^3\,g^{-1}$	$cm^3\,g^{-1}$	$cm^3\,g^{-1}$	$cm^3\,g^{-1}$	$cm^3\,g^{-1}$	$cm^3\,g^{-1}$
200	3.50	0.006	0.027	0.007	0.020	0.006	0.033
225	1.82	0.004	0.071	0.032	0.040	0.004	0.076
250	6.67	0.011	0.116	0.079	0.038	0.008	0.126
275	5.12	0.008	0.160	0.108	0.052	0.006	0.166
300	3.06	0.006	0.159	0.112	0.048	0.007	0.164

Since narrow micropores are inaccessible for Ar due to its critical diameter, CO_2 isotherms at 273 K were measured to assess the present micro- and ultramicropore volume (Figure 5.14a). An almost linear adsorption isotherm is obtained on the 200 °C sample with a low CO_2 uptake of 0.3 mmol g^{-1} at 1 bar. At higher stabilization temperatures the CO_2 capacity increases and the isotherm slope in the low-pressure region ($p/p_0 < 0.01$) increases distinctly. For samples stabilized at temperatures > 250 °C the isotherm turns into a type I shape, which is characteristic for highly microporous adsorbents. The CO_2 adsorption capacity at 1 bar rises to 2.7 mmol g^{-1} on these samples. The CO_2 adsorption isotherms were used to determine the pore size distribution based on Monte-Carlo calculations with a kernel for slit pores on carbon (Figure 5.14b).

The sample stabilized at 200 °C contains only pores larger than 0.6 nm and reaches a cumulative pore volume (V_{MC}) of 0.027 $cm^3\,g^{-1}$. These values are comparable to the

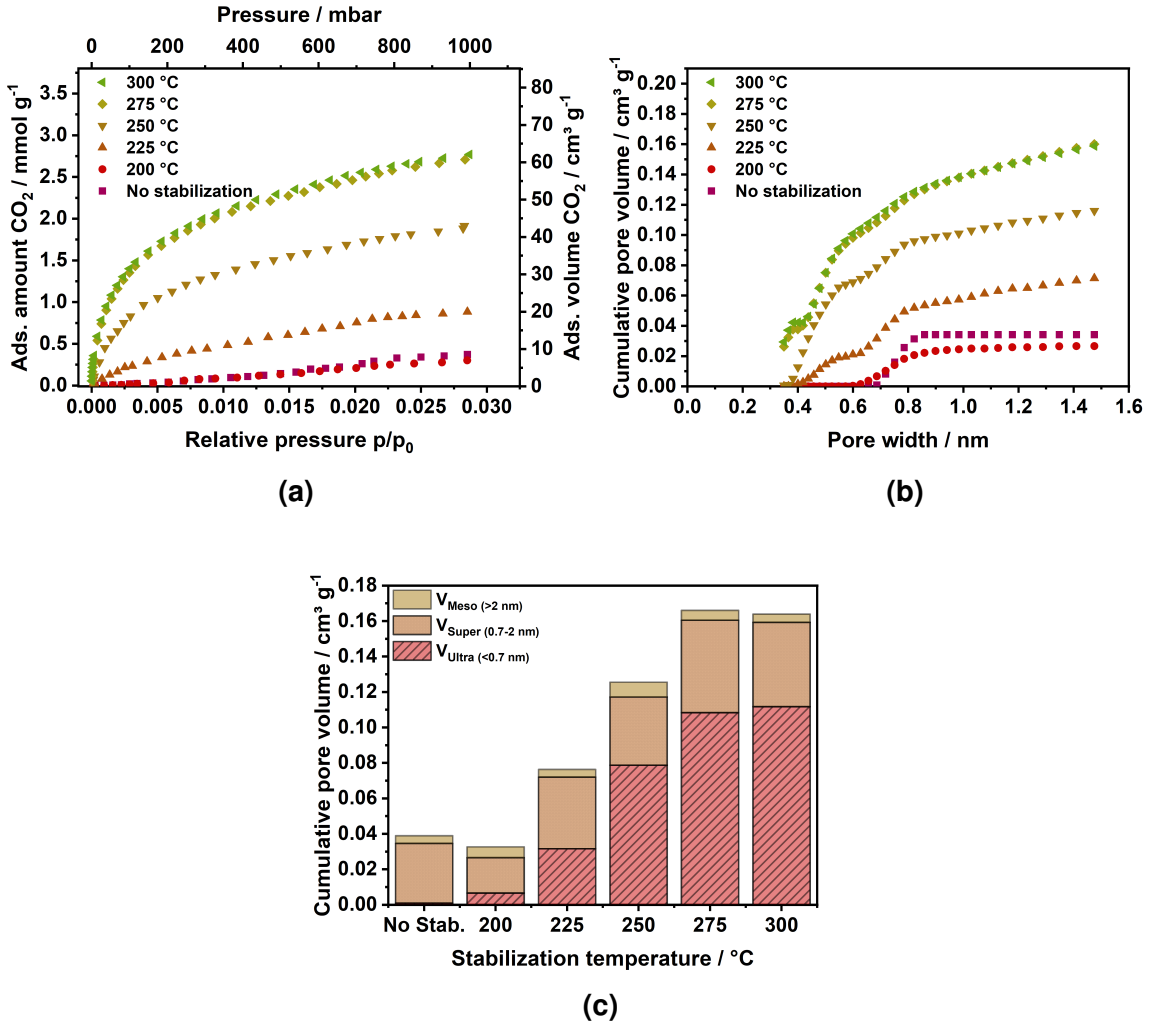


Figure 5.14. – (a) CO_2 isotherms on carbon nanofibers, which were stabilized at 200, 225, 250, 275 and 300 °C for 1 h in air. Afterwards the samples were carbonized for 3 h in Ar at 800 °C. The isotherms were measured at 273 K. (b) cumulative pore size distribution based on the CO_2 isotherms determined by Monte-Carlo calculations using a kernel for slit pores on carbon. (c) Pore size distribution divided into ultramicropore (V_{Ultra}), supermicropore (V_{Super}) and mesopore volume (V_{Meso}) based on DFT calculations using Ar isotherm data and Monte-Carlo calculations based on CO_2 isotherms.

pore volume of carbon nanofibers without thermal stabilization (Figure 5.14b, Table 5.2). At increasing stabilization temperature, V_{MC} rises steadily and results in a maximum of 0.16 $cm^3\ g^{-1}$ on samples stabilized at 275 and 300 °C. Within V_{MC}, a significant increase of the V_{Ultra} (< 0.7 nm) is observed. Especially this high formation of V_{Ultra} results in the distinct increase of the CO_2 adsorption capacities. The cumulative pore size distributions obtained from the Ar and CO_2 isotherms were combined to give a holistic overview on the pore size distribution of the samples (Figure 5.7c).

To do so, the gained data was separated into three pore regions: Ultramicropore volume V_{Ultra} (< 0.7 nm), supermicropore volume V_{Super} (0.7-2 nm) and mesopore volume V_{Meso}

(> 2 nm). V_{Super} consists of V_{MC} in the range of 0.7-1.5 nm and V_{DFT} in the range from 1.5-2 nm. The others are based solely on the respective applicable method.
The present V_{Ultra} rises from 0.007 $cm^3 g^{-1}$ (200 °C) to 0.112 $cm^3 g^{-1}$ (300 °C). Moreover, a rise of Vsuper from 0.034 $cm^3 g^{-1}$ to 0.048 $cm^3 g^{-1}$ is obtained, whereas V_{Meso} stays on a negligible level between 0.004 to 0.008 $cm^3 g^{-1}$. This clearly points out the distinct effect of stabilization temperature on the formation of the ultramicropore and supermicropore volume. Overall, the impact is comparable to the impact of the stabilization duration.

5.4. Impact of the stabilization atmosphere

All previously discussed results were obtained on carbon nanofibers, which were stabilized in air. However, thermal stabilization can in principle be conducted in inert gas, i.e. N_2, too. A negative impact of N_2 as stabilization atmosphere was reported regarding the mechanical properties of carbon nanofibers [125]. However, no results are available on the impact of the stabilization atmosphere (N_2 and air) on the pore structure and the gas adsorption properties. Therefore, the impact of the stabilization atmosphere is investigated in the following chapter.

5.4.1. Characterization

As described in Figure 2.4 the stabilization in N_2 inhibits oxidation reactions of the stabilized ladder polymer. The absence of oxygen-containing surface functional groups alters the chemical reactions during the carbonization step, which potentially affects the pore structure.

Simultaneous TGA-DSC measurements

Simultaneous TGA-DSC measurements were conducted to identify differences in the reaction pathways of the stabilization in air and in N_2. In both atmospheric conditions the PAN-based nanofibers were heated from 40-450 °C at a heating rate of 5 K min^{-1}. The mass changes and the heat flows are depicted in Figure 5.15. At low temperatures, the mass loss of the nanofibers in both atmospheres is very similar, showing a minor step at 100 °C, which is assigned to evaporation of adsorbed water. At 260 °C a distinct mass loss from 98 wt.-% to 77 wt.-% occurs on nanofibers stabilized in N_2. Afterwards

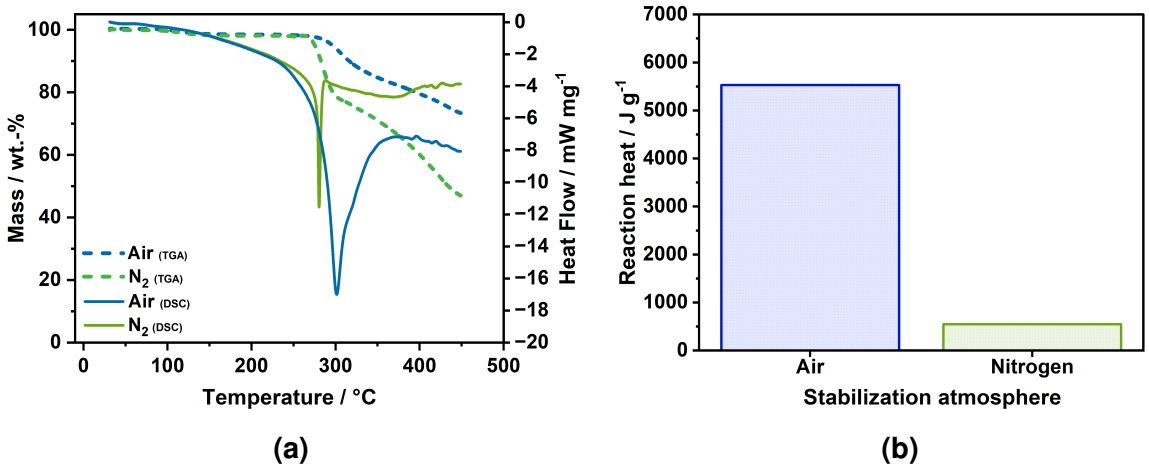


Figure 5.15. – (a) Simultaneous TGA-DSC of the thermal stabilization of PAN-based nanofibers in air and in N_2. The samples were heat treated at 10 K min^{-1} from room temperature up to 450 °C. (b) Emitted reaction heats in J g^{-1} determined by integration of the exothermic peaks.

the slope attenuates, but the mass loss continues to 47 wt.-% at 450 °C. In contrast, nanofibers stabilized in air show a far less pronounced mass loss starting at 260 °C and resulting in a mass of 73 wt.-% at 450 °C. The lower mass loss during thermal stabilization in air can be assigned to the incorporation of oxygen into the stabilized ladder polymer, which is absent for the stabilization in N_2 resulting in a higher mass loss.

Both mass losses are accompanied by the release of high reaction heats. A sharp, narrow exotherm DSC peak is visible at 280 °C for the stabilization in N_2, whereas a broad undefined exothermic peak at 301 °C is obtained for the stabilization in air.

The narrow sharp signal is commonly assigned to the cyclization reactions in the absence of oxidation reactions. Contrary, the stabilization in air is visible as a broad peak due to the different oxidation reactions, which occur in parallel and consecutive to the cyclization reactions [137–139]. These results clearly prove different reaction pathways for both stabilization processes.

IR Spectroscopy and Elemental Analysis

To determine differences in the elemental composition and the chemical structure of the nanofibers after the stabilization in air or N_2, IR spectroscopy and elemental analysis were conducted. Additionally, H_2O isotherm measurements were performed to determine changes in the hydrophilicity of the adsorbents.

In Figure 5.16a the normalized IR spectra of PAN-based nanofibers, which were stabilized in air or N_2 at 250 °C for 15 h are compared. On first glance, both spectra look quite similar, exhibiting the characteristic absorption bands of the stabilized ladder polymer, like a strong $\nu_{C=C/C=N}$ absorption band at 1590 cm^{-1} and δ_{oop} vibrations of the aromatic-H atoms at 801 cm^{-1}. However, at a closer look, differences in the spectra are observed. In the spectrum of the nanofibers stabilized in N_2 the absence of the carbonyl shoulder at 1714 cm^{-1} is visible, which is an indication for the absence of surface oxygen-containing functional groups, i.e. carbonyl groups. Additionally, a sharp

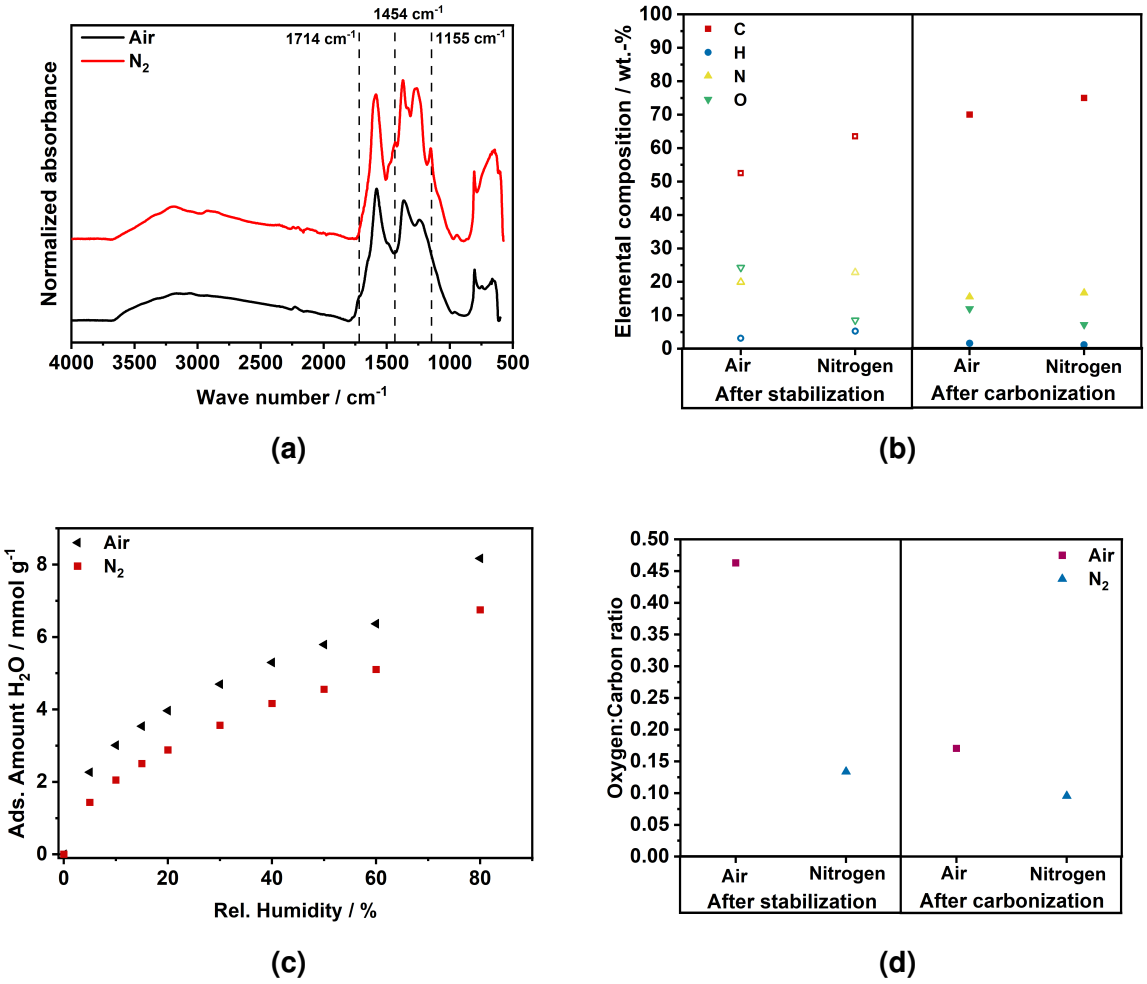


Figure 5.16. – (a) IR spectra of stabilized PAN-based nanofibers treated in air, respectively N_2 for 15 h at 250 °C. (b) Elemental analysis of the two samples after stabilization and after carbonization. The carbonization was conducted at 800 °C for 3 h in Ar for both samples. (c) H_2O isotherms at 298 K on nanofibers stabilized in air or N_2. (d) Oxygen:Carbon ratio of carbon nanofibers stabilized in air and N_2 after stabilization and after carbonization

peak at 1155 cm^{-1} occurs. Considering the spectrum of the nanofibers stabilized in air, the fact that it this absorption band is so prominent may be favoured by the absence of

other absorption bands in its vicinity. Typically, valence vibrations of alcohols are visible in this region. Thus, it could be an additional indication for the absence of oxygen in the structure. Nonetheless, as a variety of absorption bands is present in this region of the IR spectrum, a clear assignment to a certain vibration can not be drawn.

Besides indications for the absence of oxygen, the spectrum of the nanofibers stabilized in N_2 shows even after stabilization a quite pronounced absorption band at 1454 cm^{-1}. This correlates well to the determined cyclization index of 78 %, which is significantly lower than 92 % determined after the stabilization in air.

Despite, the assumption of no oxygen incorporation during N_2 stabilization and thus no oxygen-containing surface functional groups, the spectrum of nanofibers stabilized in N_2 shows a broad absorption band between 3700-2200 cm^{-1}, which was previously assigned to water adsorption due to a high number of oxygen functional groups and thus higher hydrophilicity (Figure 5.2.1).

Thus, H_2O isotherms were measured to assess the hydrophilicity of the stabilized nanofibers. The H_2O adsorption capacities were at 5.5 mmol g^{-1} at 80 % relative humidity, which is lower than the 8.0 mmol g^{-1} determined on nanofibers stabilized in air. However, the adsorption capacity is still remarkably high compared to nanofibers stabilized in air for durations smaller than 4 h (Figure 5.2.1).

Potentially, the comparably high water adsorption could be explained by a different structure of the stabilized ladder polymer containing amine functional groups. Liu et al. identified the interconnection of aminopyridine rings as major reaction during stabilization in N_2 [140–142]. The presence of such primary amines could allow hydrogen bonding similar to these of hydroxyl groups. Nonetheless, further experiments are required to verify this explanation and understand the surprisingly high water adsorption on nanofibers stabilized in N_2.

The discussed inhibition of oxygen incorporation during the thermal stabilization in N_2 is confirmed by results of the elemental analysis (Figure 5.16b). PAN-based nanofibers stabilized in N_2 show an oxygen fraction of 8.5 wt.-%, which is a trifold reduction compared to 23.8 wt.-% for the sample stabilized in air. The remaining 8.5 wt.-% can probably be assigned to impurities or copolymer contents of the PAN precursor, which are common in industrial PAN grades. The significant difference in the oxygen content is clearly visible in the drop of the oxygen:carbon ratio from 0.46 to 0.13 for the stabilization in N_2 (Figure 5.16c).

After carbonization the oxygen fractions are at 11.9 wt.% and 7.1 wt.-%, which is a far less pronounced difference compared to after stabilization. This is well reflected in

the oxygen:carbon ratio, which is at 0.17 for samples stabilized in air and at 0.10 for nanofibers stabilized in N_2 after carbonization. The strong reduction of the oxygen fraction of the nanofibers stabilized in air, fits well to the proposed condensation crosslinks during carbonization (Figure 2.6) [75].

Raman Spectroscopy

Following the previous interpretation, the lower oxygen incorporation into the nanofibers stabilized in N_2 and thus a lower number of condensation crosslinking reactions during carbonization would result in smaller carbon frameworks. This could result in a lower structural order of the carbon nanofibers. To assess the structural order of the carbon nanofibers, Raman measurements are conducted and the D_1/G ratio as measure of the structural order is determined (Figure 5.17). A D_1/G ratio of 1.74 was determined for

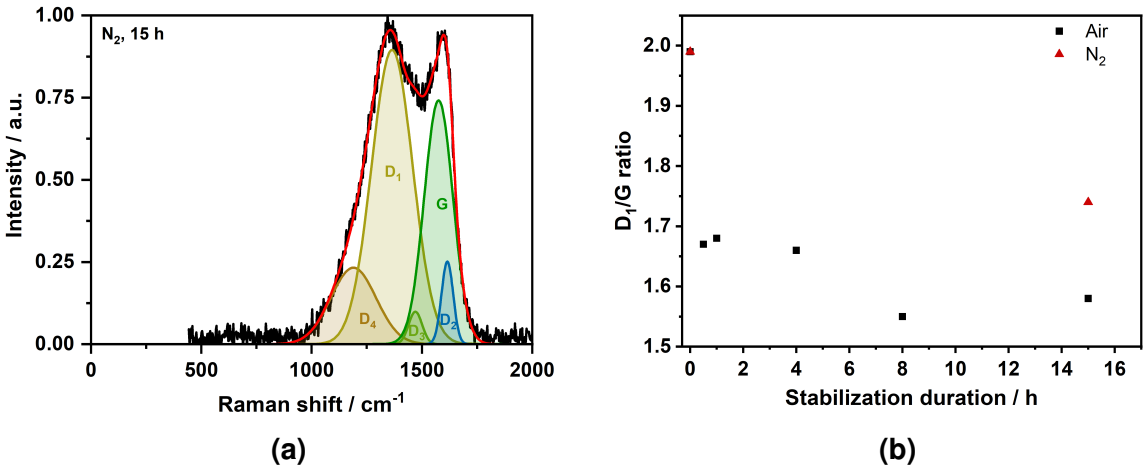


Figure 5.17. – (a) Raman spectrum of carbon nanofibers stabilized for 15 h in N_2 at 250 °C. After stabilization the samples were carbonized at 800 °C. The D and G band were fitted by 5 Gaussian fits, D_1, D_2, D_3, D_4 and G. (b) D_1/G ratio for the carbon nanofibers stabilized in N_2 compared to samples stabilized in air at durations from 0-15 h.

the carbon nanofibers stabilized in N_2. This is a 10 % increase compared to the D_1/G ratio of the samples stabilized in air, which was at 1.58. An increase in the D_1/G ratio reflects a decrease of the structural order of the carbon material. This matches well to the expectations of a reduced structural order due to a lower number of condensation reactions and thus smaller carbon frameworks.

5.4.2. Impact on the pore structure

Finally, the impact of the structural and chemical differences of the carbon nanofibers, stabilized in air or N_2, on the pore structure is discussed. Ar and CO_2 isotherm measurements were performed and used for pore size analysis.
The Ar isotherms showed type II isotherm shapes, which are typical for non-porous or macroporous adsorbents (Figure 5.18a). The adsorbed capacities are low and reach maximum values of 0.2 to 0.4 mmol g^{-1} at 1 bar. Carbon nanofibers stabilized in N_2 show slightly lower adsorption capacities. However, these differences are negligible. The pore size distribution, calculated by QSDFT calculations, fits to the isotherm shapes and negligible pore volumes are present independent of the atmospheric conditions (Figure 5.18b). These low pore volumes result in low BET areas, which are at 4.7 and 5.9 m^2 g^{-1} (Table 5.3).

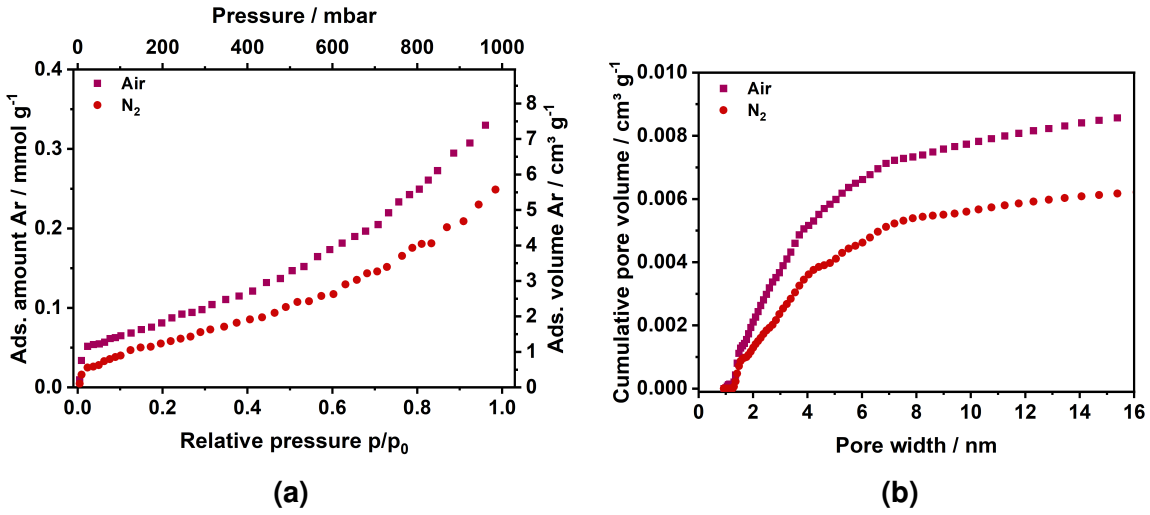


Figure 5.18. – (a) Ar isotherms measured at 87 K and (b) cumulative pore size distribution based on QSDFT calculations using a kernel for slit pores on carbon. All measurements are conducted on carbon nanofibers carbonized at 800 °C for 3 h in Ar. Prior stabilization was conducted for 15 h at 250 °C either in air or N_2.

As Ar isotherms can not be used for analysis of the narrow micropore volume due to size exclusion effects, CO_2 isotherm measurements were conducted. The CO_2 adsorption isotherms for carbon nanofibers stabilized at 250 °C for 15 h in air and N_2 are depicted in Figure 5.19a. For carbon nanofibers stabilized in air a type-I shaped isotherm with a capacity of 2.7 mmol g^{-1} at 1 bar is determined (Refer to section 5.2). In contrast, the carbon nanofibers stabilized in N_2 show an almost linear CO_2 isotherm and low adsorption capacities of 0.65 mmol g^{-1} at 1 bar.
The isotherms were used for calculation of the pore size distribution based on Monte-Carlo calculations using a model for slit pores on carbon (Figure 5.19b). Carbon

Table 5.3. – BET area, cumulative pore volume based on QSDFT calculations (V_{DFT}), cumulative pore volume based on Monte-Carlo calculations (V_{MC}), ultramicropore volume (V_{Ultra}), supermicropore volume (V_{Super}), mesopore volume (V_{Meso}) and total pore volume (V_{Tot}) for carbon nanofibers stabilized at 250 °C for 15 h in air and N_2. Subsequently, carbonization was conducted for 3 h in Ar at 800 °C.

Temperature	BET Area	V_{DFT}	V_{MC}	V_{Ultra}	V_{Super}	V_{Meso}	V_{Tot}
°C	$m^2\,g^{-1}$	$cm^3\,g^{-1}$	$cm^3\,g^{-1}$	$cm^3\,g^{-1}$	$cm^3\,g^{-1}$	$cm^3\,g^{-1}$	$cm^3\,g^{-1}$
Air	5.9	0.009	0.164	0.110	0.055	0.007	0.171
N_2	4.7	0.006	0.052	0.018	0.036	0.005	0.059

nanofibers stabilized in air show a total cumulative pore volume of 0.164 $cm^3\,g^{-1}$ at 1.5 nm. The majority of pores present is below 1 nm ranging down to less than 0.4 nm. In contrast, for carbon nanofibers stabilized in N_2 a total cumulative pore volume of 0.089 $cm^3\,g^{-1}$ was determined. Moreover, a negligible pore volume below 0.6 nm is present on the carbon nanofibers. Between 0.6 and 1 nm a sharp rise of the cumulative pore volume is observed. Afterwards only a minor amount of pore volume is present.
To give a holistic view on the pore size distribution of the carbon nanofibers, Monte-Carlo and QSDFT calculations were combined (Figure 5.19c). A significant decrease in pore volume of almost 50 % is observed for carbon nanofibers stabilized in N_2. This reduction is mainly assigned to the absence of V_{Ultra} on these samples, which reduces from 0.110 to 0.017 $cm^3\,g^{-1}$. In the meantime, V_{Super} and V_{Meso} show only minor changes depending on the applied stabilization conditions.
Overall, the results reveal a significant impact of the stabilization atmosphere on the pore structure of the carbon nanofibers. Especially, the formation of V_{Ultra} is essentially affected and the stabilization in air was found as beneficial for the formation of a high V_{Ultra}.

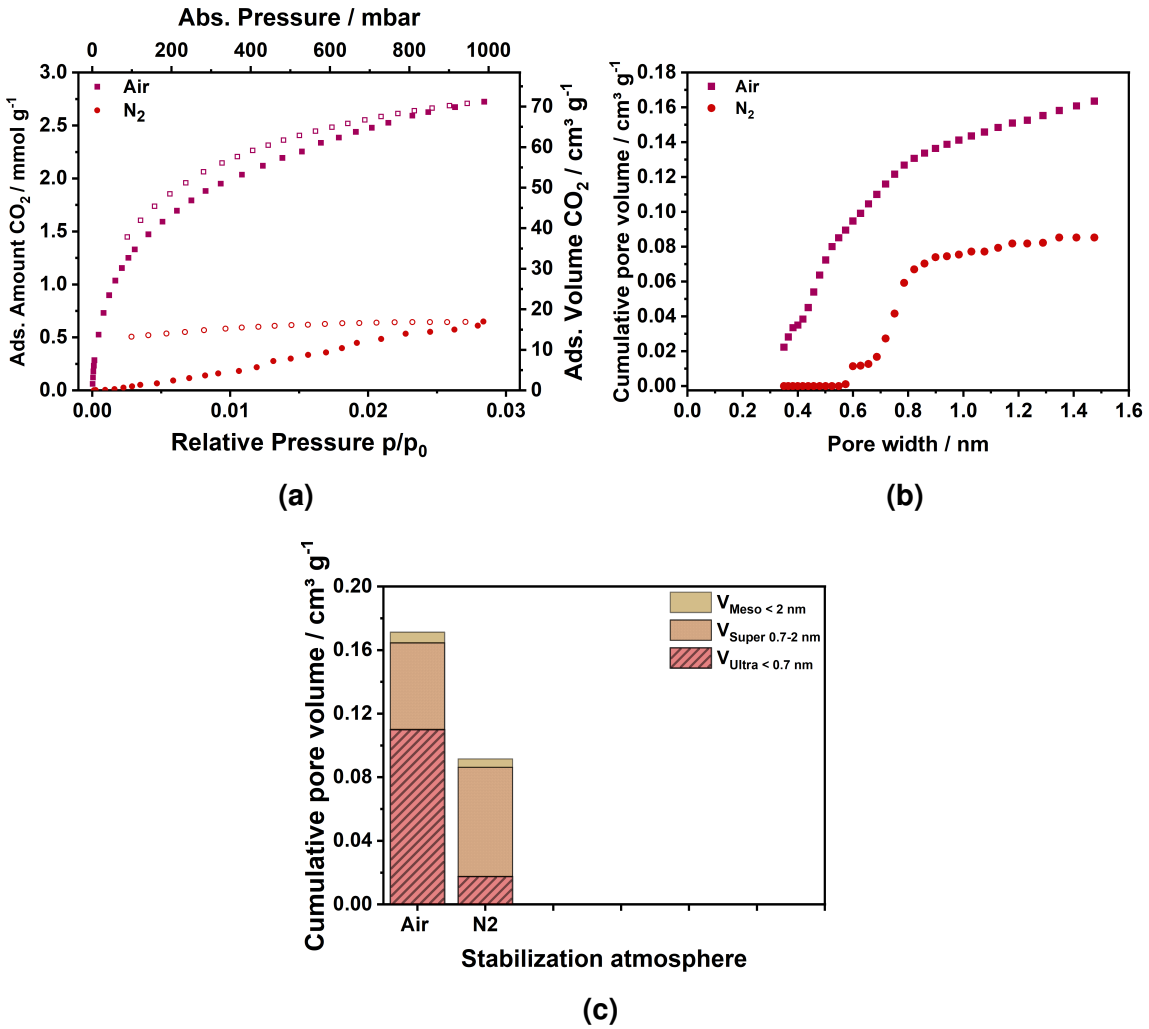


Figure 5.19. – (a) CO_2 adsorption isotherms measured at 273 K for carbon nanofibers stabilized for 15 h in air or nitrogen at 250 °C. (b) Cumulative pore volume based on Monte-Carlo calculations using a kernel for slit pores on carbon and (c) combined cumulative pore volume divided into V_{Ultra}, V_{Super}, and V_{Meso}. The data is combined using QSDFT calculations based on Ar isotherms at 87 K and Monte-Carlo simulation based on the CO_2 isotherms at 273 K.

5.5. Correlations between stabilization and pore structure

The previously discussed results showed significant impacts of the stabilization conditions on the stabilization progress. Additionally, gas adsorption measurements on carbonized samples revealed distinct effects on the pore formation and the adsorption capacities. This section targets on correlating both results.

In Figure 5.20a, the correlation of the oxygen content to the cyclization index is depicted. Both increase at more intense stabilization treatment (higher temperature, longer duration) as the reactions are promoted by the supplied additional energy. Since both, the oxygen content and the cyclization index, are strongly influenced by the intensity of

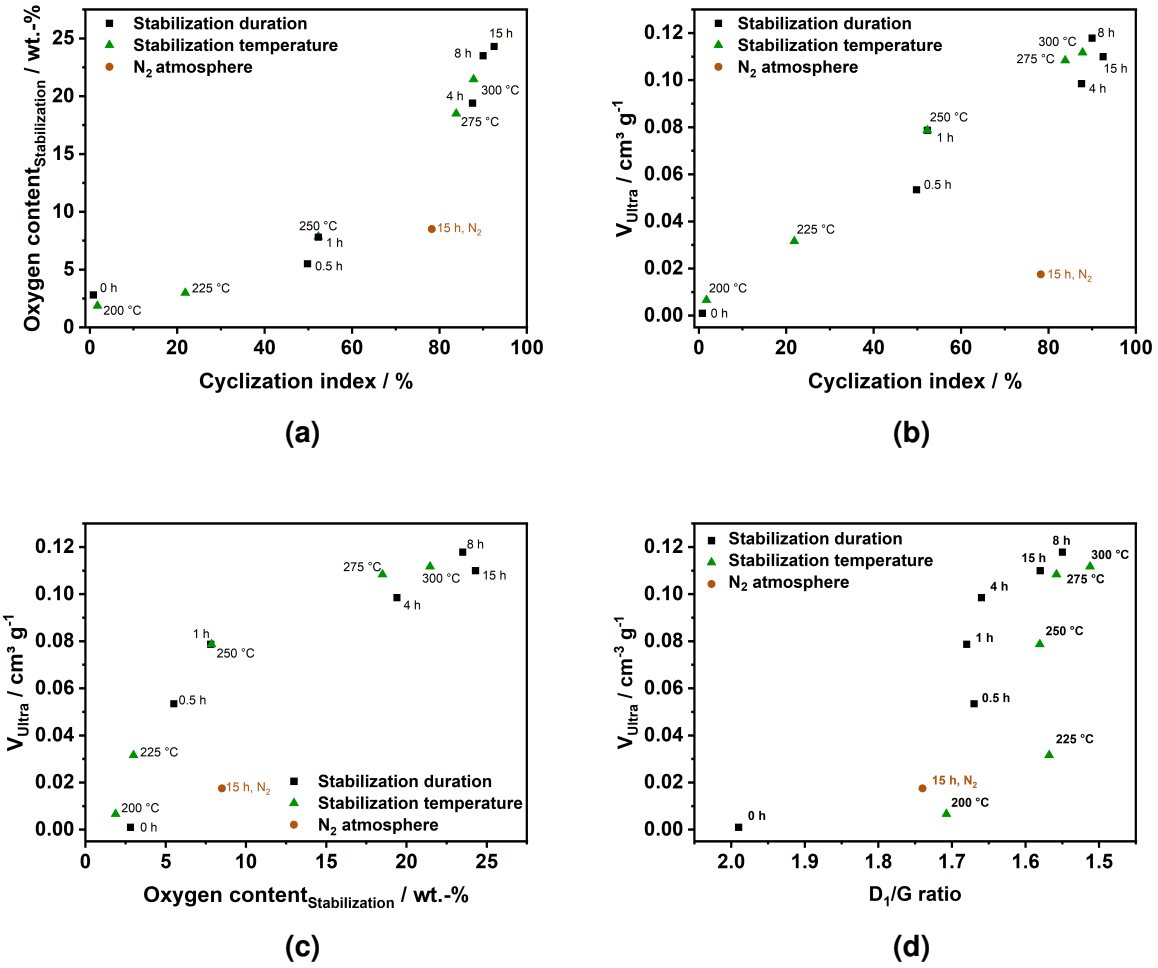


Figure 5.20. – Correlation of a) the oxygen content and cyclization index determined after thermal stabilization, b) V_{Ultra} to the cyclization index, c) V_{Ultra} to the oxygen content after stabilization and d) V_{Ultra} to the D_1/G ratio. V_{Ultra} was determined after carbonization. The samples were synthesized at different stabilization duration from 0-15 h at 250 °C and at different temperatures from 200 to 300 °C for 1 h. All stabilization were conducted in air. Additionally, one stabilization was conducted at 15 h in N_2 atmosphere. All carbonizations were conducted at 800 °C in Ar for 3 h.

stabilization conditions, a causal relationship is rather unlikely. Nonetheless, the good agreement between the duration and temperature series confirms the similar impact of duration and temperature variation on the stabilization process.

Furthermore, a good correlation of V_{Ultra} to the increasing cyclization index was found (Figure 5.20b). At higher cyclization indices, V_{Ultra} of the carbonized nanofibers increases steadily. The variation of stabilization duration and temperature have very similar effects. The sample stabilized in N_2 deviates significantly from the good correlation observed for temperature and duration. This could indicate that the degree of cyclization is not the main factor influencing pore formation, which matches to the discussed results in section 5.4.

Moreover, good correlations of V_{Ultra} to the oxygen content after stabilization were obtained (Figure 5.20c). A steep increase of V_{Ultra} is visible for low oxygen contents, which approaches a limiting value for oxygen contents of 20-25 wt.-%. Carbon nanofibers stabilized in N_2 show reduced V_{Ultra} compared to the carbon nanofibers at identical conditions in air, which is attributed to the absence of the oxygenated structures after thermal stabilization and thus reduced ultramicropore formation during carbonization.
The correlations of V_{Ultra} to the cyclization index and oxygen content, show plausible causal relationships, since the formation of V_{Ultra} occurs during carbonization, whereas oxygen incorporation and cyclization take place during stabilization. Thus, V_{Ultra} formation and oxygen incorporation and cyclization cannot be affected by identical parameters. The correlations of V_{Ultra} to the oxygen content and the cyclization index show that the increase of V_{Ultra} during carbonization is likely to be dependent on these parameters.
Besides oxygen content and cylization index, the structural order of the carbon nanofibers after carbonization might affect the formation of V_{Ultra}. However, correlations of V_{Ultra} to the D_1/G ratio do not show a unambiguous correlation of these two parameters (Figure 5.20d). Thus, a causal relationship is rather unlikely.
In total, the discussed correlations imply that V_{Ultra} formation during carbonization depends on the oxygen incorporation and partially on the cyclization progress during stabilization. Nonetheless, it is conceivable that V_{Ultra} is affected by additional parameters, which were not considered here.
All in all, the results clearly point out, that thermal stabilization conditions need careful consideration for tailoring the pore volume of PAN-based carbon nanofibers.

6. Control of oxygen-flow during post-treatment of KOH-activated carbon nanofibers

6.1. Preface

Main parts of the results presented in this chapter have been previously published in RSC Advances under a CC BY 3.0 license [88]. Minor modifications were made to adjust the publication to the context of this thesis and an additional discussion was added in section 6.6. The material synthesis, TGA-DSC studies and gas adsorption measurements were conducted by Tom Fischer. Elemental analysis and ICP-OES measurements were performed by the Central Institute of Analytics at Forschungszentrum Jülich GmbH. The Raman measurements were conducted and evaluated by Sven Jovanovic.

6.2. Oxygen flow conditions during post-treatment

After thermal stabilization the nanofibers are commonly carbonized. After or simultaneously to the carbonization, KOH activation is a frequently applied method to introduce additional pore volume into the carbon nanofibers. KOH activation proceeds via several consecutive and parallel reactions, which were discussed in subsection 2.3.4. At elevated temperatures the formation of metallic potassium is proposed [77, 78, 83]. Such metallic potassium products are highly sensitive to air and would react vigorously to corresponding per- and superoxides [143, 144].

$$2\,\mathrm{K} + 0.5\,\mathrm{O_2} \longleftrightarrow \mathrm{K_2O}, \quad \Delta \mathrm{H_R} = -363\ \mathrm{kJ\,mol^{-1}} \tag{6.1}$$

$$2\,\mathrm{K} + \mathrm{O_2} \longleftrightarrow \mathrm{K_2O_2}, \quad \Delta \mathrm{H_R} = -496\ \mathrm{kJ\,mol^{-1}} \tag{6.2}$$

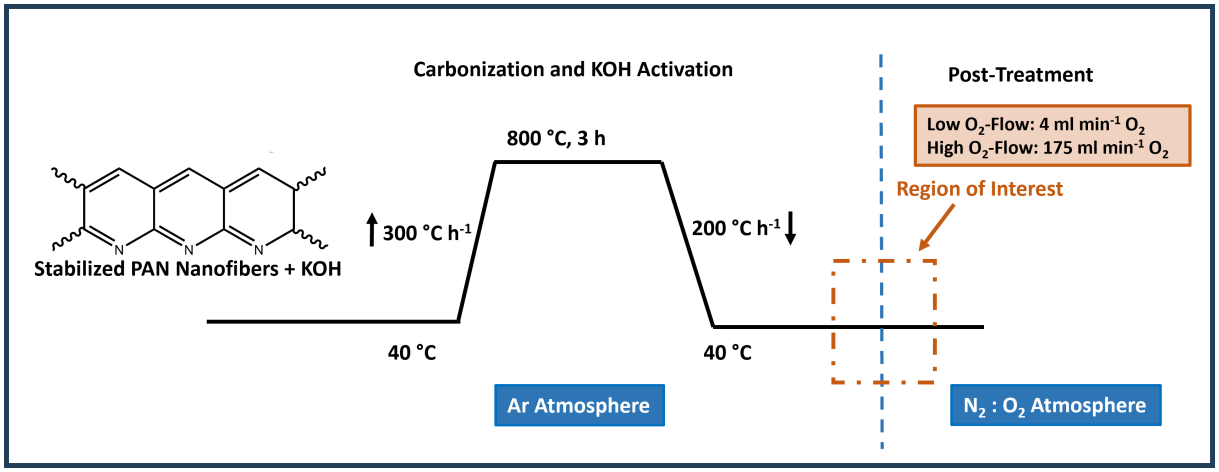


Figure 6.1. – Scheme of the applied heat treatment for carbonization of the PAN-based nanofibers. After cool down the KOH activated carbon nanofibers are exposed to different post-treatment conditions, which are detailed investigated regarding their effects on the gas adsorption properties.

$$\mathrm{K} + \mathrm{O_2} \longleftrightarrow \mathrm{KO_2}, \quad \Delta \mathrm{H_R} = -285\ \mathrm{kJ\,mol^{-1}} \tag{6.3}$$

The occurrence of these strongly exothermic potassium oxidation reactions was already observed in 1926 by Fredenhagen and Cadenbach for potassium intercalated graphite [145, 146]. Additionally, Kapetjin et al. made similar observations during K_2CO_3 activation of coals [147]. Interestingly, although KOH activation is widely applied since decades on a large variety of materials [90] such vigorous potassium oxidation reactions are not described for KOH activation although metallic potassium is proposed to be formed.

Therefore, experiments on the post-treatment conditions after the KOH activation of carbon nanofibers were conducted. The term 'post-treatment' refers to the applied atmospheric conditions after the cool down of the sample to room temperature subsequent to KOH activation (Figure 6.1).

In preliminary experiments KOH-activated carbon nanofibers were post-treated at ambient air, which is the commonly applied process [77, 78, 83]. At the exposure to ambient air, a strong red glowing of the carbon nanofibers was observed, indicating vigorous potassium oxidation reactions. Such a severe combustion reaction is believed to significantly alter the carbon nanofiber structure. Therefore, two post-treatment conditions, 'Low O_2-flow' and 'High O_2-flow' were applied in this chapter, to investigate the impact of the potassium oxidation reactions and to develop a strategy to avoid structural changes of the carbon nanofibers. The occuring reactions as well as the morphological changes were thoroughly investigated using SEM, TGA-DSC, TGA-MS, CHNO elemental analysis, Raman spectroscopy and gas adsorption measurements.

6.3. High O_2-flow treatment

In Figure 6.2a the TGA results of a freshly KOH-activated sample on switching the atmosphere from Ar to a mixture of N_2:O_2 (30:70), high O_2-flow conditions, are shown. The vertical dashed line indicates the switch from Argon to N_2:O_2 (30:70) atmosphere. The oxygen flow rate was set to 175 mL min^{-1} O_2-flow. Almost instantly after the switch of atmosphere, a mass gain of 2.8±0.7 wt.-% is observed. Afterwards, a mass loss of 3.1±1.1 wt.-% occurs before the mass slightly increases. Simultaneously, the temperature rises to 130 °C and cools down again to the temperature setpoint of 40 °C afterwards. However, it must be emphasized, that this is only an apparent temperature, as the reaction heat is partially consumed by the heat capacity of comparatively large TGA crucible. The actual temperature of the sample during the reaction is significantly higher.

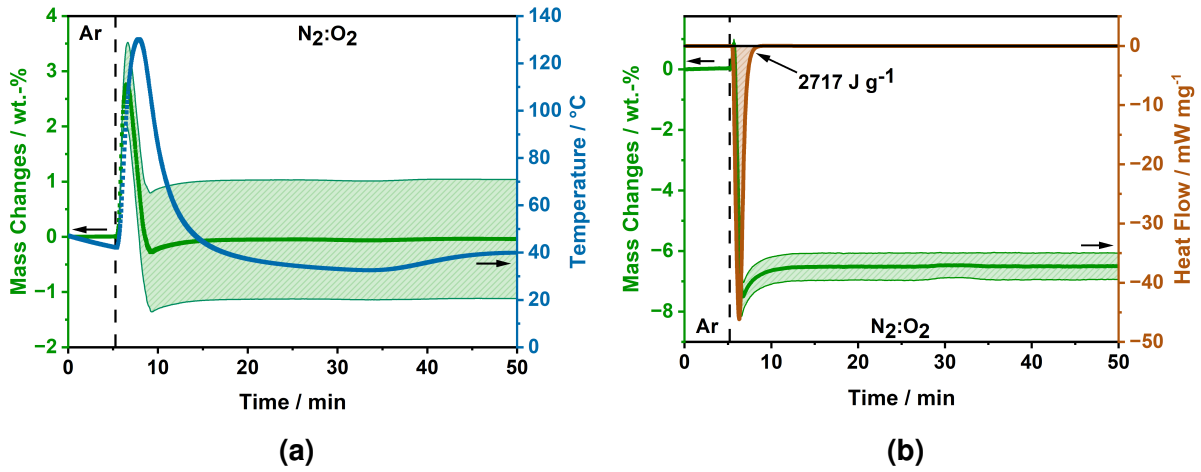


Figure 6.2. – (a) Mass and temperature changes of a carbon nanofiber sample during post-treatment at high-O_2-flow conditions. (b) Emitted reaction heat of the occuring chemical reactions obtained in a separate DSC measurement.

The mass gain and the temperature rise can be assigned to the oxidation reactions of elemental potassium, which was formed during the KOH activation reactions (Equation 2.6 and Equation 2.7). The formation of K_2O (Equation 6.1), K_2O_2 (Equation 6.2) and KO_2 (Equation 6.3) releases high reaction enthalpies. The oxidation reactions most probably result in the formation of KO_2 for conditions with a high availability of oxygen, due to the higher lattice stability of KO_2 compared to K_2O and K_2O_2 [144]. The mass gain of 2.8±0.7 wt.-% corresponds to the O_2 uptake of 0.87 mmol g^{-1}, which would require a potassium amount of 0.87 mmol g^{-1} according to Equation 6.3. This corresponds to 14 % of the total potassium, present at the carbon nanofiber samples, which was deter-

mined via ICP-OES (see section A.1). The calculated reaction heat of the formation of 0.87 mmol g^{-1} KO_2 is –248 J g^{-1} according to Equation 6.3, which is sufficient to cause a significant temperature rise.

However, these reactions cannot explain the subsequent mass loss of 3.1±1.1 wt.-%. An analysis of the gaseous products determined CO_2 as main emission, indicating a partial carbon combustion reaction caused by the reaction heat of the potassium oxidation. A total carbon loss of 2.62 mmol g^{-1} is calculated via Equation 6.4 accompanied by -1020 J g^{-1} reaction heat. In total, potassium oxidation and carbon combustion reactions result in an emitted reaction heat of -1268 J g^{-1}.

$$\mathrm{C} + \mathrm{O_2} \longleftrightarrow \mathrm{CO_2}, \quad \Delta H_R = -393\,kJ\,mol^{-1} \tag{6.4}$$

Comparing the calculated reaction heats of KO_2 and CO_2 formation, the emitted reaction heat is caused to almost 80 % by the carbon combustion to CO_2. According to the basic heat equation of thermodynamics, the emitted heat could cause a temperature increase to a temperature higher than 700 °C, which could explain the observed red glowing of the carbon nanofibers.

Based on the calculated carbon loss the theoretical released amount of CO_2 would be 2.58 mmol g^{-1}, which equals a CO_2 release of 114 mg g^{-1}. The amount of CO_2 determined via quantification of the gaseous products is lower, giving a value of 40.5 mg g^{-1}. The significant difference could be explained by the emission of solid particles due to the vigorous reaction, which are not detected by the MS. Additionally, side reactions due to formed KO_2 are possible during the reaction as listed in Equation 6.5 and Equation 6.6. The possible side reactions mainly result in the formation of potassium carbonate and bicarbonate [148, 149].

$$2\,\mathrm{KO_2} + \mathrm{CO_2} \longleftrightarrow \mathrm{K_2CO_3} + 1.5\,\mathrm{O_2}, \quad \Delta H_R = -186\,kJ\,mol^{-1} \tag{6.5}$$

$$2\,\mathrm{KO_2} + \mathrm{H_2O} + 2\,\mathrm{CO_2} \longleftrightarrow 2\,\mathrm{KHCO_3} + 1.5\,\mathrm{O_2}, \quad \Delta H_R = -328\,kJ\,mol^{-1} \tag{6.6}$$

Furthermore, simultaneous TGA-DSC measurements were conducted to obtain experimental data on the emitted reaction heats for High O_2-Flow (Figure 6.2b). The simultaneous TG measurement was done to assess the comparability of the TGA measurements since different sized crucibles had to be used for both measurements.

An emitted reaction heat of -2717 J g^{-1} was determined for the post-treatment step at high O_2-flow (Figure 6.2b). This value is about twice as high as the calculated reaction

heat of -1268 $J\,g^{-1}$ from previous TG measurements (Figure 6.2a). The deviation of these two methods is explicable, when considering the shape of the TG signal of the DSC measurement. Similar to the first discussed TG signal, a mass gain is observed directly after the switch to the High O_2-flow. Subsequently, a significant mass loss due to carbon combustion occurs. However, the mass loss during the DSC measurement is 8.2 wt.-%, which is more than double the value of 3.1 wt.-% during the TG measurement. Due to the increased carbon combustion during the DSC measurement the experimental value and the calculated reaction enthalpy from the TG measurement may not be directly comparable. The increased carbon combustion is probably caused by denser packed carbon nanofibers in the smaller DSC crucible, resulting in a stronger heat accumulation. This is an important hint, as the extent of potassium oxidation and carbon combustion reactions depend on the packing density and, therefore, heat and oxygen transport properties of the material.
Interestingly, similar observations are not described for KOH activation of commonly used carbon precursors, e.g. PAN powder, carbon fibers [89, 116, 150], biomass [52, 151, 152] and coals [153–155]. Although, the occurrence of these potassium oxidation reactions could be expected based on the proposed mechanisms for KOH activation mentioned in Equation 2.6 and Equation 2.7. Therefore, PAN powder was used as reference material and activated using the identical conditions as for activation of the nanofiber material. During high O_2-flow post-treatment no pyrophoric effect was observed. Hence, the described pyrophoric effect is probably linked to the material structure induced by the electrospinning process and, possibly, the activation conditions. A more detailed study on the potassium oxidation induced carbon combustion reaction on reference carbon materials is discussed in section 6.6.
Overall, the post-treatment at high O_2-flow conditions results in the uncontrolled oxidation of metallic potassium to KO_2 causing a carbon combustion under severe formation of heat and a strong glowing of the carbon nanofibers.

6.4. Low O_2-flow treatment

To develop a treatment strategy to suppress the sample glowing, similar experiments were conducted using an O_2-flow of 4 $mL\,min^{-1}$, 'low O_2-flow'. Figure 6.3a shows the mass and temperature changes after the switch of atmosphere from Ar to a mixture of N_2:O_2 (80:20) with an O_2-flow rate of 4 $mL\,min^{-1}$ indicated by the dashed line.

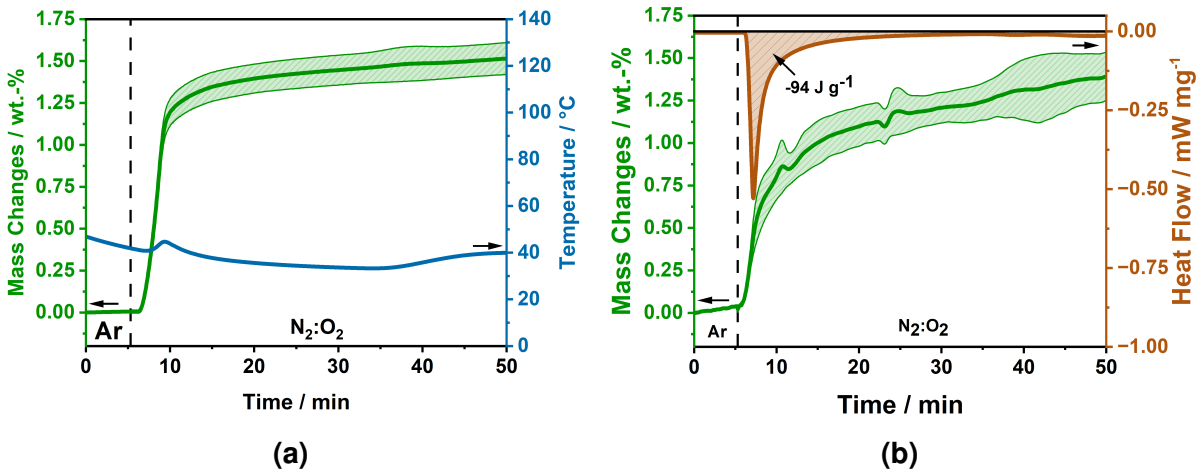


Figure 6.3. – (a) Mass change of the carbon nanofiber sample treated at low O_2-flow conditions as post treatment. (b) Evolved reaction heat during the post-treatment at low O_2-flow conditions determined by simultaneous TGA-DSC measurements.

A mass gain of 1.5±0.1 wt.-% accompanied by a minor temperature rise to 45 °C after 8 minutes is observed after the atmosphere switch. Contrary to the high O_2-flow, no weight loss is observed. The mass gain can be explained by the uptake of O_2 due to the oxidation of metallic potassium according to Equation 6.3. As the temperature increase is insufficient to cause a carbon combustion, no mass loss is observed. The obtained mass gain equals an O_2 uptake of 0.44 mmol g^{-1}, based on Equation 6.3 this results in the emission of -128 J g^{-1} reaction heat. This calculated reaction heat is comparable to the experimental value of -94 J g^{-1} obtained from the simultaneous TGA-DSC measurements (Figure 6.3b) and causes a slight temperature rise on the carbon nanofibers. The slight deviation of the obtained reaction heats can be explained by the simple nature of the calculations used, which only considered one potassium formation reaction neglecting possible side reactions to the formation of other potassium oxide species [143, 144, 148]. Summarizing, the low O_2-flow post-treatment results in controlled oxidation reactions during exposure to oxygen. The emitted reaction heat of -94 J g^{-1} is significantly reduced compared to -2717 J g^{-1} for high O_2-flow. Therefore, no indication for a carbon combustion was found.

6.5. Comparison of high O_2-flow and low O_2-flow

Besides the previously discussed mass and temperature changes during the sample treatment with high O_2-flow and low O_2-flow, this section addresses differences in the

emitted CO_2 amount, elemental composition and morphological changes observed in SEM.

6.5.1. Mass balances

Figure 6.4 shows the emitted amount of CO_2 in $mmol\,g^{-1}$ for high O_2-flow and low O_2-flow as measured by the MS. The detected CO_2 amount for high O_2-Flow is at 1000 $\mu mol\,g^{-1}$, whereas the CO_2 emission for low O_2-flow was at 0.6 $\mu mol\,g^{-1}$. This means a reduction of the emitted CO_2 amount of more than three orders of magnitude for low O_2-flow conditions. These results match with the absence of a mass loss for low O_2-flow discussed in the previous section.

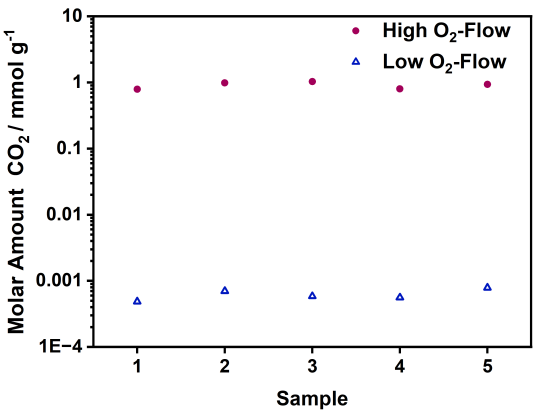


Figure 6.4. – Emitted CO_2 during low and high O_2-flow post-treatment conditions. The data was derived from mass spectrometry using $CaC_2O_4\,x\,H_2O$ as calibration substance.

Additionally, C, H, N, O elemental analysis was conducted to detect changes in the elemental composition between the carbon nanofibers at high and low O_2-flow conditions (Table 6.1).

Table 6.1. – C, H,N, O elemental composition for high O_2-flow, low O_2-flow and pristine carbon nanofibers after neutralization with distilled water. The O content was calculated as difference from C,H,N content for high O_2-flow and low O_2-flow. The elemental composition of the pristine carbon nanofibers was taken from [120].

Sample	C	H	N	O
	wt.-%	wt.-%	wt.-%	wt.-%
High O_2-Flow	59.8	2.2	12.7	25.3
Low O_2-Flow	69.6	1.7	10.7	18.0
Pristine fibers	72.6	1.4	16.2	9.8

The C content for low O_2-flow is 69.6 wt.-%, whereas it is at 59.8 wt.-% for high O_2-flow. This 10 wt.-% decreased C content can be related to the carbon combustion and possibly to oxidation of the carbon surface. For the H and N content no significant changes were observed between high O_2-flow and low O_2-flow. Regarding the O content, an increase of 7 wt.-% for high O_2-flow compared to low O_2-flow is observed. This is explained by the reduced amount of C relative to the O content and a partial oxidation of the carbon surface. However, the oxidation of the carbon surface would counteract the observed weight loss during the carbon combustion.

6.5.2. Raman spectroscopy

Raman measurements were conducted to determined structural changes of the carbon nanofibers. Both, the low and high O_2-flow carbon fibers, exhibit typical Raman spectra for amorphous carbon materials (Figure 6.5). The G-Band at 1580 cm^{-1} is assigned to E_{2g} vibrations of the graphite crystal lattice. The D-band at 1330 cm^{-1} is only observed if defects or disorder are present in the graphite structure. For the carbon fiber materials, the D-band is broad and intense compared to the G-band, indicating the presence of a highly unordered or defect-rich carbon lattice. The broad double-resonance $2D$ band between 2300 and 3300 cm^{-1} is present for all graphitic independent of lattice defects. In order to qualitatively compare the degree of crystallinity and structural disorder between different carbon compounds, the ratio of D-band to G-band integrals (D/G-ratio) is calculated.

The averaged D/G ratio for the low and high O_2-flow samples was at 5.77±0.09 for high O_2-flow and at 5.50±0.12 for the low O_2-flow sample. As evident from the calculated standard deviation, no significant variation of the Raman spectra were observed for the individual measurement spots of each sample. Furthermore, high D/G ratios were determined for both types of carbon fibers. These observations are attributed to the uniform, but highly amorphous carbon structure of the fibers, which is in line with the expectations for a low carbonization temperature of 800 °C. Moreover, no differences in D/G ratio and thus carbon amorphicity were observed within a 3σ (99.6 %) confidence interval. Therefore, no significant differences in carbon structure due to post-treatment could be shown for the two sample types based on the Raman results.

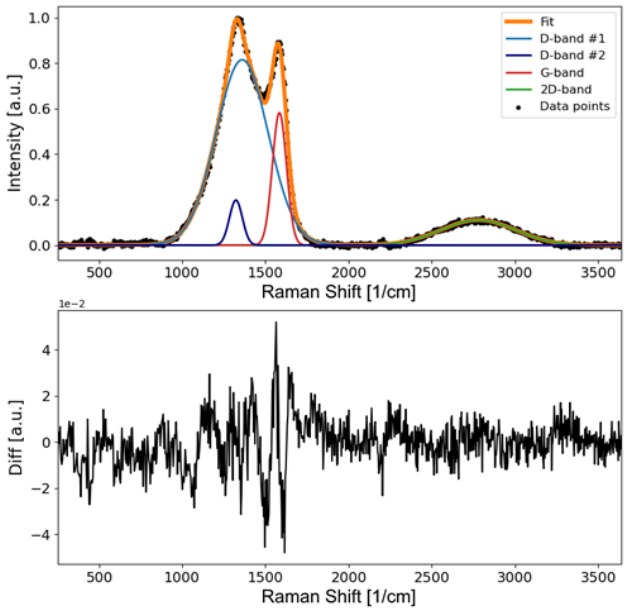


Figure 6.5. – Raman spectra of KOH-activated carbon nanofibers after the post-treatment at low O_2-flow.The Raman spectrum was fitted using 3 Gaussian fits for D, G and $2D$ band.

6.5.3. Electron microscopy

As the described glowing and combustion effect on the high O_2-flow samples might cause severe changes to the surface morphology of the carbon nanofibers, high O_2-flow and low O_2-flow samples were investigated with SEM (Figure 6.6). For reference purposes the pristine fibers [120] are shown in Figure 6.6 as well.

The pristine carbon nanofibers are randomly aligned and large void volumes are visible between the fibers. For the KOH-activated carbon nanofibers smaller void volumes and fragmented fibers are observed. The low O_2-flow samples exhibit a similar morphology as the pristine material (Figure 6.6 a vs. b). In contrast, high O_2-flow samples (see Figure 6.6d) exhibit areas with significant destruction of surface morphology compared to the pristine material Figure 6.6a. The formation of voids in the size of up to 3 microns is clearly visible in the SEM images Figure 6.6d.

These macropores are not homogeneously distributed on the surface of the High O_2-Flow samples as also areas with less severe destruction are visible Figure 6.6c. This observation could be explained by an inhomogeneous distribution of metallic potassium on the samples and, therefore, inhomogeneous severe heat formation due to the potassium oxidation reactions.

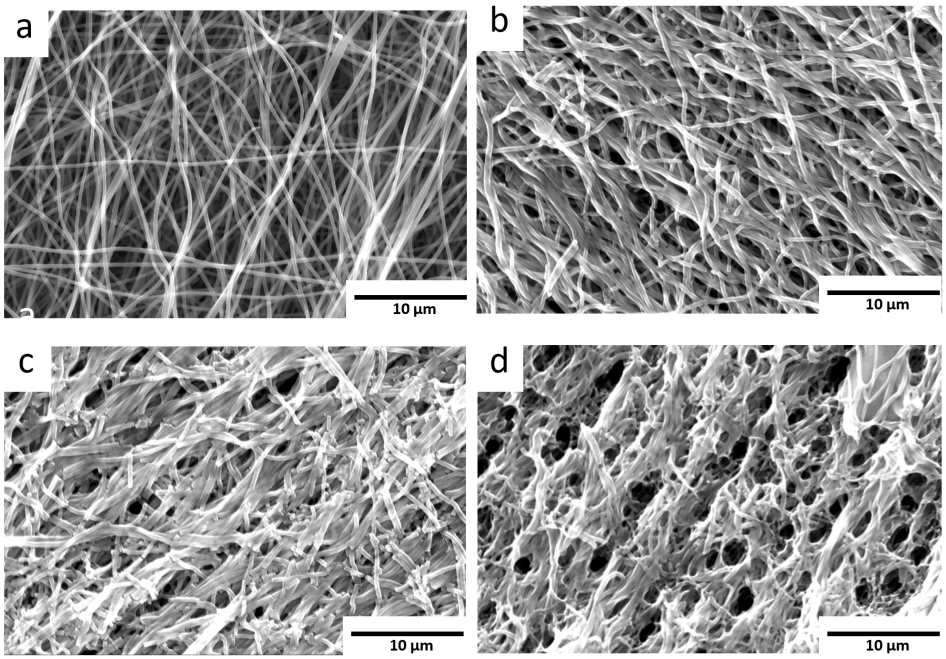


Figure 6.6. – (a) Pristine carbon nanofibers as reference material. (b) Low O_2-flow samples without visible destruction of the fiber morphology. (c) High O_2-flow samples with an area displaying a smaller degree of destruction. (d) High O_2-flow samples with severe destruction of the fiber morphology.

Summarizing, the SEM results prove that the control of post-treatment conditions significantly affects the morphology of the samples. The applied O_2-flow affects the potassium oxidation reactions and a severe destruction of the carbon nanofibers can be avoided by application of a low O_2-flow as post-treatment.

6.5.4. Gas adsorption properties

To obtain detailed information on the impact of the different post-treatment conditions on the pore structure and the adsorption properties, gas adsorption measurements were conducted on high O_2-flow and low O_2-flow samples. Argon adsorption measurements were performed at 87 K to assess the micropore volume. The adsorption isotherms exhibit a type I shape, which is typical for highly microporous adsorbents (Figure 6.7a). In the low relative pressure range a steep increase is observed, which flattens at higher relative pressures and approaches a limiting value. The isotherms exhibit similar shapes independent of post-treatment, although the adsorption capacities are significantly higher on the low O_2-flow samples. At 1 bar 17 mmol g^{-1} Ar are adsorbed on the low O_2-flow samples, whereas 31 mmol g^{-1} Ar are obtained for high O_2-flow. This equals an increase in adsorption capacity at 1 bar by 82 %.

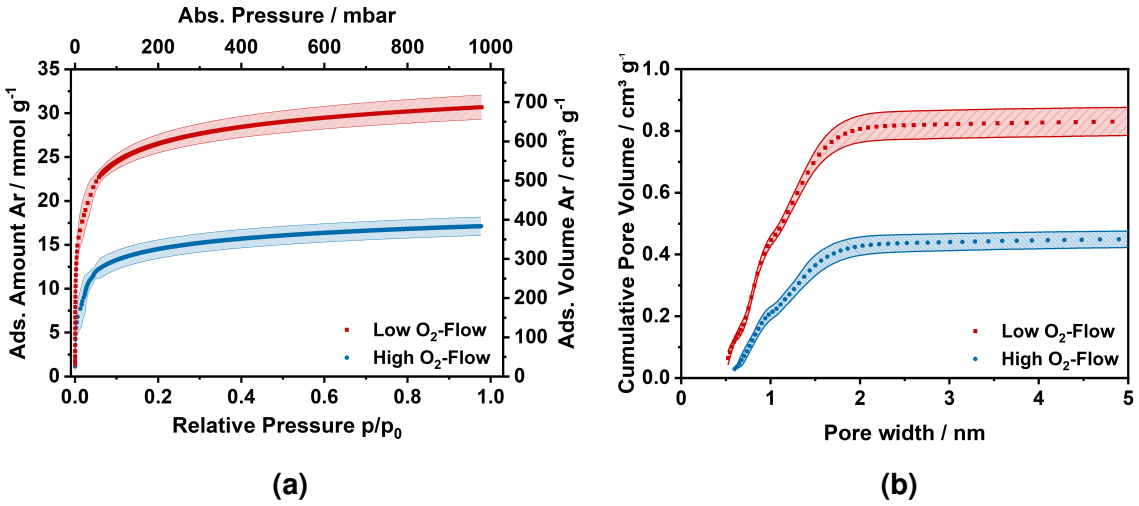


Figure 6.7. – (a) Ar adsorption isotherms at 87 K for low O_2-flow and high O_2-flow samples. An increase in adsorption capacity at 1 bar by 82 % is obtained. (b) Cumulative pore volume obtained from DFT calculations using a kernel for slit pores on carbon.

The pore size distribution was derived from the Ar adsorption isotherms using a QSDFT kernel. The cumulative pore size distributions for low O_2-flow and high O_2-flow are shown in Figure 6.7b. The comparison of the total pore volume $V_{DFT(tot)}$ and the pore volume of pores below 2 nm ($V_{DFT<2\,nm}$) reveals that both samples have almost exclusively micropores (Table 6.2). The micropore volume is 0.806 $cm^3\,g^{-1}$ for low O_2-flow samples, which is an increase of 90 % compared to 0.424 $cm^3\,g^{-1}$ for the high O_2-flow. Such values are comparable to values obtained by Im et al. and Chiang et al. for PAN-based activated carbon fibers [150, 156].

Table 6.2. – BET area, pore volume calculated by DFT calculations (V_{DFT}) and pore volume calculated using the Monte-Carlo method (V_{MC}) for low O_2-flow, high O_2-flow and the pristine fibers. Data is derived from the gas adsorption isotherms of Ar at 87 K and CO_2 at 273 K. The data for the pristine fibers is taken from [120].

Sample	BET	V_{DFT}	$V_{DFT<2nm}$	$V_{DFT<1.5nm}$	V_{MC}	$V_{DFT<0.7nm}$	$V_{MC<0.7nm}$
	$m^2\,g^{-1}$	$cm^3\,g^{-1}$	$cm^3\,g^{-1}$	$cm^3\,g^{-1}$	$cm^3\,g^{-1}$	$cm^3\,g^{-1}$	$cm^3\,g^{-1}$
High O_2-Flow	2029	0.831	0.806	0.696	0.605	0.173	0.208
Low O_2-Flow	1094	0.461	0.424	0.365	0.446	0.058	0.145
Pristine fibers	13.4	0.016	0.004	0.003	0.180	–	0.101

The BET area was determined at 1094 $m^2\,g^{-1}$ for high O_2-flow and at 2029 $m^2\,g^{-1}$ for low O_2-flow, which are typical BET areas of KOH-activated carbons [79, 157, 158]. Especially the direct comparison to the BET area of the pristine fibers (13.4 $m^2\,g^{-1}$) clearly proves a successful KOH activation of the electrospun PAN-based carbon nanofibers. Additionally, the high impact of the applied post-treatment conditions on the surface

morphology and porosity of the carbon nanofibers is obvious.

For more detailed micropore characterization CO_2 adsorption measurements at 273 K were performed. Figure 6.8 shows the CO_2 adsorption isotherms for the pristine [120], high O_2-flow and the low O_2-flow samples. The pristine fibers isotherm exhibits a high uptake at low relative pressures and turns more into a linear shape at higher relative pressures with a maximum CO_2 uptake of 2.7 mmol g^{-1} at 1 bar. In comparison, the adsorption isotherm of the high O_2-flow shows a lower CO_2 uptake at pressures below 200 mbar. At pressures above 200 mbar the adsorption isotherm of CO_2 surpasses the adsorption isotherm of the pristine fibers and rises to 4.7 mmol g^{-1} at 1 bar (Figure 6.8). Contrary, the low O_2-flow samples exhibit a similar uptake as the pristine fibers at

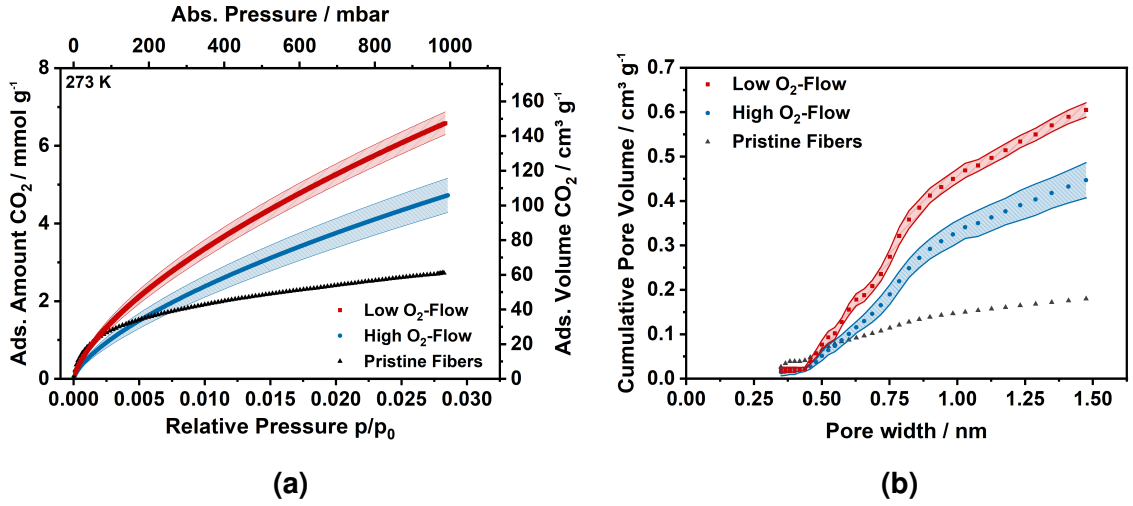


Figure 6.8. – (a) CO_2 adsorption isotherms at 273 K for high O_2-flow, low O_2-flow and the pristine carbon nanofibers. (b)The cumulative pore volume was determined from Monte-Carlo calculations using a kernel for slit pores on carbon.

low relative pressures and already surpasses the adsorption capacity of the pristine fibers at pressures of 75 mbar. At 1 bar it reaches an CO_2 adsorption capacity of 6.5 mmol g^{-1}, which is 38 % increase compared to the high O_2-flow samples and even 140 % increase compared to the pristine fibers. In comparison to literature data the obtained CO_2 adsorption capacities are among the highest for KOH-activated electrospun carbon nanofibers. Wang et al. reported CO_2 adsorption capacities of 2.9 mmol g^{-1} at 1 bar and 273 K, which is significantly lower than the reported values in the present work [89]. Comparable CO_2 adsorption capacities were reported by Chiang et al. and Zainab et al. who obtained 3.5 mmol g^{-1} at 298 K, which is close to the obtained 4.2 mmol g^{-1} at 293 K on the high O_2-flow sample in this study [118, 159].

The pore size distribution was determined using Monte-Carlo calculations and the cumulative pore volume is shown in Figure 6.8b. Similar to the previously described results of the DFT calculations, the pore volume increases for low O_2-flow samples over the full range of pore sizes compared to the high O_2-flow samples. The total pore volume is 0.61 $cm^3\,g^{-1}$ for low O_2-Flow and 0.45 $cm^3\,g^{-1}$ for high O_2-flow samples, resulting in an increase in pore volume of 36 % for the low O_2-flow samples. Regarding the ultramicropore volume (< 0.7 nm), high O_2-flow samples exhibit an amount of 0.15 $cm^3\,g^{-1}$, which is enhanced to 0.21 $cm^3\,g^{-1}$ on low O_2-flow samples. Overall, the pore volumes from CO_2 adsorption isotherms are comparable to those from Argon isotherms, except for a significant difference of the obtained micropore volume below 1.5 nm for DFT (0.365 $cm^3\,g^{-1}$) and Monte-Carlo (0.446 $cm^3\,g^{-1}$) data for high O_2-flow. This deviation could be caused by the different surface chemistry of samples prepared at high and low O_2-flow. High O_2-flow samples have a higher oxygen content than low O_2-flow samples, which could affect the interactions of adsorptive and adsorbent. Such effects are not accounted for in the standard calculation models used for the determination of the pore size distributions.

Furthermore, the isosteric enthalpy of adsorption was calculated for high and low O_2-flow based on CO_2 adsorption isotherms measured at 273 K, 283 K and 293 K using the approach of Clausius-Clapeyron. For low O_2-flow a value of 28.9 $kJ\,mol^{-1}$ was determined at a loading of 0.1 $mmol\,g^{-1}$ which slightly decreases to 27.1 $kJ\,mol^{-1}$ at a loading of 6.5 $mmol\,g^{-1}$ (Figure 6.9a). For high O_2-flow, the enthalpy of adsorption is at 27.4 $kJ\,mol^{-1}$ at a loading of 0.1 $mmol\,g^{-1}$ and decreases to 23.0 $kJ\,mol^{-1}$ at a loading of 5 $mmol\,g^{-1}$. Both isosteric enthalpies of adsorption are comparable to adsorption enthalpies of activated electrospun carbon nanofibers in literature [118]. The more distinctive decrease of the isosteric enthalpy of adsorption for high O_2-Flow can be linked to a higher degree of surface oxygen due to the partial carbon oxidation at high O_2-flow, which probably lowers the binding affinity towards CO_2 due to the increased number of acidic groups on the surface. To get an insight into the adsorption kinetics, equilibration curves of CO_2 at 50 mbar and 298 K were measured (Figure 6.9b).

For high and low O_2-flow the adsorption rate is fast, as the equilibrium loading is reached within the first 100 s with the steepest increase in the first 20 s. Comparing the two post-treatments, there are no significant changes of the adsorption kinetics. Therefore, the choice of post-treatment does not notably affect the adsorption rate of the carbon nanofibers.

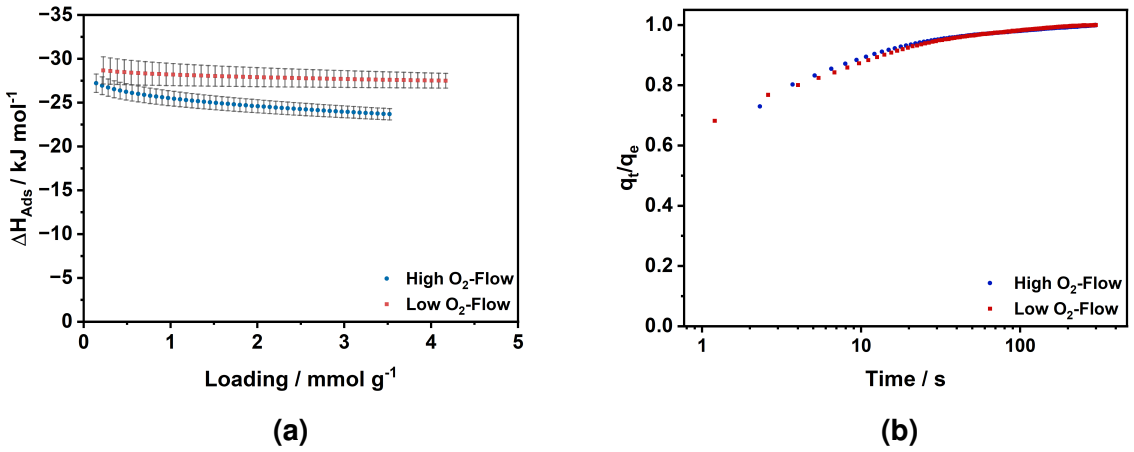


Figure 6.9. – (a) Isosteric enthalpy of adsorption for CO_2 on KOH-activated carbon nanofibers treated at high O_2 and low O_2-flow. Data determined using the Clausius Clapeyron approach and isostherm data at 273, 283 and 293 K. (b) Normalized adsorption kinetics for high and low O2-flow determined at 50 mbar and 298 K.

Overall, the low O_2-flow conditions result in improved gas adsorption properties, namely a higher adsorption capacity and a higher micropore volume. Furthermore, the isosteric enthalpy of adsorption is increased for low O_2-flow, whereas the adsorption kinetics are very similar for both post-treatments. Based on the results, the importance the choice of post-treatment conditions after KOH activation of electrospun carbon nanofibers becomes evident.

6.6. Potential triggers of a carbon combustion reaction

As stated in the previous sections the occurrence of vigorous potassium oxidation reactions with consecutive carbon combustion after KOH activation was not reported in literature so far. Although the proposed KOH activation mechanism involves the formation of metallic potassium and vigorous oxidation reactions are known for the intercalation of potassium into graphite [52, 145]. Therefore, the question arises, if certain material properties trigger the potassium oxidation induced carbon combustion reaction. To address this question several reference carbon materials were investigated focussing on the vigorous potassium oxidation reactions subsequent to KOH activation. To identify an influence of the material size, bulk materials, i.e. coconut shell and PAN powder, as well as carbon microfibers and carbon nanofibers were investigated. The reference materials were impregnated with KOH and subsequently exposed to the identical heat treatment as previously discussed carbon nanofibers. After cool down

after the activation treatment, the reference materials were treated at high O_2-flow conditions.

Figure 6.10 depicts the mass and temperature changes of the samples during post-treatment. The dimensions of the reference materials decrease from bulk to nanoscale. As bulk materials PAN powder and coconut shells were investigated. For PAN powder a mass gain of 0.5 wt.-% without a noteworthy temperature increase after the switch to high O_2-flow was observed. The coconut shells showed a similar development and an increase in mass of 1.5 wt.-% and a weakly pronounced temperature rise was determined during post-treatment. As no mass loss was detected for both, no indication for a carbon combustion reaction was found. The comparably low mass gain of the PAN powder during post-treatment is probably caused by a smaller amount of K present on the material, which results in a smaller weight gain due to K oxidation. Potential causes for a lower amount of metallic K could be a less sufficient impregnation with KOH prior to the activation.

As no carbon combustion reactions were found on bulk materials, carbon microfibers were investigated as second group of reference materials. Commercially available carbon microfibers, typically applied as electrode materials, were used. The carbon papers were pyrolyzed at 1000 °C prior to activation to remove flourine residues from hydrophobic treatment of the materials. The mass gain during post-treatment is just at 0.25 wt.-% on both samples. The low mass gain is an indication for an insufficient KOH impregnation prior to the activation treatment. The commercial carbon papers are hydrophobic even without the flourine as they were carbonized at temperatures $>$ 1000 °C. Therefore, the aqueous KOH could probably not wet the fibers sufficiently. Due to the insufficient wetting, no reliable statement on the effects of the dimension of the material on the carbon combustion could be made.

As third size class, carbon nanofibers were investigated. The precursor PAN-based nanofibers were obtained on an IME electrospinner equipped with a 4-tip nozzle and custom-made needleless spun nanofibers were obtained from Stellenbosch Nanofiber Company (SNC, South Africa). The SNC fibers showed a mass gain of 0.7 wt.-% during post-treatment and no temperature rise. Therefore, no carbon combustion reaction occurred.

In contrast, the inhouse spun nanofibers showed a high mass gain of 1.5 wt.-% and a significant temperature rise at post-treatment. After 330 s, a mass loss related to the start of the carbon combustion occurs. Taking a closer look on the properties of both nanofibers, a significant difference in the fiber diameter distribution was observed. The

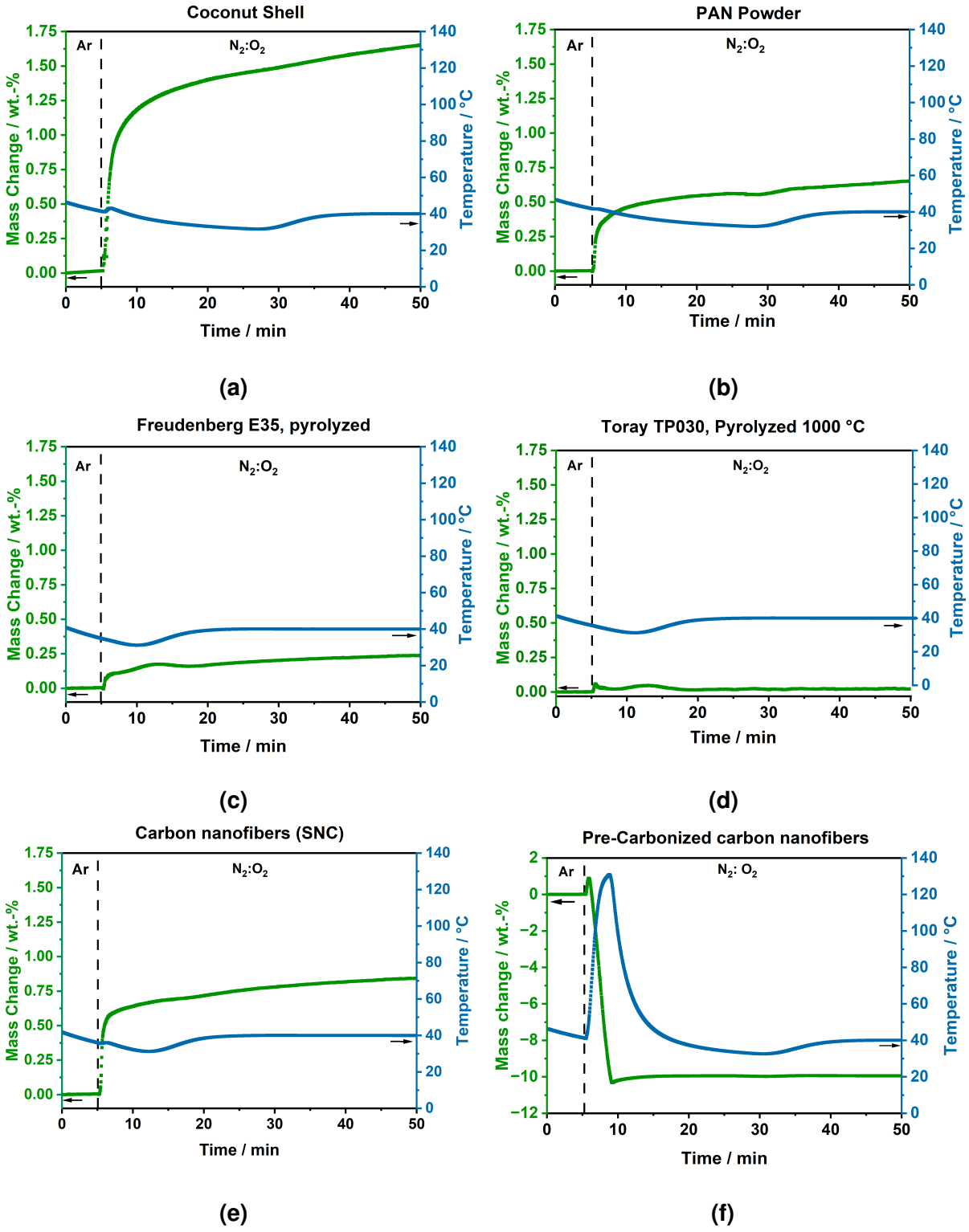


Figure 6.10. – TGA-DSC results for various carbon reference materials. All samples were KOH-activated with subsequent exposure to high $_{O2}$-flow conditions.

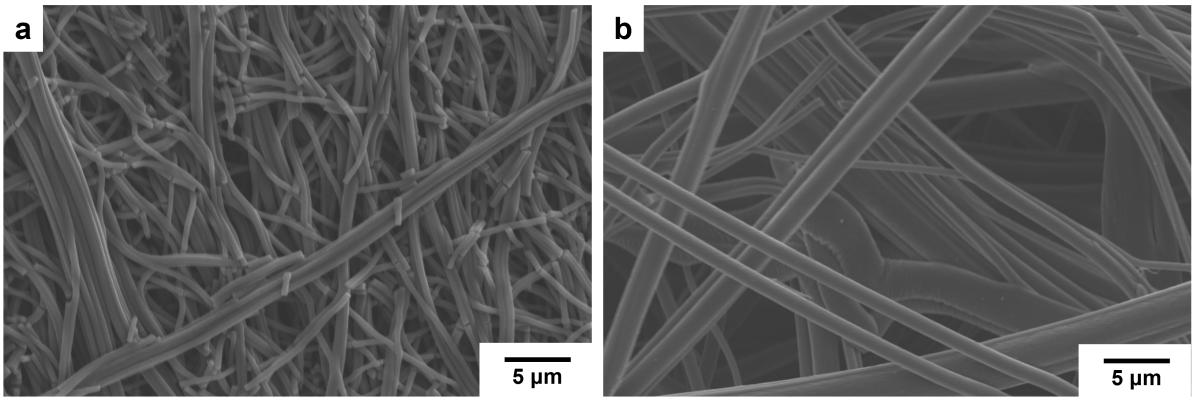


Figure 6.11. – (a) Inhouse spun carbon nanofibers showing a quite uniform fiber diameter distribution. (b) Custom-made carbon nanofibers (Stellenbosch Nanofibers Company, SNC, South Africa, which show a significantly broader pore size distribution

inhouse made fibers showed quite homogeneously distributed diameters ranging from 200 to 300 nm. Contrary, the SNC nanofibers have a broad distribution ranging from 200 nm to the size of 1 to 2 µm. This could be an explanation for the different reactions during post-treatment and a hint to the size effects on the carbon combustion reaction. The smaller size of the nanofibers could affect the diffusion processes of potassium as well as oxygen within the carbon nanofiber mats. The smaller the fiber diameter, the faster the oxidation of potassium occurs, causing a high heat formation in a short period of time resulting in the carbon combustion.

In total, the investigations on the reference materials indicate an effect of the material size on the potassium oxidation reactions and thus the occurrence of a carbon combustion reaction. However, the results are currently not unambiguous and additional experiments are necessary to clarify and prove the hypothesis of a size dependent effect.

7. Characterization of KOH-Activated carbon nanofibers

7.1. Preface

A series of KOH-activated carbon nanofibers at KOH:Fiber weight ratios of 1:4 to 3:4 was synthesized using a simultaneous carbonization and activation approach at 800 °C in Ar. Prior to the carbonization and activation the samples were stabilized at 250 °C for 15 h in air. Subsequent to carbonization and KOH activation the developed low O_2-flow post-treatment was applied (chapter 6). The KOH-activated carbon nanofibers were processed into cylindrical pellets. This is advantageous compared to carbon nanofiber mats due to a simplified handling and improved packing properties inside an adsorber column, which is interesting for consecutive breakthrough experiments discussed in chapter 8.
The material synthesis and characterization using SEM and gas adsorption were conducted by Tom Fischer. The elemental analysis was performed by the Central Institute of Analytics at Forschungszentrum Jülich GmbH.

7.2. Electron microscopy

The SEM images of the carbon nanofibers pellets were recorded to ensure a successful synthesis of the cylindrical pellets, while the carbon nanofiber structure is still maintained. In Figure 7.1a, the cross-section of a cylindrical pellet with a diameter of roughly 2 mm and a relatively smooth surface is shown. At increased magnification the pellet structure appears rougher and the single carbon nanofibers are getting visible (Figure 7.1b,c). At the highest magnification, densely packed carbon nanofibers could be identified. Compared to the carbon nanofiber mats a significant reduction of the fiber length and the void between the single carbon nanofibers could be observed.

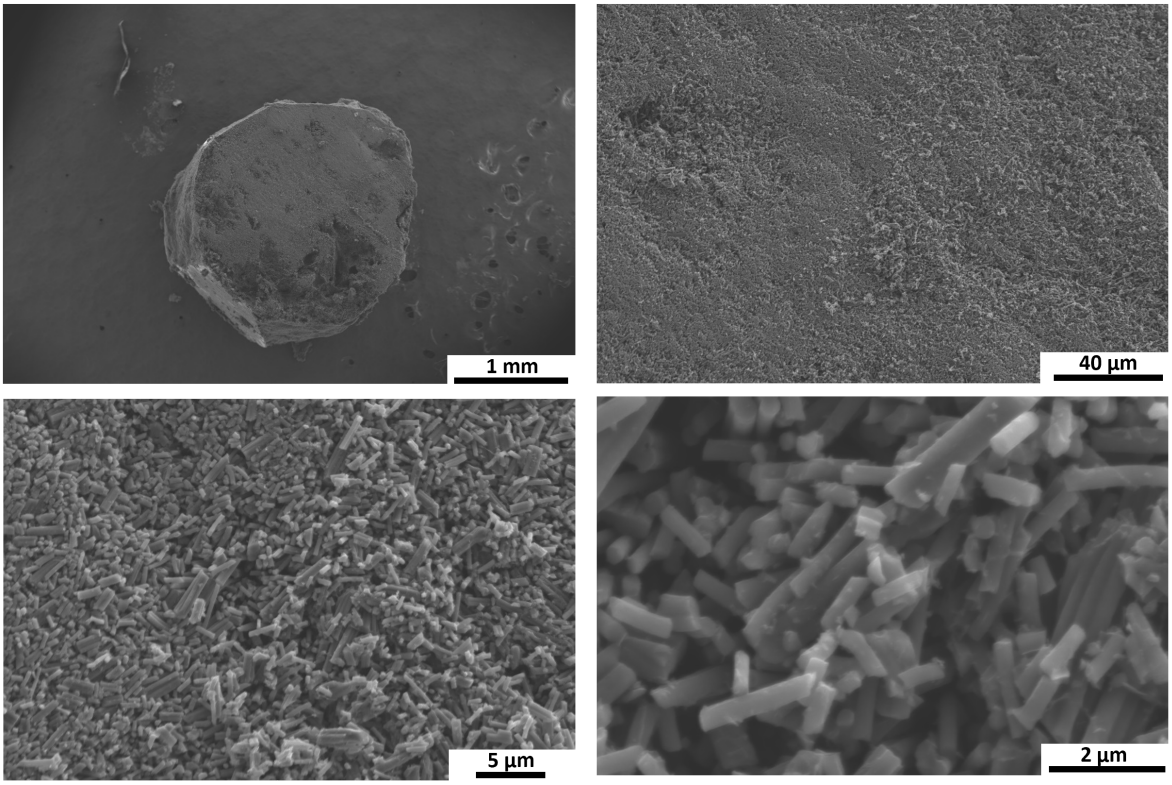


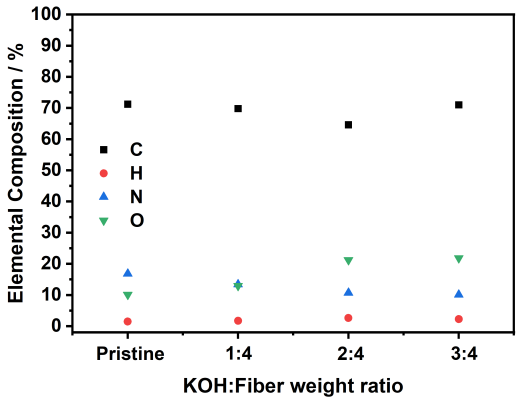
Figure 7.1. – SEM images of KOH-activated carbon nanofiber pellets (KOH:Fiber 1:4) at different magnifications. A densely packed cylindrical pellet was synthesized, preserving the single carbon nanofiber structure. A decrease in the fiber length and in void volume was observed.

Overall, the SEM images prove the successful transformation of the KOH-activated carbon nanofiber mats into cylindrical carbon nanofiber pellets with a diameter of 2 mm and a length of 4 mm. No significant differences in morphology of the pellets for the different KOH:Fiber ratios were found.

7.3. Elemental composition

Elemental analysis was conducted to determine changes in the C, H, N and O content of the KOH-activated carbon nanofibers at different KOH:Fiber ratios (Figure 7.2). The reference material, pristine carbon nanofibers, has a carbon content of 71.2 wt.-% and an H content of 1.5 wt.-%. The hetero atom contents are at 16.8 wt.-% nitrogen and 10.1 wt.-% oxygen, respectively. These values are comparable to previously reported elemental composition of pristine PAN-based carbon nanofibers [120]. At a KOH:Fiber ratio of 1:4 the C content slightly decreases to 69.8 wt.-%. In the meantime a decrease of the N content to 13.4 wt.-% and an increase of O to 12.9 wt.-% is visible. This development

continues at higher KOH:Fiber ratios and results in an O content of 21.8 wt.-% and an N content of 10.0 wt.-%, respectively. The C and H content show only small variations. The increase of O in the carbon nanofibers is caused by the KOH activation, which etches the carbon, causing the formation of oxygen containing functional groups, such as hydroxyl, carbonyl and carboxyl groups.



(a)

Figure 7.2. – Elemental composition of KOH-activated carbon nanofibers at KOH:Fiber weight ratios of 1:4 to 3:4. The pristine carbon nanofibers are given as reference.

7.4. Pore characterization

The KOH-activated carbon nanofibers were characterized by gas adsorption measurements using Ar, CO_2 and H_2O to determine adsorption capacities, adsorption enthalpies as well as pore size distributions.

7.4.1. Ar adsorption

Ar adsorption isotherms at 87 K are depicted in Figure 7.3a,b. The pristine carbon nanofibers and the carbon nanofibers activated at a KOH:Fiber weight ratio of 1:4 show a type II adsorption isotherm, which is typical for non-porous or macroporous adsorbents. The adsorbed amount of Ar stays fairly low with a maximum capacity below 0.8 mmol g^{-1} at 1 bar for both samples. Opposite to this, the adsorption isotherms of the samples activated at KOH:Fiber weight ratios of 2:4 and 3:4 show type I shapes. These are typical for adsorption on microporous adsorbents. Already at very low relative pressures

a high amount of Ar is adsorbed, before the isotherm approaches a limiting value at higher relative pressures. In total, the adsorbed amounts are at 11.1 and 21.3 mmol g^{-1}, respectively.

The adsorption data was used to determine the BET area of the samples. For the pristine carbon nanofibers and the carbon nanofibers activated at a KOH:Fiber weight ratio of 1:4 small BET areas of 10 and 5 $m^2 g^{-1}$ were obtained in a p/p_0 range of 0.05-0.3. For samples activated at KOH:Fiber weight ratios of 2:4 and 3:4 the BET area increases significantly and values of at 708 and 1432 $m^2 g^{-1}$ in p/p_0 range of 0.05-0.1 were determined. The p/p_0 range was adjusted due to the limitations of the BET theory on microporous materials [100]. The large BET areas are in good agreement to literature data, e.g. Kim et al. obtained a BET area of 1726 $m^2 g^{-1}$ [157]. The change of the adsorption isotherm shape and capacity as well as the high increase in BET area clearly proof a successful KOH activation of the carbon nanofibers.

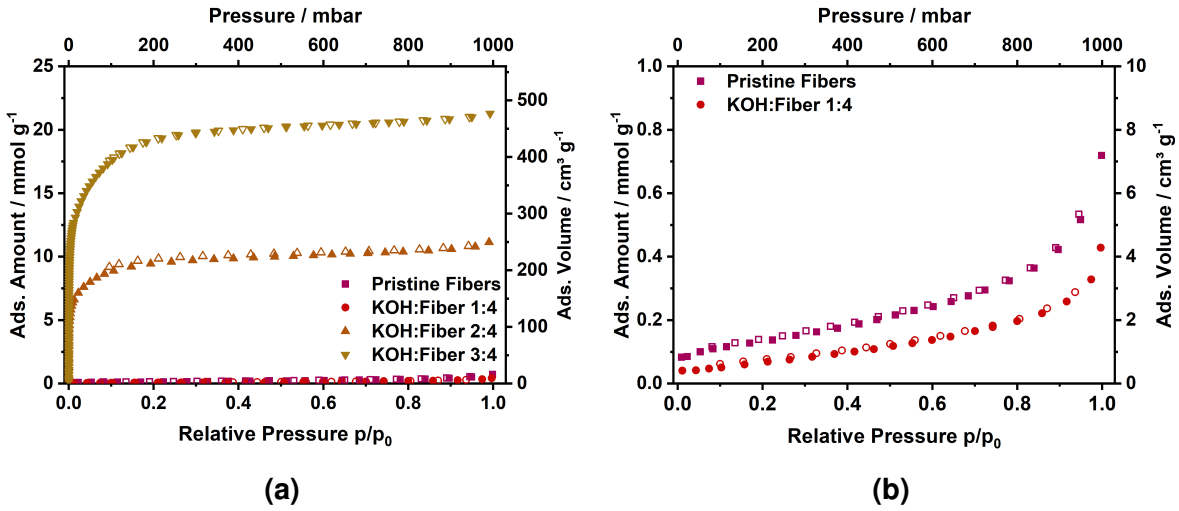


Figure 7.3. – (a) Ar adsorption isotherms obtained at 87 K for KOH activated carbon nanofibers at KOH:Fiber ratios of 1:4 to 3:4. The pristine fibers are shown as reference material. (b) Magnified depiction of the Ar adsorption isotherms of the pristine carbon nanofibers and the KOH:Fiber 1:4 sample. Open symbols show the desorption branches.

As more profound characterization of the carbon nanofibers, DFT calculations allow to determine the incremental and cumulative pore size distribution using a kernel for slits pores on carbon. The cumulative pore volume changes in a similar manner as the shape of the Ar isotherms. For the pristine sample and the carbon nanofibers activated at a KOH:Fiber weight ratio ratio of 1:4 negligible cumulative pore volumes of 0.02 and 0.01 $cm^3 g^{-1}$ were determined, whereas on samples activated at KOH:Fiber weight ratio of 2:4 and 3:4 cumulative pore volumes of 0.30 and 0.58 $cm^3 g^{-1}$ were obtained (Figure 7.4 and Table A.4). This equals an increase in cumulative pore volume of almost

two orders of magnitude. Taking a look on the incremental pore volume it is evident, that KOH activation at KOH:Fiber weight ratio ratios of 2:4 and 3:4 results in the formation of a high micropore volume and especially a high amount of pores below 1 nm. In contrast, for the pristine carbon nanofibers and the sample activated at a KOH:Fiber weight ratio ratio of 1:4 the micropore volume is negligible.
All in all, the Ar adsorption measurements clearly show a strong effect of the KOH activation on the pore volume of the carbon nanofibers. Especially, at higher KOH:Fiber weight ratios of 2:4 and 3:4, highly microporous carbon nanofibers with large BET areas are obtained.

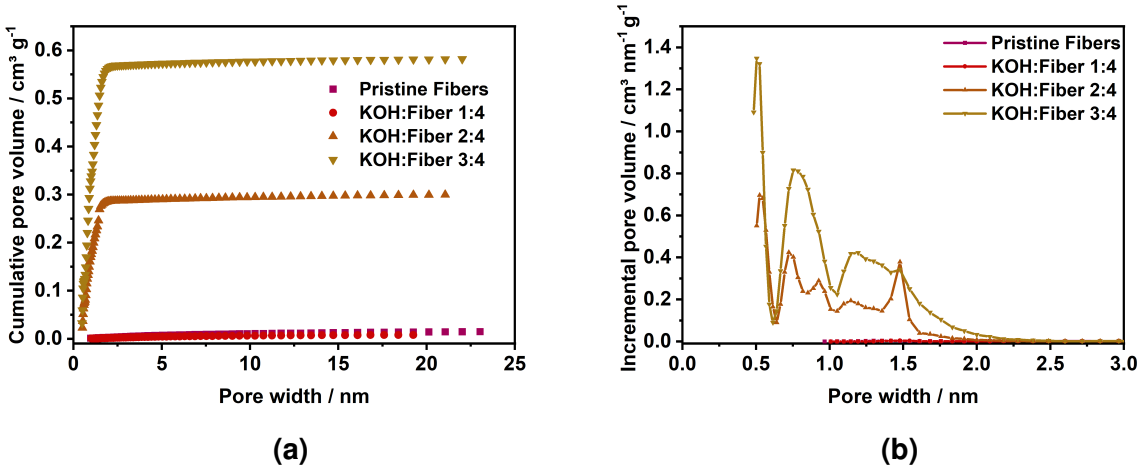


Figure 7.4. – (a) Cumulative and (b) incremental pore size distribution of the pristine carbon nanofibers and for samples activated at KOH:Fiber weight ratios of 1:4, 2:4 and 3:4. The results are based on DFT calculations using Ar isotherm data.

7.4.2. CO_2 adsorption

Additionally, CO_2 adsorption isotherms were recorded at 273 K to assess the adsorption capacities as well as the pore size distribution in the narrow micropore region. All samples have type-I shaped isotherms, which are characteristic for highly microporous adsorbents (Figure 7.5a). In detail, the isotherms of the pristine carbon nanofibers and the carbon nanofibers activated at a KOH:Fiber weight ratio of 1:4 show steep slopes at low relative pressures, which flatten at higher relative pressures and approach limiting values of 2.11 and 2.74 mmol g^{-1} at 1 bar absolute pressure. Contrary, the samples activated at KOH:Fiber weight ratios of 2:4 and 3:4 show similar steep slopes at low relative pressures, but turn into a linear slope at higher relative pressures. Their adsorption capacities at 1 bar are at 4.1 and 5.4 mmol g^{-1}. For better assessment of

the changes in the low relative pressure region, Figure 7.5b shows a magnification for relative pressures below 0.010, which equals an absolute pressure smaller than 400 mbar. The magnification shows a higher adsorption capacity of the KOH-activated materials compared to the pristine carbon nanofiber material already at 75 mbar absolute pressure.

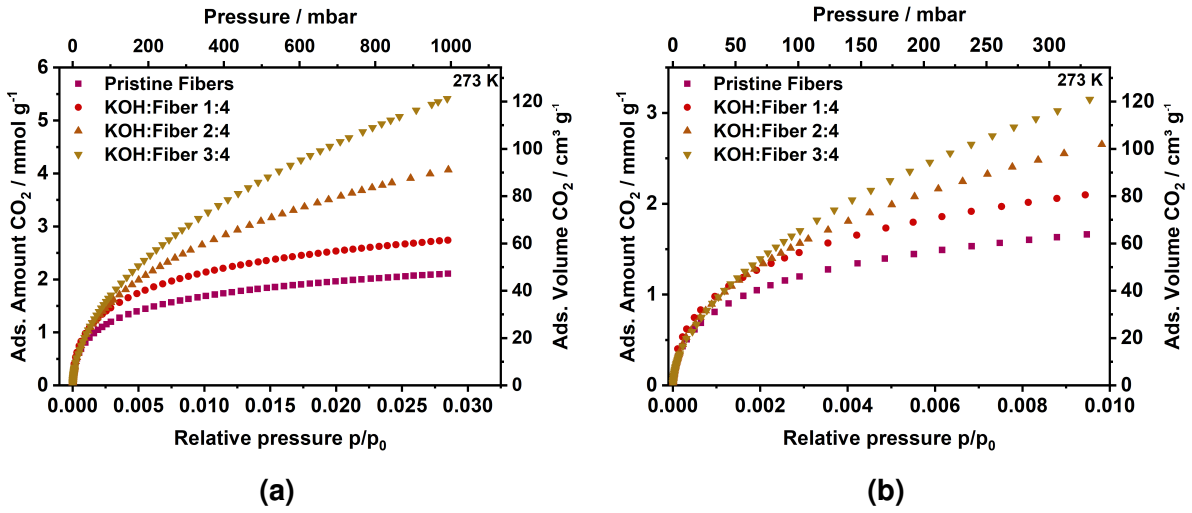


Figure 7.5. – (a) CO_2 adsorption isotherms at 273 K on KOH-activated carbon nanofibers activated at KOH:Fiber ratios 1:4 to 3:4 and the pristine nanofibers. (b) Magnification of the isotherm region below 400 mbar to assess differences in the low-pressure regime.

The isotherm data was used to determine the pore size distribution using Monte-Carlo calculations with a kernel for slit pores on carbon. The cumulative pore volume is depicted in Figure 7.6a. All four samples have a similar, but very low, cumulative pore volume at very narrow pore sizes < 0.5 nm. At higher pore widths the cumulative pore volume clearly changes and significant differences between the different samples are visible. The pristine material has a steep increase in pore volume from 0.045 $cm^3\,g^{-1}$ to 0.087 $cm^3\,g^{-1}$. Afterwards the slope flattens resulting in a total cumulative pore volume of 0.110 $cm^3\,g^{-1}$. A similar development is observed on carbon nanofibers activated at a KOH:Fiber weight ratio of 1:4. However, the increase is more pronounced, which is caused by the slight activation of the sample. At higher activation ratios (KOH:Fiber 2:4 and 3:4) this development is even more pronounced. For carbon nanofibers activated at a KOH:Fiber weight ratio of 2:4 a cumulative pore volume of 0.277 $cm^3\,g^{-1}$ is determined, which is even surpassed by the sample activated at a KOH:Fiber weight ratio of 3:4 with a cumulative pore volume of 0.412 $cm^3\,g^{-1}$. This clearly points out the strong impact of KOH activation on the pore volume of the carbon nanofibers. Interestingly, the incremental pore volume shows a sharp peak at very narrow pore widths on pristine

carbon nanofibers and samples activated at a KOH:Fiber weight ratio of 1:4 (Figure 7.6b). At higher KOH:Fiber weight ratios of 2:4 and 3:4 this peak is vanished. This indicates the presence of very narrow ultramicropores on the pristine carbon nanofibers and the sample activated at a KOH:Fiber weight ratio of 1:4. However, it might also be an artefact due to deviations between the used kernel and the actual adsorbent properties. Nonetheless, a clear growth in pore width with increasing KOH:Fiber ratios is observed. The KOH activation mainly generates pores in the range of 0.5 to 1.2 nm.
The results are in good agreement to the previously discussed DFT calculations. Both data sets, DFT and Monte-Carlo pore size distributions were combined to illustrate and discuss changes in pore volume for the regions of ultramicropores (<0.7nm), supermicropores (0.7-2 nm) and mesopores (>2 nm). In Figure 7.6 the pristine carbon nanofibers mainly exhibit pores in the ultramicropore region. A development of wider micropores with a width up to 2 nm is observed for higher KOH:Fiber ratios. However, almost no mesopores are formed during KOH activation.

Table 7.1. – BET area, ultramicropore volume, supermicropore volume, mesopore volume and total pore volume for KOH-activated carbon nanofibers stabilized at KOH:Fiber ratios of 1:4, 2:4 and 3:4. As reference material the pristine fibers are listed.

KOH:Fiber	BET Area	V_{DFT}	V_{MC}	V_{Ultra}	V_{Super}	V_{Meso}
	$m^2\,g^{-1}$	$cm^3\,g^{-1}$	$cm^3\,g^{-1}$	$cm^3\,g^{-1}$	$cm^3\,g^{-1}$	$cm^3\,g^{-1}$
Pristine Fibers	9.6	0.015	0.110	0.086	0.024	0.012
KOH:Fiber 1:4	5.2	0.008	0.146	0.113	0.033	0.007
KOH:Fiber 2:4	707.9	0.300	0.277	0.161	0.132	0.014
KOH:Fiber 3:4	1432.3	0.582	0.412	0.205	0.263	0.020

Since KOH activation involves several chemical reactions and significantly alters the material properties, changes in the adsorption energies were analyzed by determination of the isosteric enthalpies of adsorption. Based on adsorption isotherms at 273, 283 and 293 K the determination was conducted using the Clausius-Clapeyron approach [107]. In Figure 7.6d the isosteric enthalpies of adsorption are shown for all four samples.
The pristine carbon nanofibers have an adsorption enthalpy of -34 $kJ\,mol^{-1}$ at low adsorbed amounts. At proceeding adsorption the enthalpy decreases with increasing slope at higher adsorbed amounts, which reflects well the discussed pore size distribution. At the beginning of the adsorption the most favorable sites, the ultramicropores with a high enthalpy of adsorption, are filled. Since the pristine carbon nanofibers have almost exclusively ultramicropores, a decrease of the isosteric enthalpies to -23 $kJ\,mol^{-1}$ is observed at higher adsorbed amounts. The remaining larger micropores and mesopores are less beneficial adsorption sites with lower adsorption potentials. On carbon nanofibers

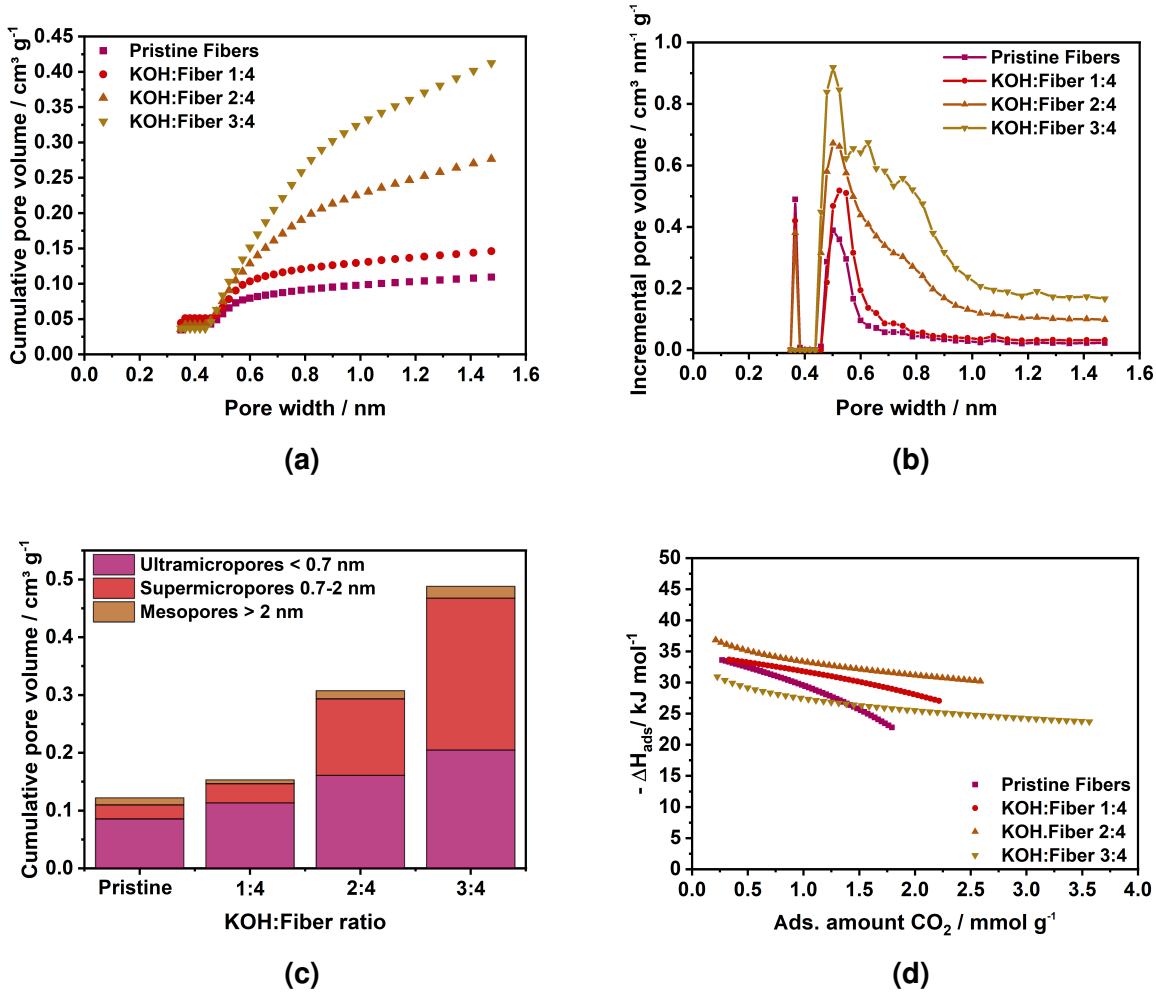


Figure 7.6. – (a) Cumulative and (b) incremental pore size distribution of the pristine carbon nanofibers and carbon nanofibers activated at KOH:Fiber weight ratios of 1:4 to 3:4 based on Monte-Carlo calculations using CO_2 isotherm data. (C) Cumulative pore size distribution for four samples based on a combination of DFT data from Ar isotherms and Monte-Carlo calculations based on CO_2 isotherms. (d) Isosteric enthalpy of adsorption for CO_2 determined via Clausius-Clapeyron approach using CO_2 isotherm data obtained at 273, 283 and 293 K.

activated at KOH:Fiber weight ratios of 1:4 a similar course is observed. For low loadings an identical adsorption enthalpy of -34 kJ mol^{-1} is determined. However, the decrease is less distinctive and results in -27 kJ mol^{-1}. This change of the isosteric enthalpies at higher loadings is related to the changed pore structure due to the slight KOH activation. The carbon nanofibers activated at a KOH:Fiber weight ratio of 1:4 have a higher ultra- and supermicropore volume. Especially, the increase of supermicropore volume could explain the smaller decrease of the adsorption enthalpies at higher adsorbed amounts since a higher number of pores is accessible.

Contrary, the courses for samples activated at KOH:Fiber weight ratios of 2:4 and 3:4 significantly change compared to the previous ones. The initial enthalpy of adsorption

is at -31 kJ mol^{-1} for carbon nanofibers activated at KOH:Fiber weight ratio of 2:4 and at -37 kJ mol^{-1} for the samples activated at a KOH:Fiber weight ratio of 3:4. At higher adsorbed amounts the adsorption enthalpy decreases and turns into a linear descent, which is almost horizontal. The lower initial enthalpy of adsorption on carbon nanofibers activated at a KOH:Fiber weight ratio of 2:4 could be assigned to the broader pore size distribution and the slightly lower amount of narrow ultramicropores on these samples. The strong deviation of carbon nanofibers activated at a KOH:Fiber weight ratio of 3:4 might be caused by significant measurement uncertainties since the highest error was obtained for the calculation.
The reduced slope of the descent at higher adsorbed amounts on both samples compared to samples activated at lower KOH:Fiber weight ratios is assigned to the broadened pore size distribution, which exhibits pores over the entire micropore region. Thus, a high number of pores at different adsorption potentials is available.
All in all, KOH activation has a significant influence on the morphology and porosity of the material, which directly affects the adsorption properties of the carbon nanofibers.

7.4.3. H_2O adsorption

The water adsorption properties of a material are important characteristics to assess the suitability as CO_2 adsorbent since CO_2 containing gas streams, such as flue gas, contain high amounts of humidity. As assessment of the water affinity, water adsorption isotherms at 298 K were recorded for all adsorbents (Figure 7.7). At a relative humidity below 30 %, almost linear ascending adsorption isotherms are obtained on all samples. The adsorbed capacities differ only slightly in this area and at a relative humidity of 30 % adsorbed amounts of 4.1-5.7 mmol g^{-1} H_2O were determined. At higher relative humidity the slope of the pristine carbon nanofibers and sample activated at KOH:Fiber weight ratio of 1:4 flattens and approaches a limiting value of 5.0 mmol g^{-1}, respectively 7.0 mmol g^{-1}. Contrary, the slope of the carbon nanofibers activated at KOH:Fiber weight ratios of 2:4 and 3:4 rises strongly at relative humidities above 30 % and flattens again at relative humidities > 60 %. The maximum capacities are at 23.6, respectively 25.9 mmol g^{-1}.
Based on the proposed mechanism, H_2O adsorption on porous carbons occurs preferentially at oxygen-containing surface groups. The adsorbed water molecules act as cluster formation sites, which allow for additional adsorption of water due to hydrogen bondings [140, 160]. However, this cluster formation can be limited by the pore width. The narrow ultramicropores on the pristine carbon nanofibers and the KOH-activated

carbon nanofibers at a weight ratio of 1:4, limit the cluster formation resulting in a type I shaped isotherm with comparatively low H_2O capacities [161].

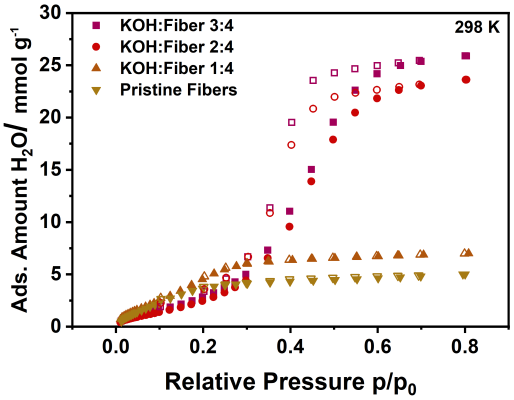


Figure 7.7. – H_2O vapor isotherms measured at 298 K on KOH-activated carbon nanofibers at activated at KOH:Fiber weight ratios 1:4 to 3:4. The pristine carbon nanofibers are shown as reference.

In contrast, the H_2O isotherms on carbon nanofibers activated at KOH:Fiber weight ratios of 2:4 and 3:4 are S-shaped type V isotherms, which are typical for water adsorption on activated carbons [162–164]. Both samples show a strong hysteresis. This adsorption behavior is mainly caused by a high degree of oxygen containing surface functional groups, which preferentially adsorb water. The adsorbed water molecules act as cluster formation sites for additional adsorption of water due to the hydrogen bondings. At low relative pressures only a small amount of water is adsorbed on the functional groups of the carbon, whereas the steep increase at medium relative pressures is assigned to the formation of H_2O clusters. Compared to the pristine and carbon nanofibers activated at a KOH:Fiber weight ratio of 1:4, the higher activation degree resulted in larger pore width and thus the pore widths are not limiting cluster formation (chapter 7).
Additionally, a high number of oxygen functional groups is introduced during the KOH activation step at high KOH:Fiber activation ratios, resulting in the formation of carbonyl, hydroxyl and carboxyl groups on the surface, which is favorable for H_2O adsorption. This is confirmed by the elemental analysis, which showed an oxygen content of 21.2 and 21.8 wt.-% for KOH:Fiber 2:4 and 3:4. This is signifcantly higher than 10.0 and 12.9 wt.-% determined on pristine and carbon nanofibers activated at a KOH:Fiber weight ratio of 1:4.
All in all, the water adsorption results show a strong affinity of water to the adsorbent, which might likely affect the separation of CO_2 from the gas stream due to competing adsorption processes.

8. Separation of a CO_2/N_2 mixture on KOH-activated carbon nanofibers

8.1. Preface

A potential field of application for carbon nanofibers is the separation of CO_2 from flue gas [32, 110, 118]. The requirements of an adsorbent for CO_2 capture were discussed in detail in chapter 1. This chapter investigates the potential of the KOH-activated carbon nanofibers, which were characterized in chapter 7, for application in a CO_2 separation process. Thus, the separation of CO_2 from a mixture of CO_2 and N_2 is analyzed. Typical adsorbent metrics, i.e. CO_2 selectivity, cycle stability and working capacity are addressed. Furthermore, an in-depth comparison of IAST and experimentally determined selectivity values is given to show the added value of experimental determinations.
The static and dynamic gas adsorption measurements as well as the data processing and evaluation presented in this chapter were conducted by Tom Fischer.

8.2. Determination of CO_2/N_2 selectivity based on the ideal adsorbed solution theory

The ideal adsorbed solution theory (IAST) is commonly applied to calculate selectivities for gases in binary mixtures. A calculation based on the IAST requires only experimental data of the pure component isotherms for both components [103, 105]. A summarizing description of the fundamentals, assumptions and shortcomings of IAST was discussed in subsection 2.4.5. In the following section, the IAST is used to determine the CO_2 selectivity of the pristine and KOH-activated carbon nanofibers in a binary mixture of 10 % CO_2 in 90 % N_2 at 298 K at 1 bar.

The pure component isotherms of CO_2 and N_2 were determined by static gas adsorption measurements at 298 K (Figure 8.1). The shapes of the CO_2 adsorption isotherms are similar to the ones discussed in the previous chapter, but show a decreased adsorption capacity due to the increased measurement temperature (Figure 7.5a). Thus, the adsorption capacity at 1 bar reduces from 5.4 mmol g^{-1} (273 K) to 3.2 mmol g^{-1} (298 K) for the carbon nanofibers activated at a KOH:Fiber weight ratio of 3:4. Similar developments are observed for the lower KOH:Fiber weight ratio samples and the pristine carbon nanofibers.

The N_2 isotherms show almost linear isotherm shapes with comparably low adsorbed amounts of 0.22 and 0.34 mmol g^{-1} at 900 mbar (Figure 8.1b). The N_2 adsorption capacity increases with ascending KOH:Fiber weight ratios. Compared to the adsorbed amount of CO_2, the N_2 adsorption is reduced by one order of magnitude. The clear differences between the CO_2 and N_2 isotherms are first indications for a high selectivity of CO_2 towards N_2 on the adsorbent.

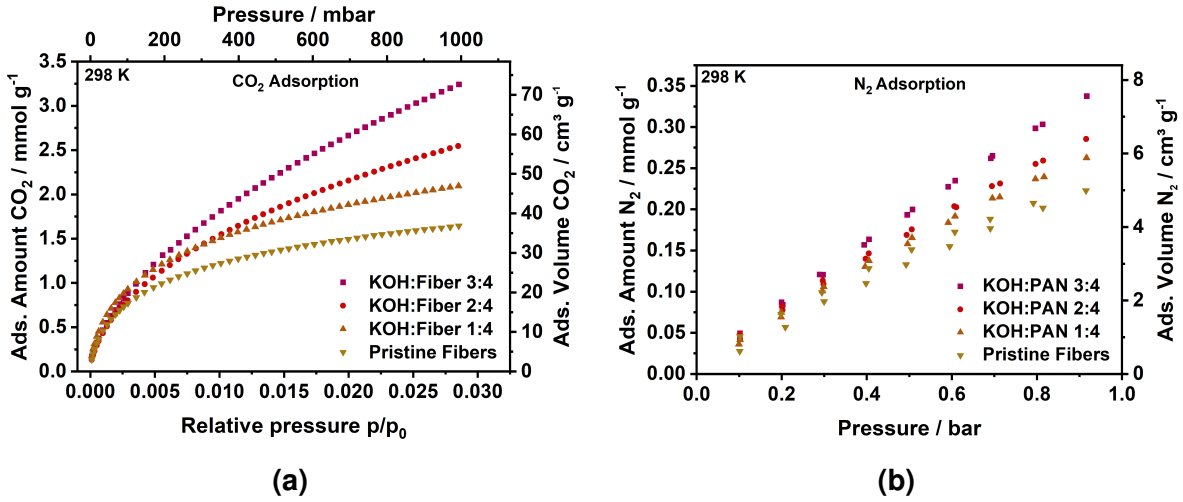


Figure 8.1. – (a) CO_2 and (b) N_2 adsorption isotherms at 298 on KOH-activated carbon nanofibers activated at KOH:Fiber weight ratios of 1:4, 2:4 and 3:4 as well as pristine carbon nanofibers.

For IAST calculations, CO_2 and N_2 isotherms were fitted using the empirical Toth Fit (Equation 8.1). The three fit parameters are the saturation capacity Q_{max}, the affinity constant k and the heterogeneity factor t.

$$q_{eq} = q_{max} \cdot \frac{K \cdot p}{(1 + (K \cdot p)^t)^{\frac{1}{t}}} \tag{8.1}$$

In order to obtain physically meaningful fit data, the saturation capacity Q_{max} was limited to 10 mmol g^{-1} for the CO_2 adsorption isotherms and limited to 3 mmol g^{-1} for

the N_2 isotherms. All additional fit parameters were left without any constraints for both adsorptives.

Table 8.1. – Toth isotherm fit parameters, saturation capacity Q_{max}, affinity constant k and heterogeneity factor t, for CO_2 and N_2 adsorption isotherms at 298 K. The residual mean square error (RMSE) is given as measure of fit accuracy.

Sample	CO_2 fit parameters				N_2 fit parameters			
	Q_{max}	k	t	RMSE	Q_{max}	k	t	RMSE
Pristine Fibers	3.828	25.281	0.340	0.00117	1.090	0.280	1.000	0.00971
KOH:Fiber 1:4	7.531	31.003	0.265	0.00126	1.471	0.258	0.878	0.00116
KOH:Fiber 2:4	10.000	3.057	0.368	0.01232	3.000	0.143	0.688	0.00422
KOH:Fiber 3:4	10.000	1.663	0.499	0.04986	3.000	0.143	0.926	0.00177

All fit parameters are listed in Table 8.1. Q_{max} increases with high KOH:Fiber ratio, which reflects the increase of CO_2 adsorption capacity of the pure component isotherms. Moreover, the affinity constant k decreases at higher KOH:Fiber weight ratios, which could be related to the wider micropores on these materials and thus lower adsorption potentials for CO_2. The heterogeneity factor t rises slightly, which indicates a more heterogeneous surface due to the higher degree of activation.

Overall, the CO_2 isotherm fits have small residual mean square error (RMSE) values, which increase at higher KOH:Fiber weight ratios. This increase is caused by the transition towards a more linear shape at high KOH:Fiber weight ratios of 2:4 and 3:4 at pressures close to 1 bar, which is less good described by the Toth isotherm. The RMSE values for the N_2 adsorption isotherms show very good accuracy of the fits to the experimental data. The parameters fit well to the trends, showing an increased Q_{max} at ascending KOH:Fiber weight ratio, whereas t remains fairly constant and k slightly decreases. In total, the agreement of the isotherm fits to the experimental data allows a use for IAST selectivity calculations (Figure 8.2).

The fits were used to calculate the selectivity of CO_2 over N_2 for binary mixture of 10 % CO_2 in 90 % N_2 at pressures from 0 to 1 bar. All IAST calculations were conducted using the python package pyGaps 4.5.0 [129].

Figure 8.3 depicts the CO_2 over N_2 selectivity for all samples. The highest CO_2 selectivity values were achieved for carbon nanofibers activated at a KOH:Fiber weight ratio of 1:4 and the pristine carbon nanofibers. At 50 mbar selectivity values of 166 and 140 were calculated, which decrease constantly at increasing pressure approaching values of 101 and 92 at 1 bar. These are very high IAST values for pristine carbon nanofibers and especially for KOH activated carbon nanofibers. Frequently reported IAST values for carbon based materials range from 10 to 40 [165, 166]. The selectivity values on

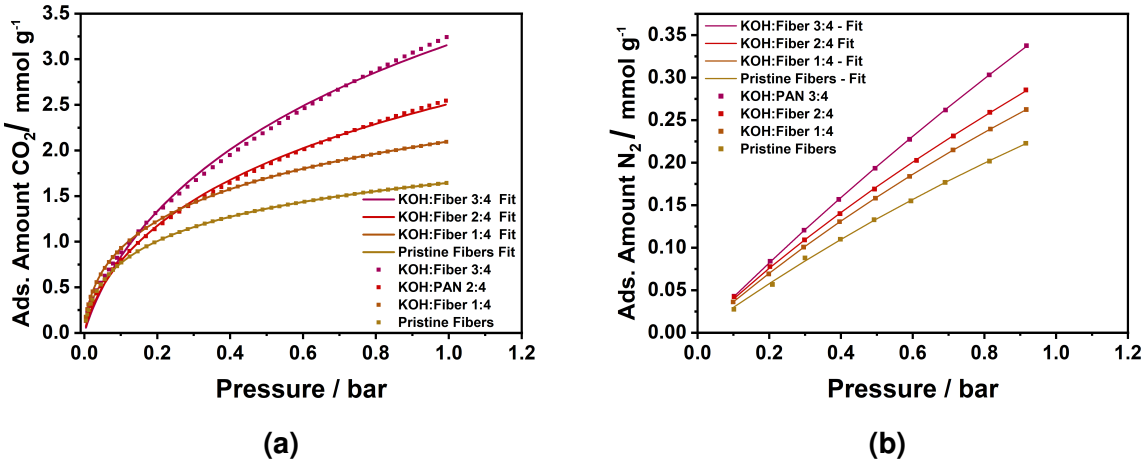


Figure 8.2. – Toth fits for CO_2 (a) and N_2 (b) isotherms measured at 298 K for the samples activated at KOH:Fiber weight ratios of 1:4, 2:4 and 3:4 as well as pristine carbon nanofibers.

carbon nanofibers activated at KOH:Fiber weight ratios of 2:4 and 3:4 are significantly reduced compared to the samples activated at lower KOH:Fiber weight ratios. The CO_2 selectivity at 50 mbar is 52 on carbon nanofibers activated at a KOH:Fiber 2:4 weight ratio and at 34 for samples activated at a KOH:Fiber weight ratio of 3:4. In contrast to the previous two samples, the descent of the selectivity at ascending pressure is almost negligible resulting in selectivity values of 42 and 30 at 1 bar. These values are comparable to the typically obtained IAST selectivity values on activated carbons [48, 165, 166].

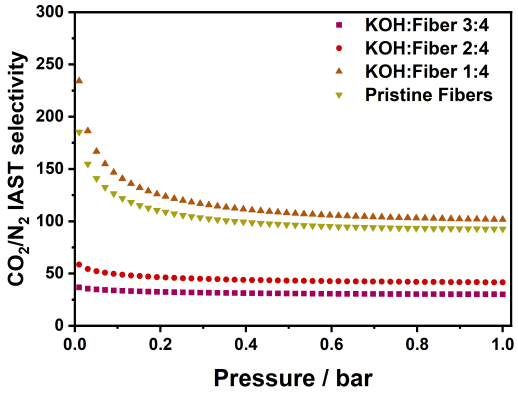


Figure 8.3. – CO_2/N_2 IAST selectivity calculations for KOH:Fiber ratios of 1:4 to 3:4 and the pristine carbon nanofibers for a mixture of 10 % CO_2 in 90 % N_2 at 298 K.

The distinct decrease of selectivity at higher KOH:Fiber weight ratios is assigned to the changed pore size distribution. At the pristine carbon nanofibers and the sample

activated at a KOH:Fiber weight ratio of 1:4, the narrow pore size distribution with a high ultramicropore volume is beneficial for a high CO_2 selectivity. Narrow ultramicropores favor size exclusion effects based on the critical diameter of CO_2 (280 pm) and N_2 (300 pm). However, as the difference in critical diameter is small, additional parameters, such as differences in condensability or chemical interactions, might have significant effects as well [47]. For samples activated at higher KOH:Fiber weight ratios the pore size distribution broadens significantly and wider ultramicropores to supermicropores are formed. These pores are accessible for CO_2 and N_2 in a similar manner. Thus, the competitive adsorption of CO_2 and N_2 is increased, resulting a reduction of the CO_2 selectivity.
All in all, the IAST selectivities are promising for an application in a separation process. Especially, the pristine and slightly KOH-activated carbon nanofibers show excellent values, whereas at higher KOH:Fiber weight ratios the selectivities are only moderate but still sufficient in comparison to reference materials [48, 165, 166].

8.3. Determination of experimental CO_2/N_2 selectivity

As discussed in subsection 2.4.5, IAST calculations rely on several assumptions and idealizations. Therefore, deviations from IAST compared to experimentally determined selectivity values are expected. To assess the differences between IAST calculations and experimental data, breakthrough experiments were conducted. In the breakthrough experiments a column filled with the carbon nanofiber adsorbents was purged with a mixture of 10 % CO_2 in 90 % N_2 diluted in the carrier gas He. At the column outlet the concentration of each component was analyzed by mass spectrometry. A detailed description of the experimental setup and parameters is given in subsection 4.3.8.
All CO_2 breakthrough curves were normalized to the inlet concentration C_0 and are depicted in Figure 8.4a. The earliest breakthrough onset occurs after 40 s on the pristine carbon nanofibers. On KOH-activated samples the breakthrough starts significantly later and the onset shifts with higher KOH:Fiber ratios. At carbon nanofibers activated at a KOH:Fiber weight ratio of 1:4 the breakthrough onset is after 2 min. Subsequently, the breaktrough onset rises to 3 min 15 s on carbon nanofibers activated at a KOH:Fiber weight ratio of 2:4 and 3 min 30 s for the highest KOH:Fiber weight ratio 3:4. The delayed breakthrough onset is attributed to the increased adsorption capacity at higher KOH activation due to the increased pore volume. Thus, the saturation time of the adsorbent is prolonged, resulting in a delayed CO_2 breakthrough.

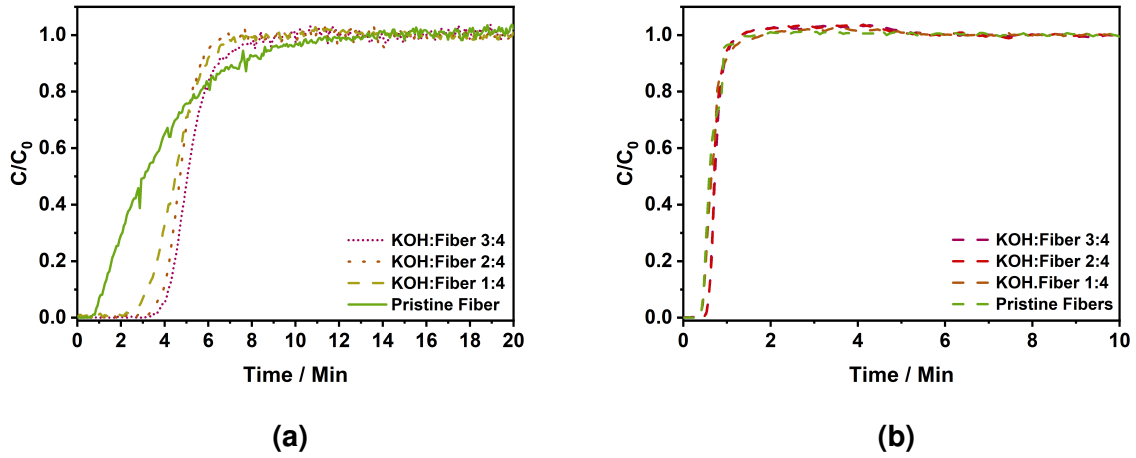


Figure 8.4. – CO_2 (a) and N_2 (b) breakthrough curves for pristine and activated carbon nanofibers at KOH:Fiber weight ratios of 1:4, 2:4 and 3:4 in a 10 % CO_2 in 90 % N_2 gas mixture at 1 bar adsorptive pressure and 298 K. Helium was used as non-adsorbing carrier gas. All breakthrough curves are normalized to the inlet concentration C_0.

For carbon nanofibers activated at KOH:Fiber weight ratios of 1:4; 2:4 and 3:4 focused CO_2 breakthrough curves are obtained, whereas the breakthrough on pristine nanofibers is dispersive [167]. Such a dispersive breakthrough indicates a kinetic limitation at the adsorbent, possibly caused by the narrow pore size present on the pristine fibers. Additionally, short-circuit currents of the adsorptive through the adorber column could be a potential cause. Such short-circuit currents might occur, if the adsorber column is not ideally packed and the adsorptive could pass partially through the column on a direct path without perturbation of the adsorbent. Due to the small sample amount (0.4 g), a narrow adsorber column was used to reduce the dead volume, however this resulted in a non-ideal column:adsorbent diameter ratio, which could result in insufficient packing. Such an insufficient packing could be overcome by the use of larger sample amounts. Previous works of Selmert et al. showed significantly less dispersive breakthrough curves for pristine carbon nanofibers using a sample amount of 1.5 g [110]. Therefore, additional measurements at higher sample amounts are desirable, but could not be carried out within the frame of the present work.

The N_2 breakthrough curves show focused shapes for all carbon nanofiber samples (Figure 8.4b). Independently of the KOH:Fiber weight ratio, the breakthrough occurs at 20 to 40 s. The earlier breakthrough compared to the CO_2 is assigned to the higher fraction of N_2 in the gas composition and the comparably low adsorption capacity of the adsorbents for N_2.

The adsorbed amounts of CO_2 and N_2 were determined by integration of the area between the sample and a blank run. Subsequently, the CO_2 over N_2 selectivity is calculated using Equation 8.2 (see subsection 4.3.8).

$$S_{CO_2} = \frac{n_{CO_2} \cdot p_{N_2}}{n_{N_2} \cdot p_{CO_2}} \tag{8.2}$$

S_{CO_2} Selectivity of CO_2 over N_2
n_{CO_2} Adsorbed amount of CO_2
n_{N_2} Adsorbed amount of N_2
p_{CO_2} Partial pressure of CO_2
p_{N_2} Partial pressure of N_2

A selectivity of 53 was determined at 1 bar in a work of Selmert et al. for pristine carbon nanofibers [110]. Compared to this, carbon nanofibers activated at a KOH:Fiber weight ratio of 1:4 show a similar selectivity of 61. However, carbon nanofibers activated at KOH:Fiber weight ratios of 2:4 and 3:4 show decreased selectivities of 39 and 32. As discussed in section 8.2 this decrease is assigned to an increased pore volume and a broader pore size distribution at high KOH:Fiber weight ratios. Both result in an increased number of adsorption sites, which are accessible for both adsorptives, leading to a decrease in CO_2 selectivity (Figure 8.5a).
For each selectivity the standard deviation is given based on a fivefold determination. A reduction of the standard deviation at higher KOH:Fiber weight ratios is observed, which is likely related to a more accurate assessment of the adsorbed amounts of N_2 on these samples due to an increased N_2 capacity. On pristine nanofibers and carbon nanofibers activated at a KOH:Fiber weight ratio of 1:4 only very small amounts of N_2 are adsorbed, which are hard to assess accurately by integration of the area between blank and sample run. Thus, a higher standard deviation is obtained.
Compared to reference materials, the KOH-activated carbon nanofibers show good adsorption selectivities. However, some reference carbons show higher CO_2 selectivities, but many of these offer low adsorption capacities in return (Figure 8.5b). Thus, the investigated KOH-activated carbon nanofibers are seen as an interesting trade-off between a high capacity and still a good selectivity.

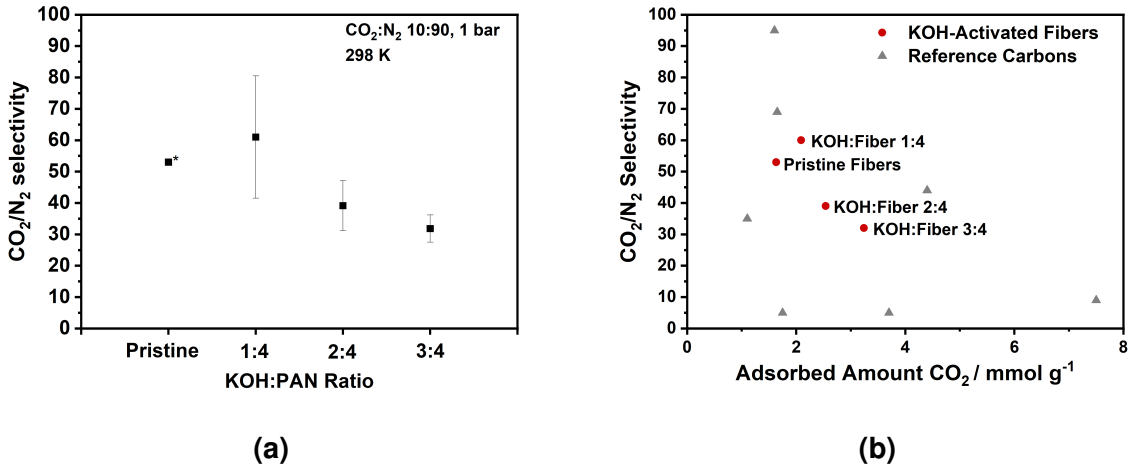


Figure 8.5. – (a) Experimental CO_2/N_2 selectivity values on carbon nanofibers activated at KOH:Fiber weight ratios of 1:4, 2:4 and 3:4 as well as pristine carbon nanofibers for a 90:10 CO_2/N_2 mixture (1 bar adsorptive pressure, 298 K). The selectivities were determined by integration of the area between blank and sample run of the breakthrough curves. (b) Comparison of the CO_2:N_2 selectivity of the carbon nanofibers synthesized in the present work to carbonaceous reference materials [110, 168–170]

8.4. Discussion of CO_2/N_2 selectivities determined by IAST and breakthrough experiments

Calculations based on IAST are commonly used to assess the selectivity of materials in gas separation processes. However, since it relies on several assumptions, a deviation between IAST selectivity and the selectivity determined in breakthrough experiments is probable. Therefore, the CO_2 selectivity values based on IAST calculations and breakthrough experiments are compared in this section.

In general, a decreasing CO_2 selectivity on carbon nanofibers activated at higher KOH:Fiber weight ratios is observed in both evaluations (Figure 8.6). For carbon nanofibers activated at KOH:Fiber weight ratios of 2:4 and 3:4, experimental and IAST selectivity match very well. However, deviations between IAST and experimental selectivity are present at carbon nanofibers activated at KOH:Fiber weight ratios of 1:4 and on pristine carbon nanofibers. For instance, the IAST selectivity on pristine carbon nanofibers is at 92, whilst the experimentally determined selectivity was at 53. Such deviations are frequently discussed in literature [106, 171, 172] and assigned to the strong extrapolation of one adsorption isotherms beyond the measured data to obtain equal spreading pressures for both adsorptives . This is especially the case, if one component adsorbs highly preferentially over the other, as observed for the investigated carbon nanofibers. To identify and assess the potential error caused by extrapolation,

Table 8.2. – Spreading pressure π used for calculation of the IAST selectivity values and the corresponding pressures P_{CO_2} and P_{N_2} of the pure component isotherms of CO_2 and N_2 at 298 K.

Sample	π	P_{CO_2}	P_{N_2}
	J m^{-2}	bar	bar
Pristine Fibers	1.47	0.11	10.17
KOH:Fiber 1:4	1.83	0.11	11.07
KOH:Fiber 2:4	1.28	0.12	5.06
KOH:Fiber 3:4	1.28	0.13	3.91

the spreading pressure and the corresponding needed pressure for both isotherms was calculated (Table 8.2).

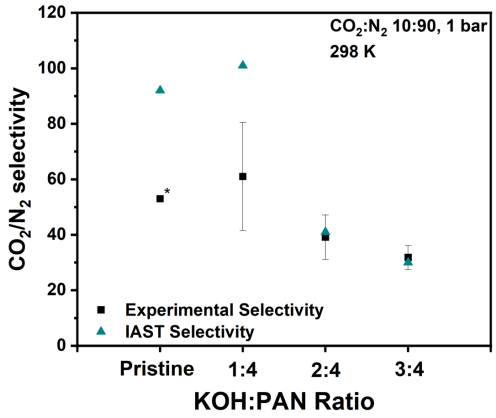


Figure 8.6. – CO_2/N_2 IAST selectivities at carbon nanofibers activated at KOH:Fiber weight ratios of 1:4, 2:4 and 3:4 as well as pristine carbon nanofibers. obtained in a 90:10 CO_2/N_2 mixture at 1 bar and 298 K.

A spreading pressure of 1.47 J m^{-2} for the pristine carbon nanofibers and spreading pressures of 1.83, 1.28 and 1.28 J m^{-2} for carbon nanofibers activated at KOH:Fiber weight ratios of 1:4, 2:4 and 3:4 were determined. The corresponding CO_2 absolute pressures P_{CO_2} lie between 0.11 to 0.13 bar, which is fully covered by the static gas adsorption isotherms. Thus, no extrapolation of the CO_2 isotherms is needed. However, a contrary situation is obtained for the corresponding N_2 pressures P_{N_2}. The N_2 pressures were at 10.17, 11.07, 5.06 and 3.91 bar, which results in a strong extrapolation of the data beyond the experimental data of the static gas adsorption experiments. The highest extrapolation is necessary for the N_2 isotherm of the pristine carbon nanofibers and the carbon nanofibers activated at a KOH:Fiber weight ratio of 1:4, since they show the lowest N_2 adsorption and flattest isotherm slope. For carbon nanofibers activated at KOH:Fiber weight ratios of 2:4 and 3:4, a less strong extrapolation is required, since higher amounts of N_2 are adsorbed on these samples. These results support the

assumption that the strong deviation of IAST selectivity to experimental selectivity is caused by the strong extrapolation of the pure component isotherms.

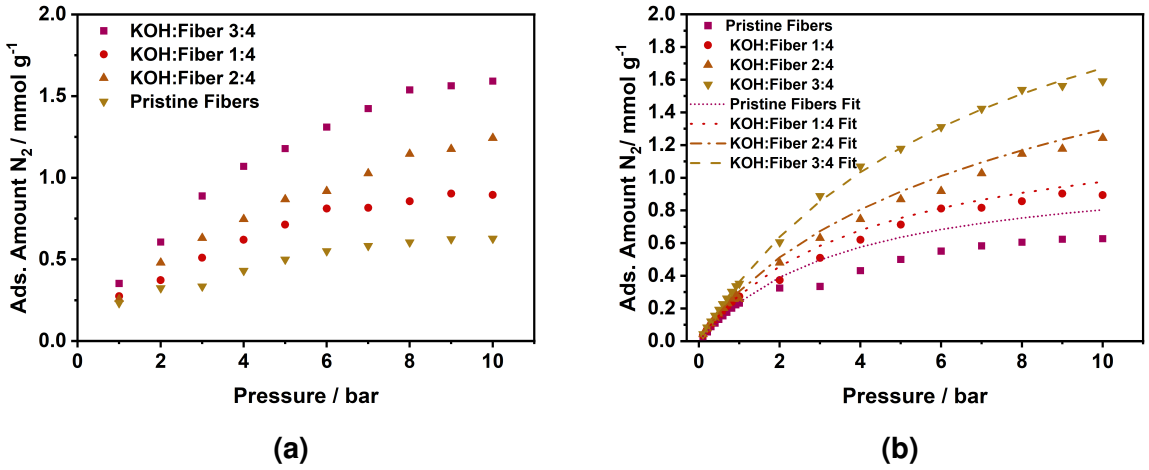


Figure 8.7. – (a) High pressure N_2 adsorption isotherms (10 bar) for pristine and carbon nanofibers activated at KOH:Fiber weight ratios of 1:4, 2:4 and 3:4. (b) Combination of static adsorption isotherms and high pressure isotherms. Correlation of isotherm fit based on the static gas adsorption isotherms to the experimental high pressure isotherms.

To proof this hypothesis, N_2 adsorption isotherms up to 10 bar were measured in dynamic sorption experiments (Figure 8.7a) and compared to the static gas adsorption data and the calculated Toth isotherm fit (Figure 8.7b). The pristine carbon nanofibers adsorbed the lowest amount N_2 at 10 bar (0.63 mmol g^{-1}). Carbon nanofibers activated at a KOH:Fiber weight ratio of 1:4 reach a capacity of 0.89 mmol g^{-1} and for samples activated at KOH:Fiber weight ratios of 2:4 and 3:4 the N_2 capacity increases to 1.24 and 1.59 mmol g^{-1}, respectively.

In Figure 8.7b a combination of experimental N_2 high pressure adsorption isotherms and the static gas adsorption isotherm up to 1 bar is depicted. Additionally, the Toth fits based on the static isotherms are shown to assess the accuracy to the high pressure isotherms. For carbon nanofibers activated at KOH:Fiber weight ratios of 1:4, 2:4 and 3:4 the fits match well the experimental data. However, an overestimation of the fit compared to the experimental isotherm is visible for the pristine carbon nanofibers at high pressures. This underlines the need for experimental selectivity determination to confirm IAST calculations. Nonetheless, as the fit is overestimating the N_2 uptake at high pressures instead of underestimating, the fits do not serve as explanation for the deviations in experimental and calculated selectivity.

Thus, the deviation is likely attributed to assumptions of the IAST. As mentioned in subsection 2.4.5, IAST assumes adsorption sites which are equally accessible for all

adsorbates, which does not describe the present carbon nanofibers well. As stated in works of Kretzschmar et al., the pristine carbon nanofibers show heterogeneous surfaces with molecular sieving properties [47, 120]. Thus, the deviation of experimental and IAST values is the highest on the pristine carbon nanofibers and decreases at higher KOH:Fiber weight ratios used during KOH activation. The stronger activation causes a widening of the pores, which lowers the molecular sieving properties of the KOH-activated carbon nanofibers, resulting in a higher number of accessible adsorption sites for both adsorptives.
Overall, the comparison of IAST and experimental determination of the selectivity clearly showed the drawbacks of IAST. Its assumptions do not describe heterogeneous materials, especially microporous carbons with molecular sieving properties, well. Therefore, breakthrough experiments for determination of the selectivity are essential to avoid overestimation of the selectivity.

8.5. Working capacity and cycle stability of the adsorbents

As already mentioned in the previous section 8.4, the capacity is another important characteristic of an adsorbent. Previously, the capacity of an adsorbent was discussed using the pure component isotherm data at a given measurement temperature. However, this does not reflect the actual capacity of an adsorbent in a separation process, since it is affected by many parameters, such as adsorptive pressure, mixture composition and desorption conditions. The capacity of an adsorbent in a separation process, the so-called working capacity, can be determined by adsorption-desorption cycle experiments. In an idealized separation process, neglecting any mixture effects, assuming complete desorption of the amount adsorbed, the working capacity would equal the isotherm capacity at the respective pressure. This is illustrated in Figure 8.8a for 10 % CO_2 in 90 % N_2 gas composition at a total adsorptive pressures of 1 bar and 10 bar, which corresponds to CO_2 partial pressures of 100 mbar and 1 bar.
At a total pressure of 1 bar, the ideal working capacities of the investigated adsorbents are roughly equal at 0.8 mmol g^{-1}. To benefit from the increased adsorption capacities of the KOH-activated carbon nanofibers compared to the pristine material, the adsorption step needs to be shifted to higher adsorption pressures. For instance, at a total pressure of 10 bar the ideal working capacities of the adsorbents vary strongly depending on the activation ratio. The pristine carbon nanofibers show an ideal capacity of just 1.64 mmol g^{-1}, whereas carbon nanofibers activated at a KOH:Fiber weight ratio

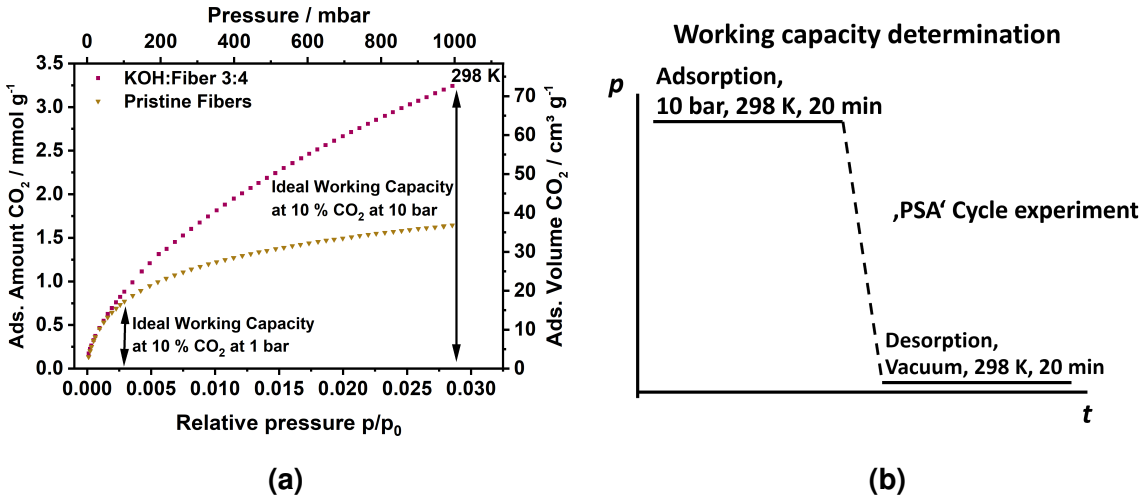


Figure 8.8. – (a) Illustration of the ideal working capacity of an adsorbent at adsorptive pressures of 1 and 10 bar. (b) Scheme of a simplified pressure swing adsorption cycle at 10 bar for a CO_2:N_2 10:90 composition. The adsorption step is conducted at 298 K and 10 bar for 20 min. Afterwards the desorption step at vacuum and 298 K is applied for 20 min.

of 3:4 have ideal working capacity of 3.24 mmol g^{-1}. This underlines the potential of KOH-activated carbon nanofibers for CO_2 separation at increased pressures, e.g. in the adsorption step of a pressure swing adsorption cycle.

To assess the working capacity of the adsorbents experimentally, an idealized pressure swing adsorption cycle experiment was conducted. The adsorption cycle was conducted at 10 bar for 20 min, followed by a desorption cycle for 20 min at fine vacuum conditions (Figure 8.8b). The breakthrough curves were normalized to the inlet concentration C_0 and are shown in Figure 8.9a. The earliest breakthrough starts at 1 min and 40 s on the pristine carbon nanofibers, shortly afterwards the breakthrough can be observed for carbon nanofibers activated at a KOH:Fiber ratio of 1:4. Both show moderately steep, slightly dispersive breakthroughs, which are completed within 10 min. The early breakthroughs as well as the almost simultaneous breakthrough onsets agree well to the previously discussed static isotherms. A delay of the breakthrough onset is visible for carbon nanofibers activated at KOH:Fiber weight ratios of 2:4, starting at 3 min 30 s, which is even more pronounced at on carbon nanofibers at an KOH:Fiber ratio of 3:4 (4 min 20 s). The delay of the breakthrough with increased activation ratios match well the expectations based on the static isotherms. Both adsorbents show increased adsorption capacities due to the higher degree of activation. Thus, the saturation of the adsorbent during the breakthrough experiment takes longer, resulting in the delay of the column breakthrough.

Interestingly, the breakthrough curves show focused shapes independent of the adsorbent. A strongly dispersive shape, as observed for the pristine carbon nanofibers during breakthrough experiments at 1 bar, is not observed at 10 bar. This might be attributed to the increased pressure, which neutralizes kinetic limitations on the pristine carbon nanofibers.

By integration of the area between the sample run and a blank run the working capacity during the idealized pressure swing cycle experiments was determined (Figure 8.9b). The lowest working capacity is obtained on the pristine nanofibers, which show a capacity of 1.1 mmol g^{-1}. An increase of the working capacity is observed at carbon nanofibers at a KOH:Fiber weight ratio of 1:4 and 2:4 reaching capacities of 1.3 and 1.5 mmol g^{-1}. Carbon fibers activated at a KOH:Fiber weight ratio of 3:4 show an additional rise of the working capacity to 2.2 mmol g^{-1}.

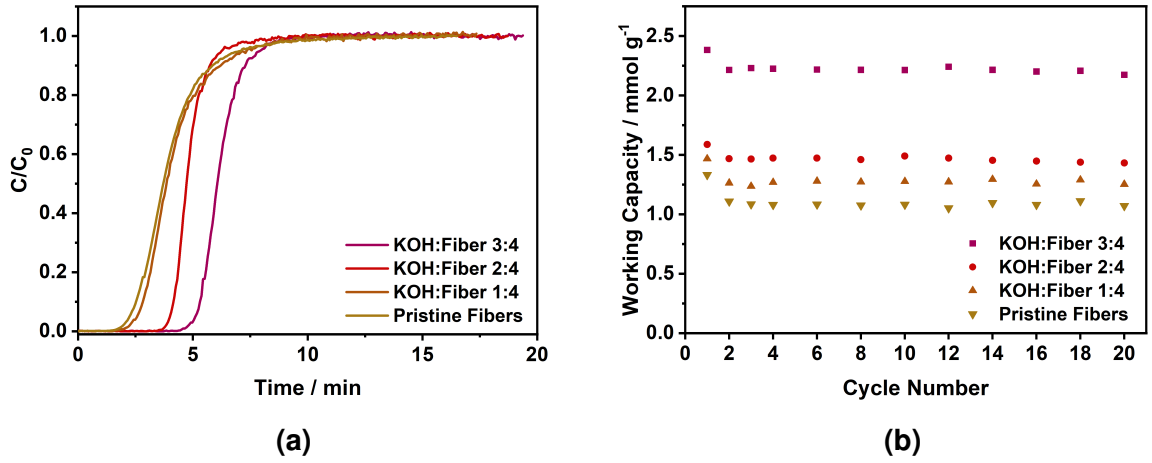


Figure 8.9. – (a) CO_2 breakthrough curves at 10 bar in a 10:90 CO_2/N_2 mixture at 25 °C. As adsorbents pristine and KOH-activated carbon nanofibers were used. KOH activation was applied at different KOH:Fiber weight ratios of 1:4, 2:4 and 3:4. (b) Working capacities and cycle stability of the investigated adsorbents in an idealized pressure swing adsorption cycle experiment. A total of 20 adsorption and desorption cycles was performed.

In general, the determined working capacities match well to the static isotherms and the breakthrough curves. However, the working capacities are reduced compared to the ideal values due to competing N_2 adsorption. The reduced CO_2 selectivity for carbon nanofibers activated at KOH:Fiber weight ratios of 2:4 and 3:4 corresponds well to the larger deviation between pure component isotherm capacity and the assessed working capacity on these samples.

Between the first and the second adsorption cycle a step in the working capacities is observed on all samples. This is attributed to a small CO_2 fraction, which is not removed during the desorption cycle. Besides this, the working capacity remains fairly constant

over the range of 20 cycles, which indicates a good stability of the adsorbent. Previously, Selmert et al. performed even longer cycle stability tests reaching 300 cycles on pristine carbon nanofibers, which showed a excellent long term stability of the adsorbents. However, in the present work such long term runs were omitted, since the idealized setup neglects effects of adsorbent contamination and degradation in a real flue gas composition. Thus, its significance under industrial relevant conditions would be limited. Overall, the increased working capacities during an adsorption step at elevated pressures, outline the advantage of the KOH-activated adsorbents. However, as the selectivities decrease, there is a trade-off between high capacity and high selectivity. Nevertheless, the KOH activation offers interesting opportunities for the tailoring of CO_2 adsorbents for adsorption cycles at elevated pressures.

9. Conclusion

Carbon nanofibers based on polyacrylonitrile (PAN) are a promising material for many gas separation applications. Their synthesis includes the steps of electrospinning, thermal stabilization, carbonization and optional activation. After previous works focused on the carbonization temperature, the present thesis investigated the impact of thermal stabilization and KOH activation on the pore structure, the CO_2 adsorption capacities and the CO_2 over N_2 selectivity.
The thermal stabilization parameters, duration, temperature and atmosphere, were thoroughly investigated and their influence on the chemical structure, pore size distribution and CO_2 adsorption capacities were analyzed. Regarding the KOH activation process, different post-treatment conditions at two oxygen flows subsequent to KOH activation were investigated. Moreover, a series of KOH-activated carbon nanofiber pellets was analyzed in breakthrough experiments of a binary gas mixture of CO_2 in N_2. Particular attention was spent on separation process relevant parameters, such as CO_2 over N_2 selectivity, working capacity and cycle stability of the adsorbent.

An essential influence of the thermal stabilization parameters on the pore structure and CO_2 adsorption properties of the carbon nanofibers was found. By extending the stabilization duration, the pore volume as well as the CO_2 adsorption capacities improved significantly. Compared to 0.5 h stabilization duration, the CO_2 adsorption capacity at 1 bar doubled for carbon nanofibers stabilized for 15 h and the linear isotherm turned into a type I isotherm. Similar effects were obtained by variation of the stabilization temperature, where a rise of the stabilization temperature from 200 to 300 °C resulted in a ninefold increased CO_2 adsorption capacity at 1 bar. Both, the extended stabilization duration or a higher stabilization temperature resulted in an increased cumulative pore volume. These changes were attributed to a higher progress of stabilized ladder polymer formation and a higher incorporation of oxygen into the structure, which affects the pore formation during carbonization.
The essential impact of the oxygen incorporation during thermal stabilization on the pore structure of the carbon nanofibers was identified in a study varying the stabilization

atmosphere between N_2 and air. An approximately 50 % increased cumulative pore volume was determined on carbon nanofibers stabilized in air compared to stabilization in N_2. The oxygen incorporation was especially important for the formation of the ultramicropore volume during carbonization, which is seen as essential for high CO_2 adsorption capacities and selectivity.

Commonly, post-treatment conditions after KOH activation are not controlled and the activated carbon is simply exposed to ambient air. However, since air-sensitive potassium is formed during activation, an uncontrolled exposure might alter the activated carbon structure. By application of different oxygen concentrations and flow rates as post-treatment conditions, potential effects were studied. At high oxygen availability vigorous potassium oxidation reactions followed by a partial carbon combustion were observed. These reactions strongly alter the pore structure of the carbon nanofibers. Control of these reactions was achieved by applying a low oxygen flow, which resulted in a slow potassium oxidation and insufficient heat release to start a carbon combustion reaction. The control of the post-treatment conditions and inhibition of the carbon combustion reactions resulted in a 35 % increase in pore volume of the carbon nanofibers. This results in a rise of the CO_2 adsorption capacity at 1 bar to 6.5 mmol g^{-1} instead of 4.7 mmol g^{-1} without controlled post-treatment.

The post-treatment strategy was used to synthesize a series of KOH-activated carbon nanofibers, which were activated at KOH:Fiber weight ratios of 1:4 to 3:4. At increased KOH:Fiber weight ratios a high increase in micropore volume was achieved, reaching a four times increased cumulative pore volume at a KOH:Fiber weight ratio of 3:4 compared to the pristine nanofibers. The ideal adsorbed solution theory (IAST) was used to calculate the CO_2 selectivity of the carbon nanofibers in a binary mixture of 10 % CO_2 in N_2, which matches typical CO_2 concentrations in flue gas. At 1 bar adsorptive pressure promising CO_2 over N_2 selectivity values of 94 (KOH:Fiber wt.-ratio 1:4), which decreased to 52 (KOH:Fiber wt.-ratio 2:4) and 34 (KOH:Fiber wt.-ratio 3:4) were determined. This decrease was attributed to the broadening of the pore size distribution resulting in more accessible adsorption sites for both adsorptives.

For verification of the IAST selectivities, the KOH-activated carbon nanofibers were investigated in breakthrough experiments. The highest experimental selectivities were determined at 53 and 61 on pristine carbon nanofibers and samples activated at a KOH:Fiber weight ratio of 1:4, respectively. At higher KOH:Fiber weight ratios a decline

of the selectivity to 39 and 32 was observed. In principal, IAST and experimental selectivity values show similar trends. However, especially for pristine carbon nanofibers and carbon nanofibers activated at a KOH:Fiber weight ratio of 1:4 a significant overestimation was obtained in IAST calculations. These were assigned to deviations of the adsorbent from the assumptions underlying IAST, which points out the necessity for an experimental determination of the selectivity of these adsorbents.
Besides the CO_2 selectivity, parameters like the working capacity and the cycle stability were analyzed. To do so, the performance of the adsorbents was investigated in a simplified vacuum pressure swing adsorption cycle at a total pressure of 10 bar during the adsorption step. Carbon nanofibers activated at KOH:Fiber weight ratios of 3:4 offered the highest working capacity of 2.2 $mmol\,g^{-1}$, which is doubled the working capacity of the pristine nanofibers. All adsorbents showed a good cycle stability over the investigated cycle number. In total, the KOH-activated carbon nanofiber pellets are a trade-off between a high selectivity and a high capacity, but especially for adsorption processes at high adsorptive pressure they offer good adsorption performance.

Summarizing, this thesis provides in-depth results on the importance of thermal stabilization on the development of the pore structure during carbonization of PAN-based carbon nanofibers. The choice of thermal stabilization conditions, especially the availability of oxygen, highly affects the pore formation and thus the CO_2 adsorption properties of the carbon nanofibers. Furthermore, a control of the post-treatment conditions after KOH activation was identified as essential to preserve the pore structure after the activation step. Doing so, the oxidation of elemental potassium is slowed down and a carbon combustion reaction is inhibited. KOH-activated adsorbents synthesized under controlled post-treatment, showed high CO_2 working capacities, good CO_2 over N_2 selectivity as well as good cycle stability. Overall, the gathered results supplement the earlier works focused on the impact of the carbonization temperature and contribute to a holistic understanding of the impact of the different process steps in carbon nanofiber synthesis on the pore structure and corresponding gas adsorption properties.

Bibliography

[1] L. Hoesung et al. *Climate Change 2023: Synthesis Report. Contribution of Working Groups I, II and III to the Sixth Assessment Report of the Intergovernmental Panel on Climate Change, IPCC, Geneva, Switzerland*. 2023. DOI: 10.59327/IPCC/AR6-9789291691647.

[2] M. Crippa et al. "CO2 emissions of all world countries - JRC/IEA/PBL 2022 Report". In: (2022). DOI: 10.2760/730164.

[3] Q. Wang, ed. *Post-combustion Carbon Dioxide Capture Materials*. 2nd ed. The Royal Society of Chemistry, 2019.

[4] N. J. Azhari et al. "Methanol synthesis from CO2: A mechanistic overview". In: *Results in Engineering* 16 (2022), p. 100711. ISSN: 25901230. DOI: 10.1016/j.rineng.2022.100711.

[5] T. Biswal et al. "Conversion of carbon dioxide to methanol: A comprehensive review". In: *Chemosphere* 298 (2022), p. 134299. DOI: 10.1016/j.chemosphere.2022.134299.

[6] C. G. Okoye-Chine et al. "Conversion of carbon dioxide into fuels—A review". In: *Journal of CO2 Utilization* 62 (2022), p. 102099. ISSN: 22129820. DOI: 10.1016/j.jcou.2022.102099.

[7] E. S. Sanz-Perez et al. "Direct Capture of CO2 from Ambient Air". In: *Chem Rev* 116.19 (2016), pp. 11840–11876. ISSN: 1520-6890 (Electronic) 0009-2665 (Linking). DOI: 10.1021/acs.chemrev.6b00173.

[8] Z. Dai and L. Deng. "Membranes for CO2 capture and separation: Progress in research and development for industrial applications". In: *Separation and Purification Technology* 335 (2024), p. 126022. ISSN: 13835866. DOI: 10.1016/j.seppur.2023.126022.

[9] M. Herout et al. "Biogas composition depending on the type of plant biomass used". In: *Research in Agricultural Engineering* 57.4 (2011), pp. 137–143. ISSN: 12129151. DOI: 10.17221/41/2010-RAE.

[10] Y. Li et al. “Composition and Toxicity of Biogas Produced from Different Feedstocks in California”. In: *Environmental Science & Technology* 53.19 (2019), pp. 11569–11579. ISSN: 0013-936X. DOI: 10.1021/acs.est.9b03003.

[11] A. Bosoaga, O. Masek, and J. E. Oakey. “CO2 Capture Technologies for Cement Industry”. In: *Energy Procedia* 1.1 (2009), pp. 133–140. ISSN: 18766102. DOI: 10.1016/j.egypro.2009.01.020.

[12] M. Bui et al. “Carbon capture and storage (CCS): the way forward”. In: *Energy & Environmental Science* 11.5 (2018), pp. 1062–1176. ISSN: 1754-5692. DOI: 10.1039/C7EE02342A.

[13] H. Chu et al. “Integration of carbon emission reduction policies and technologies: Research progress on carbon capture, utilization and storage technologies”. In: *Separation and Purification Technology* 343 (2024), p. 127153. ISSN: 13835866. DOI: 10.1016/j.seppur.2024.127153.

[14] C. A. Grande. “Advances in Pressure Swing Adsorption for Gas Separation”. In: *ISRN Chemical Engineering* 2012 (2012), pp. 1–13. DOI: 10.5402/2012/982934.

[15] M. Kong et al. “A review on development of post-combustion CO2 capture technologies: Performance of carbon-based, zeolites and MOFs adsorbents”. In: *Fuel* 371 (2024), p. 132103. DOI: 10.1016/j.fuel.2024.132103.

[16] A. Das et al. “Advancements in adsorption based carbon dioxide capture technologies-A comprehensive review”. In: *Heliyon* 9.12 (2023), e22341. ISSN: 2405-8440. DOI: 10.1016/j.heliyon.2023.e22341.

[17] Z. Hu et al. “CO 2 Capture in Metal–Organic Framework Adsorbents: An Engineering Perspective”. In: *Advanced Sustainable Systems* 3.1 (2019). ISSN: 2366-7486 2366-7486. DOI: 10.1002/adsu.201800080.

[18] Y. Liu, Z. U. Wang, and H.-C. Zhou. “Recent advances in carbon dioxide capture with metal-organic frameworks”. In: *Greenhouse Gases: Science and Technology* 2.4 (2012), pp. 239–259. ISSN: 21523878. DOI: 10.1002/ghg.1296.

[19] P. Nugent et al. “Porous materials with optimal adsorption thermodynamics and kinetics for CO2 separation”. In: *Nature* 495.7439 (2013), pp. 80–84. DOI: 10.1038/nature11893.

[20] Z. Xiang, S. Leng, and D. Cao. “Functional Group Modification of Metal–Organic Frameworks for CO 2 Capture”. In: *The Journal of Physical Chemistry C* 116.19 (2012), pp. 10573–10579. ISSN: 1932-7447. DOI: 10.1021/jp3018875.

[21] B. Zheng et al. “Expanded porous MOF-505 analogue exhibiting large hydrogen storage capacity and selective carbon dioxide adsorption”. In: *Inorganic chemistry* 52.6 (2013), pp. 2823–2829. DOI: 10.1021/ic301598n.

[22] P. M. Bhatt et al. “A Fine-Tuned Fluorinated MOF Addresses the Needs for Trace CO2 Removal and Air Capture Using Physisorption”. In: *Journal of the American Chemical Society* 138.29 (2016), pp. 9301–9307. DOI: 10.1021/jacs.6b05345.

[23] F. Su and C. Lu. “CO2 capture from gas stream by zeolite 13X using a dual-column temperature/vacuum swing adsorption”. In: *Energy & Environmental Science* 5.10 (2012), p. 9021. ISSN: 1754-5692. DOI: 10.1039/c2ee22647b.

[24] D. Ko, R. Siriwardane, and L. T. Biegler. “Optimization of a Pressure-Swing Adsorption Process Using Zeolite 13X for CO 2 Sequestration”. In: *Industrial & Engineering Chemistry Research* 42.2 (2003), pp. 339–348. ISSN: 0888-5885. DOI: 10.1021/ie0204540.

[25] M. R. Hudson et al. “Unconventional, highly selective CO2 adsorption in zeolite SSZ-13”. In: *Journal of the American Chemical Society* 134.4 (2012), pp. 1970–1973. DOI: 10.1021/ja210580b.

[26] M. M. Lozinska et al. “Understanding carbon dioxide adsorption on univalent cation forms of the flexible zeolite Rho at conditions relevant to carbon capture from flue gases”. In: *Journal of the American Chemical Society* 134.42 (2012), pp. 17628–17642. DOI: 10.1021/ja3070864.

[27] D. Saha et al. “Adsorption of CO2, CH4, N2O, and N2 on MOF-5, MOF-177, and zeolite 5A”. In: *Environmental science & technology* 44.5 (2010), pp. 1820–1826. ISSN: 0013-936X. DOI: 10.1021/es9032309.

[28] X. Xu et al. “Novel Polyethylenimine-Modified Mesoporous Molecular Sieve of MCM-41 Type as High-Capacity Adsorbent for CO 2 Capture”. In: *Energy & Fuels* 16.6 (2002), pp. 1463–1469. ISSN: 0887-0624. DOI: 10.1021/ef020058u.

[29] A. H. Lu and Dai. S., eds. *Porous materials for carbon dioxide*. Springer Verlag, 2014.

[30] M. S. Shafeeyan et al. “A review on surface modification of activated carbon for carbon dioxide adsorption”. In: *Journal of Analytical and Applied Pyrolysis* 89.2 (2010), pp. 143–151. ISSN: 01652370. DOI: 10.1016/j.jaap.2010.07.006.

[31] H. Zhao et al. “Carbon-based adsorbents for post-combustion capture: a review”. In: *Greenhouse Gases: Science and Technology* 8.1 (2018), pp. 11–36. ISSN: 21523878. DOI: 10.1002/ghg.1758.

[32] X.-Q. Zhang, W.-C. Li, and A.-H. Lu. “Designed porous carbon materials for efficient CO2 adsorption and separation”. In: *New Carbon Materials* 30.6 (2015), pp. 481–501. ISSN: 18725805. DOI: 10.1016/s1872-5805(15)60203-7.

[33] N. A. Rashidi and S. Yusup. “An overview of activated carbons utilization for the post-combustion carbon dioxide capture”. In: *Journal of CO2 Utilization* 13 (2016), pp. 1–16. ISSN: 22129820. DOI: 10.1016/j.jcou.2015.11.002.

[34] K. Sumida et al. “Carbon dioxide capture in metal-organic frameworks”. In: *Chemical reviews* 112.2 (2012), pp. 724–781. DOI: 10.1021/cr2003272.

[35] Y. Liu et al. “Pentaethylenehexamine loaded SBA-16 for CO 2 capture from simulated flue gas”. In: *Powder Technology* 318 (2017), pp. 186–192. ISSN: 00325910. DOI: 10.1016/j.powtec.2017.06.002.

[36] P. Sharma et al. “Amine modified and pelletized mesoporous materials: Synthesis, textural–mechanical characterization and application in adsorptive separation of carbondioxide”. In: *Powder Technology* 219 (2012), pp. 86–98. ISSN: 00325910. DOI: 10.1016/j.powtec.2011.12.023.

[37] J. Zhou, X. Wang, and W. Xing. “Carbon-based CO2 adsorbents”. In: *Post-combustion Carbon Dioxide Capture Materials*. Ed. by Q. Wang. The Royal Society of Chemistry, 2019, pp. 1–75. DOI: 10.1039/9781788013352-00001.

[38] D. A. Khuong, H. N. Nguyen, and T. Tsubota. “Activated carbon produced from bamboo and solid residue by CO2 activation utilized as CO2 adsorbents”. In: *Biomass and Bioenergy* 148 (2021), p. 106039. ISSN: 09619534. DOI: 10.1016/j.biombioe.2021.106039.

[39] H. Wei et al. “Granular bamboo-derived activated carbon for high CO(2) adsorption: the dominant role of narrow micropores”. In: *ChemSusChem* 5.12 (2012), pp. 2354–2360. ISSN: 1864-564X (Electronic) 1864-5631 (Linking). DOI: 10.1002/cssc.201200570.

[40] J. Yang et al. “Efficient CO 2 Capture by Porous Carbons Derived from Coconut Shell”. In: *Energy & Fuels* 31.4 (2017), pp. 4287–4293. ISSN: 0887-0624. DOI: 10.1021/acs.energyfuels.7b00633.

[41] A. S. Ello et al. “Coconut shell-based microporous carbons for CO2 capture”. In: *Microporous and Mesoporous Materials* 180 (2013), pp. 280–283. ISSN: 13871811. DOI: 10.1016/j.micromeso.2013.07.008.

[42] J. Kaźmierczak, P. Nowicki, and R. Pietrzak. “Sorption properties of activated carbons obtained from corn cobs by chemical and physical activation”. In: *Adsorption* 19.2-4 (2013), pp. 273–281. ISSN: 0929-5607 1572-8757. DOI: 10.1007/s10450-012-9450-y.

[43] M. Zhong et al. “Copolymer-templated nitrogen-enriched porous nanocarbons for CO2 capture”. In: *Chemical communications (Cambridge, England)* 48.94 (2012), pp. 11516–11518. DOI: 10.1039/c2cc36652e.

[44] Q. Wang., ed. *Post-combustion Carbon Dioxide Capture Materials: Chapter 1-Carbon-based CO2 Adsorbents*. DOI: 10.1039/9781788011099-00001.

[45] S.-Y. Lee and S.-J. Park. “A review on solid adsorbents for carbon dioxide capture”. In: *Journal of Industrial and Engineering Chemistry* 23 (2015), pp. 1–11. ISSN: 1226086X. DOI: 10.1016/j.jiec.2014.09.001.

[46] B. Petrovic, M. Gorbounov, and S. Masoudi Soltani. “Influence of surface modification on selective CO2 adsorption: A technical review on mechanisms and methods”. In: *Microporous and Mesoporous Materials* 312 (2021), pp. 1–41. ISSN: 13871811. DOI: 10.1016/j.micromeso.2020.110751.

[47] A. Kretzschmar et al. “Application of a tailorable carbon molecular sieve to evaluate concepts for the molecular dimensions of gases”. In: *Microporous and Mesoporous Materials* 343 (2022), pp. 1–9. ISSN: 13871811. DOI: 10.1016/j.micromeso.2022.112156.

[48] M. Oschatz and M. Antonietti. “A search for selectivity to enable CO2 capture with porous adsorbents”. In: *Energy & Environmental Science* 11.1 (2018), pp. 57–70. ISSN: 1754-5692 1754-5706. DOI: 10.1039/c7ee02110k.

[49] M. T. Ho, G. W. Allinson, and D. E. Wiley. “Reducing the Cost of CO 2 Capture from Flue Gases Using Pressure Swing Adsorption”. In: *Industrial & Engineering Chemistry Research* 47.14 (2008), pp. 4883–4890. ISSN: 0888-5885. DOI: 10.1021/ie070831e.

[50] M. S. A. Rahaman, A. F. Ismail, and A. Mustafa. “A review of heat treatment on polyacrylonitrile fiber”. In: *Polymer Degradation and Stability* 92.8 (2007), pp. 1421–1432. ISSN: 01413910. DOI: 10.1016/j.polymdegradstab.2007.03.023.

[51] H. Khayyam et al. “PAN precursor fabrication, applications and thermal stabilization process in carbon fiber production: Experimental and mathematical modelling”. In: *Progress in Materials Science* 107 (2020), pp. 1–39. ISSN: 00796425. DOI: 10.1016/j.pmatsci.2019.100575.

[52] J. Wang et al. “Fungi-based porous carbons for CO2 adsorption and separation”. In: *Journal of Materials Chemistry* 22.28 (2012), pp. 13911–13913. ISSN: 0959-9428 1364-5501. DOI: 10.1039/c2jm32139d.

[53] P. P. Tsai, H. Schreuder-Gibson, and P. Gibson. “Different electrostatic methods for making electret filters”. In: *Journal of Electrostatics* 54 (2002), pp. 333–341. DOI: 10.1016/S0304-3886(01)00160-7.

[54] P. Gibson, H. Schreuder-Gibson, and D. Rivin. “Transport properties of porous membranes based on electrospun nanofibers”. In: *Colloids and Surfaces A: Physicochemical and Engineering Aspects* (2001), pp. 469–481. ISSN: 09277757.

[55] S. Md. Islam et al. “A review on fabrication of nanofibers via electrospinning and their applications”. In: *SN Applied Sciences* 1.10 (2019). ISSN: 2523-3963. DOI: 10.1007/s42452-019-1288-4.

[56] A. Greiner and J. H. Wendorff. “Electrospinning: a fascinating method for the preparation of ultrathin fibers”. In: *Angewandte Chemie (International ed. in English)* 46.30 (2007), pp. 5670–5703. ISSN: 1433-7851. DOI: 10.1002/anie.200604646.

[57] Z. Dong, S. J. Kennedy, and Y. Wu. “Electrospinning materials for energy-related applications and devices”. In: *Journal of Power Sources* 196.11 (2011), pp. 4886–4904. ISSN: 03787753. DOI: 10.1016/j.jpowsour.2011.01.090.

[58] D. Li and Y. Xia. “Electrospinning of Nanofibers: Reinventing the Wheel?” In: *Advanced Materials* 16.14 (2004), pp. 1151–1170. ISSN: 0935-9648 1521-4095. DOI: 10.1002/adma.200400719.

[59] Ya Li et al. “Developments of Advanced Electrospinning Techniques: A Critical Review”. In: *Advanced Materials Technologies* 6.11 (2021). ISSN: 2365-709X 2365-709X. DOI: 10.1002/admt.202100410.

[60] L. M. Manocha and O. P. Bahl. “Role of oxygen during thermal stabilisation of PAN fibres”. In: *Fibre Science and Technology* 13 (1980), pp. 199–212. DOI: 10.1016/0015-0568(80)90004-4.

[61] R. C. Houtz. “"Orlon" Acrylic Fiber: Chemistry and Properties”. In: *Textile Research Journal* 20.11 (1950), pp. 786–801. DOI: 10.1177/004051755002001107.

[62] P. J. Goodhew, A. J. Clarke, and J. E. Bailey. “A Review of the farbication and properties of carbon fibers”. In: *Materials Science and Engineering* 17 (1975), pp. 3–30. URL: https://doi.org/10.1016/0025-5416(75)90026-9.

[63] Z. Bashir. “A Critical Review of the Stabilisation of Polyacrylonitrile”. In: *Carbon* 29.8 (1991), pp. 1081–1190. ISSN: 00086223. DOI: 10.1016/0008-6223(91)90024-D.

[64] S. Damodaran, P. Desai, and A. S. Abhiraman. “Chemical and Physical Aspects of the Formation of Carbon Fibres from PAN-based Precursors”. In: *The Journal of The Textile Institute* 81.4 (2008), pp. 384–420. ISSN: 0040-5000 1754-2340. DOI: 10.1080/00405009008658719.

[65] A. J. Clarke and J. E. Bailey. “Oxidation of acrylic fibres for carbon fibre formation”. In: *Nature* 243 (1973), pp. 146–150. DOI: 10.1038/243146a0.

[66] K. Morita et al. “Characterization of commercially available PAN (Polyacrylonitrile)-based carbon fibers”. In: *Pure and Applied Chemistry* 58.3 (1986), pp. 455–468. ISSN: 1365-3075 0033-4545.

[67] Mittal J. et al. “IR Studies of PAN Fibres Thermally Stabilized at Elevated Temperatures”. In: *Carbon* 32.6 (1994), pp. 1133–1136. ISSN: 00086223.

[68] T. Takahagi et al. “XPS studies on the chemical structure of the stabilized polyacrylonitrile fiber in the carbon fiber production process”. In: *Journal of Polymer Science Part A: Polymer Chemistry* 24 (1986), pp. 3101–3107. ISSN: 0887-624X 1099-0518. DOI: 10.1002/pola.1986.080241134.

[69] S. Arbab et al. “The essential conditions for developing high electrical conductivity capability in carbon nanofibers”. In: *IOP Conference Series: Materials Science and Engineering* 460 (2018), p. 012019. ISSN: 1757-8981. DOI: 10.1088/1757-899X/460/1/012019.

[70] Z. Du et al. “Electrospinning organic solvent resistant preoxidized poly(acrylonitrile) nanofiber membrane and its properties”. In: *Chinese Journal of Chemical Engineering* 53 (2023), pp. 289–299. ISSN: 10049541. DOI: 10.1016/j.cjche.2022.01.030.

[71] S. Arbab et al. “Optimum stabilization processing parameters for polyacrylonitrile-based carbon nanofibers and their difference with carbon (micro) fibers”. In: *Polymer Degradation and Stability* 142 (2017), pp. 198–208. ISSN: 01413910. DOI: 10.1016/j.polymdegradstab.2017.06.026.

[72] E. Maruccia et al. “Effect of Thermal Stabilization on PAN-Derived Electrospun Carbon Nanofibers for CO(2) Capture”. In: *Polymers (Basel)* 13.23 (2021), pp. 1–13. ISSN: 2073-4360 (Electronic) 2073-4360 (Linking). DOI: 10.3390/polym13234197.

[73] R. Ojeda-López et al. “Improve in CO2 and CH4 Adsorption Capacity on Carbon Microfibers Synthesized by Electrospinning of PAN”. In: *Fibers* 7.10 (2019), pp. 1–14. ISSN: 2079-6439. DOI: 10.3390/fib7100081.

[74] Watt, W. Green, J. “The pyrolysis of polyacrylonitrile”. In: 1971.

[75] W. Watt and B. Perov, ed. *Strong Fibers*. 1985.

[76] J. Park et al. “Structural Study of Polyacrylonitrile-Based Carbon Nanofibers for Understanding Gas Adsorption”. In: *ACS Appl Mater Interfaces* 13.39 (2021), pp. 46665–46670. ISSN: 1944-8252 (Electronic) 1944-8244 (Linking). DOI: 10.1021/acsami.1c13541.

[77] K. Kaneko and F. Rodriguez-Reinoso. *Nanoporous Materials for Gas Storage*. Springer, 2019. DOI: 10.1007/978-981-13-3504-4.

[78] H. Marsh and F. Rodriguez-Reinoso. *Activated Carbon*. Elsevier, 2006. DOI: 10.1016/B978-0-08-044463-5.X5013-4.

[79] W. Shen et al. “Hierarchical porous polyacrylonitrile-based activated carbon fibers for CO2 capture”. In: *Journal of Materials Chemistry* 21.36 (2011), pp. 14036–14040. ISSN: 0959-9428 1364-5501. DOI: 10.1039/c1jm12585k.

[80] U. Kamran, J. R. Choi, and S. J. Park. “A Role of Activators for Efficient CO2 Affinity on Polyacrylonitrile-Based Porous Carbon Materials”. In: *Front Chem* 8 (2020), pp. 1–18. ISSN: 2296-2646 (Print) 2296-2646 (Linking). DOI: 10.3389/fchem.2020.00710.

[81] M. Wu et al. “Preparation and characterization of porous carbons from PAN-based preoxidized cloth by KOH activation”. In: *Carbon* 42.1 (2004), pp. 205–210. ISSN: 00086223. DOI: 10.1016/j.carbon.2003.10.025.

[82] A. N. Wennerberg and T. M. O’Grady. “Active Carbon process and composition: US Patent”. 4082694.

[83] J. Wang and S. Kaskel. “KOH activation of carbon-based materials for energy storage”. In: *Journal of Materials Chemistry* 22 (2012), pp. 23710–23725. ISSN: 0959-9428 1364-5501. DOI: 10.1039/C2JM34066F.

[84] N. E. Williams, O. A. Oba, and N. P. Aydinlik. “Modification, Production, and Methods of KOH–Activated Carbon”. In: *ChemBioEng Reviews* 9.2 (2022), pp. 164–189. ISSN: 2196-9744 2196-9744. DOI: 10.1002/cben.202100030.

[85] Otowa, T. Tanibata, R. and M. Itoh. “Production and adsorption characteristics of MAXSORB: high surface-area active carbon”. In: *Gas Separation & Purification* 7 (1993), pp. 241–245. DOI: 10.1016/0950-4214(93)80024-Q.

[86] T. Otowa. “Activation mechanism, surface properties and adsorption characteristics of KOH activated high surface area carbon”. In: *Fundamentals of Adsorption* (1996), pp. 709–716. DOI: 10.1007/978-1-4613-1375-5{\textunderscore}88.

[87] E. Raymundo-Piñero et al. “KOH and NaOH activation mechanisms of multiwalled carbon nanotubes with different structural organisation”. In: *Carbon* 43.4 (2005), pp. 786–795. ISSN: 00086223. DOI: 10.1016/j.carbon.2004.11.005.

[88] T. Fischer et al. “Post-treatment strategies for pyrophoric KOH-activated carbon nanofibres”. In: *RSC Advances* 14.6 (2024), pp. 3845–3856. ISSN: 2046-2069. DOI: 10.1039/d3ra07096d.

[89] J. Wang, Y. K. Park, and Y. M. Jo. “Sequential improvement of activated carbon fiber properties for enhanced removal efficiency of indoor CO2”. In: *Journal of Industrial and Engineering Chemistry* 89 (2020), pp. 400–408. ISSN: 1226086X. DOI: 10.1016/j.jiec.2020.06.011.

[90] Ljubisa R. Radovic, ed. *Chemistry and Physics of Carbon*. CRC Press Taylor and Francis Group, 2008.

[91] K.S.W. Sing et al. “Reporting Physisoprtion data for gas/solid systems with special Reference to the Determination of Surface Area and Porosity”. In: *Pure and Applied Chemistry* 57.4 (1985), pp. 603–619. ISSN: 1365-3075 0033-4545.

[92] S. Lowell et al. *Characterization of porous solids and powders: surface area, pore size and density*. Kluwer Academic Publishers, 2010.

[93] Matthias Thommes et al. “Physisorption of gases, with special reference to the evaluation of surface area and pore size distribution (IUPAC Technical Report)”. In: *Pure and Applied Chemistry* 87.9-10 (2015), pp. 1051–1069. ISSN: 1365-3075 0033-4545. DOI: 10.1515/pac-2014-1117.

[94] M. A. Al-Ghouti and D. A. Da’ana. “Guidelines for the use and interpretation of adsorption isotherm models: A review”. In: *Journal of hazardous materials* 393 (2020), p. 122383. DOI: 10.1016/j.jhazmat.2020.122383.

[95] J. Wang and X. Guo. “Adsorption isotherm models: Classification, physical meaning, application and solving method”. In: *Chemosphere* 258 (2020), p. 127279. DOI: 10.1016/j.chemosphere.2020.127279.

[96] N. Ayawei, A. N. Ebelegi, and D. Wankasi. “Modelling and Interpretation of Adsorption Isotherms”. In: *Journal of Chemistry* 2017 (2017), pp. 1–11. ISSN: 2090-9063. DOI: 10.1155/2017/3039817.

[97] S. Brunauer, P. H. Emmet, and E. Teller. “Adsorption of Gases in Multimolecular Layers”. In: *J. Am. Chem. Soc.* 60 (1938), pp. 309–319. DOI: 10.1021/ja01269a023.

[98] J. Tóth. “Uniform interpretation of Gas/solid adsorption”. In: *Advances in Colloid and Interface Science* 55 (1995), pp. 1–239. DOI: 10.1016/0001-8686(94)00226-3.

[99] I. Langmuir. “The adsorption of gases on plane surfaces of glass, mica and platinum”. In: *Journal of the American Chemical Society* 40.9 (1918), pp. 1361–1403. DOI: 10.1021/ja02242a004.

[100] J. Rouquerol, P. Llewellyn, and F. Rouquerol. “Is the BET equation applicable to microporous adsorbents?” In: *Studies in Surface Science and Caralysis* 160 (2007), pp. 49–56. DOI: 10.1016/S0167-2991(07)80008-5.

[101] F. Rouquerol, J. Rouquerol, and K. Sing, eds. *Adsorption by Powders and Porous Solids: Principles, Methodology and Applications*. Academic Press, 1999.

[102] J. Landers, G. Y.. Gor, and A. V. Neimark. “Density functional theory methods for characterization of porous materials”. In: *Colloids and Surfaces A: Physicochemical and Engineering Aspects* 437 (2013), pp. 3–32. ISSN: 09277757. DOI: 10.1016/j.colsurfa.2013.01.007.

[103] K. S. Walton and D. S. Sholl. “Predicting multicomponent adsorption: 50 years of the ideal adsorbed solution theory”. In: *AIChE Journal* 61.9 (2015), pp. 2757–2762. ISSN: 0001-1541 1547-5905. DOI: 10.1002/aic.14878.

[104] A. L. Myers. “Thermodynamics of Adsorption in Porous Materials”. In: ().

[105] A. L. Myers and J. M. Prausnitz. “Thermodynamics of mixed–gas adsorption”. In: *AIChE Journal* 11.1 (1965), pp. 121–127. ISSN: 0001-1541 1547-5905. DOI: 10.1002/aic.690110125.

[106] P. Billemont et al. “IAST predictions vs co-adsorption measurements for CO2 capture and separation on MIL-100 (Fe)”. In: *Adsorption* 23.2-3 (2016), pp. 225–237. ISSN: 0929-5607 1572-8757. DOI: 10.1007/s10450-016-9825-6.

[107] A. Nuhnen and C. Janiak. “A practical guide to calculate the isosteric heat/enthalpy of adsorption via adsorption isotherms in metal-organic frameworks, MOFs”. In: *Dalton Trans* 49.30 (2020), pp. 10295–10307. ISSN: 1477-9234 (Electronic) 1477-9226 (Linking). DOI: 10.1039/d0dt01784a.

[108] Pan H., J. A. Ritter, and P. B. Balbuena. “Examination of the approximations used in determining the isosteric het of adsorption from the Clausius-Clapeyron equation”. In: *Langmuir* 14 (1998), pp. 6323–6327. ISSN: 1520-5827 (Electronic) 0743-7463 (Linking). DOI: 10.1021/la9803373.

[109] T. Fischer. “Optimization of CO2 adsorption selectivity and capacity of electrospun PAN-based carbon nanofibers”. Masterarbeit. Aachen: RWTH, 2020.

[110] V. Selmert et al. “CO2/N2 separation on highly selective carbon nanofibers investigated by dynamic gas adsorption”. In: *ChemSusChem* 15 (2022), pp. 1–12. ISSN: 1864-564X (Electronic) 1864-5631 (Linking). DOI: 10.1002/cssc.202200761.

[111] 3P Instruments GmbH. *mixSorb L, mixSorb S, mixSorb SHP, mixSorb Manager: Dynamic Sorption Analyzer Operating Manual*. Ed. by 3P Instruments GmbH. Oedelzhausen, 2020.

[112] N. S. Wilkins, A. Rajendran, and S. Farooq. “Dynamic column breakthrough experiments for measurement of adsorption equilibrium and kinetics”. In: *Adsorption* 27.3 (2020), pp. 397–422. ISSN: 0929-5607 1572-8757. DOI: 10.1007/s10450-020-00269-6.

[113] S. N. Arshad, M. Naraghi, and I. Chasiotis. “Strong carbon nanofibers from electrospun polyacrylonitrile”. In: *Carbon* 49.5 (2011), pp. 1710–1719. ISSN: 00086223. DOI: 10.1016/j.carbon.2010.12.056.

[114] J. Borowec et al. “Carbonization-Temperature-Dependent Electrical Properties of Carbon Nanofibers-From Nanoscale to Macroscale”. In: *Adv Mater* 35.31 (2023), e2300936. ISSN: 1521-4095 (Electronic) 0935-9648 (Linking). DOI: 10.1002/adma.202300936.

[115] Y. Aykut, B. Pourdeyhimi, and S. A. Khan. “Effects of surfactants on the microstructures of electrospun polyacrylonitrile nanofibers and their carbonized analogs”. In: *Journal of Applied Polymer Science* 130.5 (2013), pp. 3726–3735. ISSN: 0021-8995 1097-4628. DOI: 10.1002/app.39637.

[116] S.-H. Yoon et al. “KOH activation of carbon nanofibers”. In: *Carbon* 42.8-9 (2004), pp. 1723–1729. ISSN: 00086223. DOI: 10.1016/j.carbon.2004.03.006.

[117] R. Schierholz et al. “The carbonization of polyacrylonitrile-derived electrospun carbon nanofibers studied by in situ transmission electron microscopy”. In: *RSC Advances* 9.11 (2019), pp. 6267–6277. ISSN: 2046-2069. DOI: 10.1039/c8ra10491c.

[118] Y. C. Chiang, W. T. Chin, and C. C. Huang. “The Application of Hollow Carbon Nanofibers Prepared by Electrospinning to Carbon Dioxide Capture”. In: *Polymers (Basel)* 13.19 (2021), pp. 1–17. ISSN: 2073-4360 (Electronic) 2073-4360 (Linking). DOI: 10.3390/polym13193275.

[119] D. Yadav, F. Amini, and A. Ehrmann. “Recent advances in carbon nanofibers and their applications – A review”. In: *European Polymer Journal* 138 (2020), p. 109963. DOI: 10.1016/j.eurpolymj.2020.109963.

[120] A. Kretzschmar et al. “Tailored Gas Adsorption Properties of Electrospun Carbon Nanofibers for Gas Separation and Storage”. In: *ChemSusChem* 13.12 (2020), pp. 3180–3191. ISSN: 1864-564X (Electronic) 1864-5631 (Linking). DOI: 10.1002/cssc.202000520.

[121] H. Weinrich et al. “Kohlenstofffaser-Formkörper”.

[122] C. Song et al. “Adsorption Studies of Coconut Shell Carbons Prepared by KOH Activation for Removal of Lead(II) From Aqueous Solutions”. In: *Sustainability* 6.1 (2013), pp. 86–98. ISSN: 2071-1050. DOI: 10.3390/su6010086.

[123] G. Hotová and V. Slovák. “Quantitative TG-MS analysis of evolved gases during the thermal decomposition of carbon containing solids”. In: *Thermochimica Acta* 632 (2016), pp. 23–28. DOI: 10.1016/j.tca.2016.03.012.

[124] G. L. Collins, N. W. Thomas, and G. E. Williams. “Kinetic Relationships between heat generation and nitrile consumption in the reaction of poly(acrylonitrile) in air at 265 °C”. In: *Carbon* 26 (1988), pp. 672–679. ISSN: 00086223. DOI: 10.1016/0008-6223(88)90070-X.

[125] L. Chen et al. “Effects of oxygen on the structural evolution of polyacrylonitrile fibers during rapid thermal treatment”. In: *RSC Adv* 10.11 (2020), pp. 6356–6361. ISSN: 2046-2069 (Electronic) 2046-2069 (Linking). DOI: 10.1039/c9ra08881d.

[126] A. Sadezky et al. “Raman microspectroscopy of soot and related carbonaceous materials: Spectral analysis and structural information”. In: *Carbon* 43.8 (2005), pp. 1731–1742. ISSN: 00086223. DOI: 10.1016/j.carbon.2005.02.018.

[127] Z. E. Brubaker et al. “Quantitative analysis of Raman spectral parameters for carbon fibers: practical considerations and connection to mechanical properties”. In: *Journal of Materials Science* 56.27 (2021), pp. 15087–15121. ISSN: 0022-2461 1573-4803. DOI: 10.1007/s10853-021-06225-1.

[128] N. Newville et al. *lmfit/lmfit-py 0.9.14*. 2019. DOI: 10.5281/zenodo.3381550.

[129] P. Iacomi and P. L. Llewellyn. “pyGAPS: a Python-based framework for adsorption isotherm processing and material characterisation”. In: *Adsorption* 25.8 (2019), pp. 1533–1542. ISSN: 0929-5607 1572-8757. DOI: 10.1007/s10450-019-00168-5.

[130] M. Pagel. “Einfluss der thermischen Stabilisierung auf die Gasadsorptionseigenschaften von elektrogesponnenen Kohlenstoffnanofasern”. Masterthesis. Rheinbach: Hochschule Bonn-Rhein-Sieg, 2024.

[131] T. Fischer et al. “The impact of thermal stabilization temperature and duration on the pore structure of polyacrylonitrile-based carbon nanofibers”. In: *Carbon Trends* 21 (2025), p. 100559. ISSN: 26670569. DOI: 10.1016/j.cartre.2025.100559.

[132] H. N. Friedlander et al. “On the chromophore of polyacrylonitrile. VI. Mechanism of Color Formation in Polyacrylonitrile”. In: *Macromolecules* 1.1 (1968), pp. 79–86. ISSN: 0024-9297.

[133] E. Cipriani et al. “Crosslinking and carbonization processes in PAN films and nanofibers”. In: *Polymer Degradation and Stability* 123 (2016), pp. 178–188. ISSN: 01413910.

[134] J. Choi et al. “Evolution of structural inhomogeneity in polyacrylonitrile fibers by oxidative stabilization”. In: *Carbon* 165 (2020), pp. 225–237. ISSN: 00086223. DOI: 10.1016/j.carbon.2020.04.027.

[135] Z. Li et al. “Raman spectroscopy of carbon materials and their composites: Graphene, nanotubes and fibres”. In: *Progress in Materials Science* 135 (2023), pp. 1–58. ISSN: 00796425. DOI: 10.1016/j.pmatsci.2023.101089.

[136] H. Niu, X. Wang, and T. Lin. “Needleless Electrospinning: Developments and Perfomances”. In: *Nanofibers - Production, Properties and Functional Applications*, pp. 17–36. DOI: 10.5772/24999.

[137] E. Fitzer and D. J. Müller. “The influence of oxygen on the chemical reactions during stabilization of PAN as carbon fiber precursor”. In: *Carbon* 13 (1975), pp. 63–69. ISSN: 00086223. DOI: 10.1016/0008-6223(75)90259-6.

[138] Z. Fu et al. “Structure evolution and mechanism of polyacrylonitrile and related copolymers during the stabilization”. In: *Journal of Materials Science* 49.7 (2014), pp. 2864–2874. ISSN: 0022-2461 1573-4803. DOI: 10.1007/s10853-013-7992-3.

[139] S. Xiao et al. “Mechanism and kinetics of oxidation during the thermal stabilization of polyacrylonitrile fibers”. In: *Journal of Applied Polymer Science* 127.4 (2012), pp. 3198–3203. ISSN: 0021-8995 1097-4628. DOI: 10.1002/app.37733.

[140] L. Liu et al. “Water adsorption on carbon - A review”. In: *Adv Colloid Interface Sci* 250 (2017), pp. 64–78. ISSN: 1873-3727 (Electronic) 0001-8686 (Linking). DOI: 10.1016/j.cis.2017.10.002.

[141] X. Liu et al. “Stabilization of Atactic -Polyacrylonitrile under Nitrogen and Air As Studied by Solid-State NMR”. In: *Macromolecules* 48.15 (2015), pp. 5300–5309. ISSN: 0024-9297. DOI: 10.1021/acs.macromol.5b01030.

[142] Y. Wang et al. “Structural Identification of Polyacrylonitrile during Thermal Treatment by Selective 13 C Labeling and Solid-State 13 C NMR Spectroscopy”. In: *Macromolecules* 47.12 (2014), pp. 3901–3908. ISSN: 0024-9297. DOI: 10.1021/ma500727n.

[143] N-G. Vannerberg. “Peroxides, Superoxides, and Ozonides of the Metals of Groups Ia IIa and IIb”. In: *Prog. Inorg. Chem.* 4 (1962), pp. 125–297. DOI: 10.1002/9780470166055.ch3.

[144] Vol’nov I. I. *Peroxides, Superoxides, and Ozonides of Alkali and Alkaline Earth Metals*. New York: Springer, 1966.

[145] K. Fredenhagen and G. Cadenbach. “Die Bindung von Kalium durch Kohlenstoff”. In: *Zeitschrift für anorganische und allgemeine Chemie* 158.1 (1926), pp. 249–263. ISSN: 0044-2313 1521-3749. DOI: 10.1002/zaac.19261580122.

[146] H. Marsh et al. *Chemistry and Physics of Carbon*. Chemistry and Physics of Carbon. Marcel Dekker Inc., 1987. DOI: 10.1201/9781003209034.

[147] Kapteijn F., Jurriaans J., and Moulijn J. A. “Formation of intercalate-like structures by heat treatment of K2CO3-carbon in an inert atmosphere”. In: *Fuel* 62 (1983), pp. 249–251. DOI: 10.1016/0016-2361(83)90210-7.

[148] R. Bovard. “Oxygen Sources for Space Flights”. In: *Aerospace Medicine* (1960), pp. 407–412.

[149] C. B. Jackson and R. C. Werner. “Manufacture and Use of Potassium Superoxide”. In: *Handling and uses of the alkali metals*. Vol. 19. American Chemical Society, 1957, pp. 174–177. DOI: 10.1021/ba-1957-0019.ch019.

[150] J. S. Im et al. “The study of controlling pore size on electrospun carbon nanofibers for hydrogen adsorption”. In: *J Colloid Interface Sci* 318.1 (2008), pp. 42–49. ISSN: 1095-7103 (Electronic) 0021-9797 (Linking). DOI: 10.1016/j.jcis.2007.10.024.

[151] J. Romanos et al. “Nanospace engineering of KOH activated carbon”. In: *Nanotechnology* 23.1 (2012), pp. 1–7. ISSN: 1361-6528 (Electronic) 0957-4484 (Linking). DOI: 10.1088/0957-4484/23/1/015401.

[152] A.-N. A. El-Hendawy. “An insight into the KOH activation mechanism through the production of microporous activated carbon for the removal of Pb2+ cations”. In: *Applied Surface Science* 255.6 (2009), pp. 3723–3730. ISSN: 01694332. DOI: 10.1016/j.apsusc.2008.10.034.

[153] D. Lozano-Castelló et al. “Carbon activation with KOH as explored by temperature programmed techniques, and the effects of hydrogen”. In: *Carbon* 45.13 (2007), pp. 2529–2536. ISSN: 00086223. DOI: 10.1016/j.carbon.2007.08.021.

[154] D. Lozano-Castelló et al. “Preparation of activated carbons from Spanish anthracite. Activation by KOH”. In: *Carbon* 39 (2000), pp. 741–749. ISSN: 00086223. DOI: 10.1016/S0008-6223(00)00185-8.

[155] Yoshizawa N. et al. “XRD evaluation of KOH activation process and influence coal rank”. In: *Fuel* 81 (2002), pp. 1717–1722. DOI: 10.1016/S0016-2361(02)00101-1.

[156] Y.-C. Chiang, C.-Y. Yeh, and C.-H. Weng. “Carbon Dioxide Adsorption on Porous and Functionalized Activated Carbon Fibers”. In: *Applied Sciences* 9.10 (2019), pp. 1–15. ISSN: 2076-3417. DOI: 10.3390/app9101977.

[157] Y. K. Kim, G. M. Kim, and J. W. Lee. “Highly porous N-doped carbons impregnated with sodium for efficient CO2 capture”. In: *Journal of Materials Chemistry A* 3.20 (2015), pp. 10919–10927. ISSN: 2050-7488 2050-7496. DOI: 10.1039/c5ta01776a.

[158] J. Singh, H. Bhunia, and S. Basu. “Adsorption of CO2 on KOH activated carbon adsorbents: Effect of different mass ratios”. In: *Journal of Environmental Management* 250 (2019). DOI: 10.1016/j.jenvman.2019.109457.

[159] G. Zainab et al. “Electrospun carbon nanofibers with multi-aperture/opening porous hierarchical structure for efficient CO(2) adsorption”. In: *J Colloid Interface Sci* 561 (2020), pp. 659–667. ISSN: 1095-7103 (Electronic) 0021-9797 (Linking). DOI: 10.1016/j.jcis.2019.11.041.

[160] D. D. Do, S. Junpirom, and H. D. Do. “A new adsorption–desorption model for water adsorption in activated carbon”. In: *Carbon* 47.6 (2009), pp. 1466–1473. ISSN: 00086223. DOI: 10.1016/j.carbon.2009.01.039.

[161] A. Kretzschmar. “Gasadsorption auf elektrogesponnenen Kohlenstoffnanofasern für Kohlendioxidabscheidung und -nutzung”. PhD thesis. RWTH Aachen University, 2021. DOI: 10.18154/RWTH-2021-11972.

[162] R. H. Bradley. “The adsorption of vapours by activated and heat-treated microporous carbons. Part 2. Assessment of surface polarity using water adsorption”. In: *Carbon* 31.2 (1993), pp. 269–272. ISSN: 00086223.

[163] F. Stoeckli and D. Huguenin. “Water Adsorption in Active Carbon characterized by adsorption and immersion techniques”. In: *J. Chem. Soc. Faraday Trans.* 88.5 (1992), pp. 737–740.

[164] L. Cossarutto et al. “Transport and sorption of water vapour in activated carbons”. In: *Carbon* 39 (2001), pp. 2339–2346. ISSN: 00086223.

[165] J. W. To et al. “Hierarchical N-Doped Carbon as CO2 Adsorbent with High CO2 Selectivity from Rationally Designed Polypyrrole Precursor”. In: *J Am Chem Soc* 138.3 (2016), pp. 1001–1009. ISSN: 1520-5126 (Electronic) 0002-7863 (Linking). DOI: 10.1021/jacs.5b11955.

[166] K. Li et al. “Pine cone shell-based activated carbon used for CO 2 adsorption”. In: *Journal of Materials Chemistry A* 4.14 (2016), pp. 5223–5234. ISSN: 2050-7488. DOI: 10.1039/C5TA09908K.

[167] D. Basmadjian. “Rapid Procedures for the Prediction of Fixed-Bed Adsorber Behavior. 1. Isothermal Sorption of Single Gases with Arbitrary Isotherms and Transport Modes: Principles and Recommended Methods”. In: ().

[168] Y. Zhao et al. “Superior Capture of CO2 Achieved by Introducing Extra-framework Cations into N-doped Microporous Carbon”. In: *Chemistry of Materials* 24.24 (2012), pp. 4725–4734. ISSN: 0897-4756 1520-5002. DOI: 10.1021/cm303072n.

[169] P. Zhang et al. “A new choice of polymer precursor for solvent-free method: Preparation of N-enriched porous carbons for highly selective CO2 capture”. In: *Chemical Engineering Journal* 355 (2019), pp. 963–973. ISSN: 13858947. DOI: 10.1016/j.cej.2018.08.219.

[170] R. B. Rios et al. “Evaluation of carbon dioxide–nitrogen separation through fixed bed measurements and simulations”. In: *Adsorption* 20.8 (2014), pp. 945–957. ISSN: 0929-5607 1572-8757. DOI: 10.1007/s10450-014-9639-3.

[171] F. Gharagheizi and D. S. Sholl. “Comprehensive Assessment of the Accuracy of the Ideal Adsorbed Solution Theory for Predicting Binary Adsorption of Gas Mixtures in Porous Materials”. In: *Industrial & Engineering Chemistry Research* 61.1 (2022), pp. 727–739. ISSN: 0888-5885. DOI: 10.1021/acs.iecr.1c03876.

[172] R. Krishna and J. M. van Baten. “How Reliable Is the Ideal Adsorbed Solution Theory for the Estimation of Mixture Separation Selectivities in Microporous Crystalline Adsorbents?” In: *ACS Omega* 6.23 (2021), pp. 15499–15513. ISSN: 2470-1343 (Electronic) 2470-1343 (Linking). DOI: 10.1021/acsomega.1c02136.

[173] P. Linstrom. *NIST Chemistry WebBook, NIST Standard Reference Database 69*. 1997. DOI: 10.18434/T4D303.

A. Appendix

A.1. ICP-OES

Inductively coupled plasma optical emission spectroscopy (ICP-OES) was performed on an iCAP 7600 analyser (ThermoFisher Scientific, USA). Two parallel digestions of 100 mg sample each were prepared in a furnace with 250 mg lithium borate. The samples were heated to 1050 °C during 3 h and maintained for 30 minutes at this temperature. The obtained melt was diluted in 50 ml 5 % HNO_3 and filled up to 100 ml. The obtained solutions were analyzed in the ICP-OES. The ICP-OES measurements were conducted at the Central Institue of Engineering and Analytics (ZEA-3) of Forschungszentrum Jülich GmbH.

Table A.1. – Determination of the total potassium content of impregnated, low O_2-flow and high O_2-flow carbon nanofibers.

Sample	Potassium content wt.-%	Standard deviation wt.-%
After KOH impregnation	25.2	0.6
Low O_2-flow	26.8	0.7
High O_2-flow	30.4	0.4

A.2. Raman spectra fits

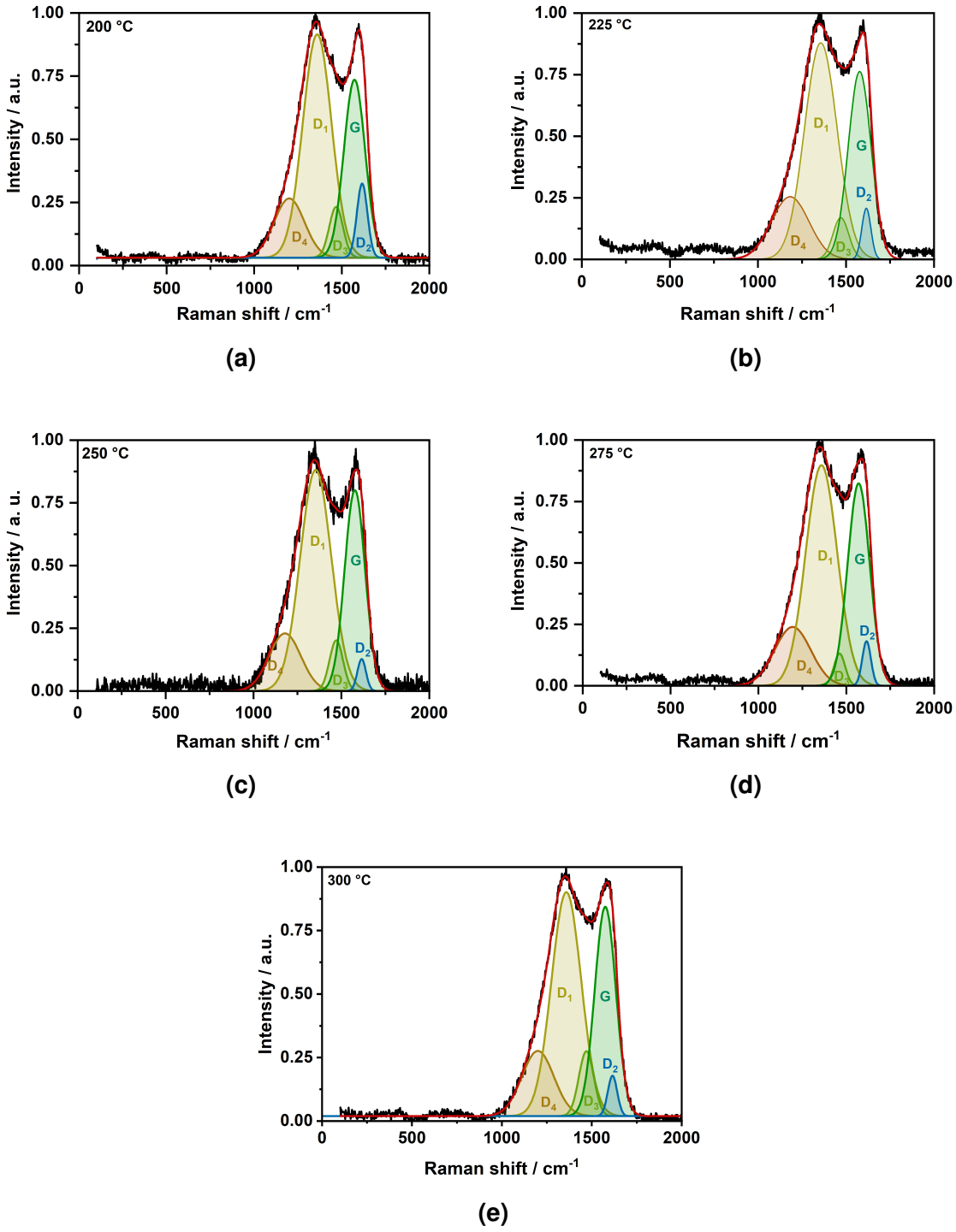


Figure A.1. – Raman spectra of the D and G band region of carbon nanofibers thermally stabilized at temperatures of (a) 200, (b) 225, (c) 250, (d) 275 and (e) 300 °C. The carbonization was conducted for all samples at 800 °C in Ar for 3 h.

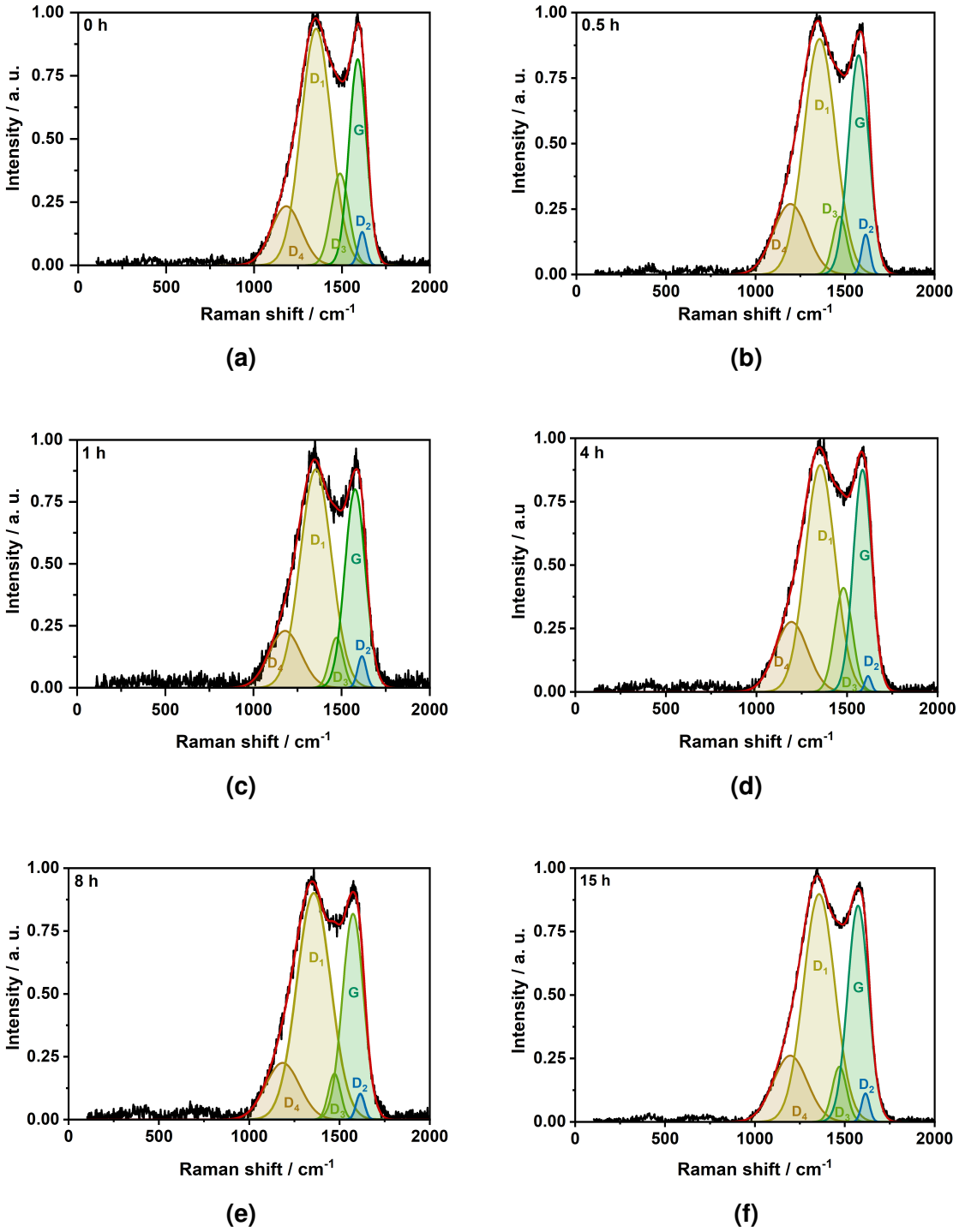


Figure A.2. – Raman spectra of the D and G band region of carbon nanofibers thermally stabilized at durations of (a) 0, (b) 0.5, (c) 1, (d) 4, (e) 8 and (f) 15 h. The carbonization was conducted for all samples at 800 °C in Ar for 3 h.

Table A.2. – Peak position, peak area and full width half mid (FWHM) of the G, D_1, D_2, D_3 and D_4 fits used for analyis of the Raman spectra in section 5.2.

Band	Parameter	0 h	0.5 h	1 h	4 h	8 h	15 h (Air)	15 h (N_2)
G	Position / cm^{-1}	1589	1575	1576	1585	1578	1573	1575
	Area	101	119	117	111	137	124	120
	FWHM	116	133	136	120	137	136	152
D1	Position	1352	1357	1353	1351	1354	1364	1364
	Area	201	199	196	184	212	196	209
	FWHM	201	208	209	193	212	205	219
D2	Position	1615	1615	1615	1615	1615	1615	1615
	Area	8	9	8	3	6	6	16
	FWHM	54	54	57	42	55	52	62
D3	Position	1488	1470	1470	1480	1476	1470	1470
	Area	46	22	19	49	15	22	8
	FWHM	117	92	90	114	79	94	72
D4	Position	1182	1194	1178	1192	1175	1196	1189
	Area	50	64	52	62	53	62	60
	FWHM	201	223	212	210	221	223	241

Table A.3. – Peak position, peak area and full width half mid (FWHM) of the G, D_1, D_2, D_3 and D_4 fits used for analyis of the Raman spectra in section 5.3.

Band	Parameter	200 °C	225 °C	250 °C	275 °C	300 °C
G	Position / cm^{-1}	1572	1570	1573	1570	1574
	Area	106	125	124	129	121
	FWHM	142	152	136	147	138
D1	Position	1359	1350	1357	1358	1358
	Area	181	196	196	201	183
	FWHM	192	218	205	210	195
D2	Position	1616	1610	1615	1615	1615
	Area	22	13	6	11	10
	FWHM	70	60	52	58	61
D3	Position	1467	1474	1470	1461	1469
	Area	19	13	22	10	26
	FWHM	92	105	94	75	97
D4	Position	1200	1190	1196	1194	1200
	Area	50	72	62	62	57
	FWHM	203	250	223	243	210

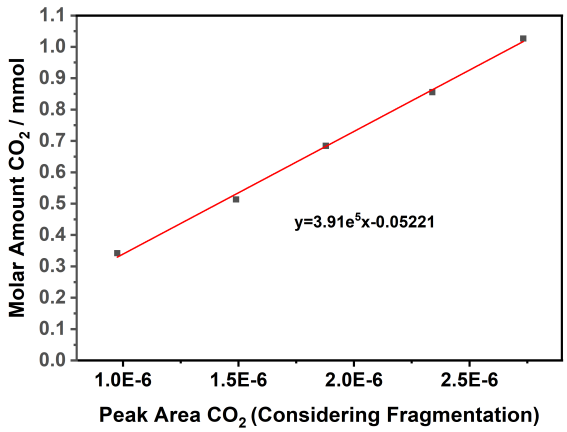
A.3. Calcium oxalate calibration of the mass spectrometer

50, 75, 100, 125 and 150 mg of $CaC_2O_4\,x\,H_2O$ were heated to 1000 °C inside the TGA-MS. The measurement was conducted in MID mode. The the peak area of m/z 44 during the decomposition of formed $CaCO_3$ into CaO and CO_2 was determined. Based on the fragmentation data from the NIST database the total peak area of CO_2 was determined and used as calibration. Occuring chemical reactions, ion fragmentation data and calibration graph are given below.

$$\mathrm{CaC_2O_4\,H_2O} \longleftrightarrow \mathrm{CaC_2CO_4 + H_2O}\ (< 150\,^\circ C) \tag{A.1}$$

$$\mathrm{CaC_2O_4} \longleftrightarrow \mathrm{CaCO_3 + CO}\ (< 500\,^\circ C) \tag{A.2}$$

$$\mathrm{CaCO_3} \longleftrightarrow \mathrm{CaO + CO_2}\ (< 750\,^\circ C) \tag{A.3}$$



(a)

Figure A.3. – Mass spectrometer calibration data obtained from $CaC_2O_4\,x\,H_2O$ calibration. 50, 75, 100, 125 and 150 mg of $CaC_2O_4\,x\,H_2O$ were heated up to 1000 °C inside a TGA-MS device. A relation between the peak area and the molar amount of CO_2 was established.

Table A.4. – Relative intensities of the ion fragmentation of CO_2 in mass sepctrometry for m/z 44, 28, 16 and 12. [173]

Ion Fragmentation CO_2 m/z 44	m/z 28	m/z 16	m/z 12
1	0.098	0.097	0.085

List of Figures

2.1. Process steps in carbon nanofiber synthesis 6
2.2. Scheme of an electrospinning setup 7
2.3. Simplified reaction scheme of the thermal stabilization reaction 8
2.4. Reaction sequences during thermal stabilization in air and N_2 9
2.5. Simplified scheme of the carbonization reactions of PAN 10
2.6. Condensation reactions of oxygen-containing stabilized ladder polymer structures 11
2.7. Process steps in KOH activation 12
2.8. Adsorption potentials depending on the pore size 14
2.9. Classification of adsorption isotherms 16
2.10. Scheme of a volumetric static gas adsorption device 21
2.11. Schematic setup of a dynamic sorption analyzer 22
2.12. Breakthrough curves obtained in dynamic sorption experiments 23
2.13. Evaluation of breakthrough curves - Assessment of the weak component 24

5.1. Color change of stabilized PAN-based nanofibers depending on the stabilization duration 42
5.2. IR investigations of nanofibers stabilized at different stabilization durations 43
5.3. Elemental analysis of carbon nanofibers stabilized at different stabilization durations at 250 °C 45
5.4. Raman spectrum and changes in D_1/G ratio caused by variation of the stabilization duration 46
5.5. SEM images of carbon nanofibers stabilized at different durations 47
5.6. Ar isotherms and cumulative pore size distribution on carbon nanofibers stabilized at different durations 48
5.7. CO_2 isotherms and pore size analysis of carbon nanofibers stabilized at different durations 50
5.8. Color change of stabilized PAN-based nanofibers depending on the stabilization temperature 51

5.9. IR spectra and cyclization index of PAN-based nanofibers stabilized at different stabilization temperatures 52
5.10. Elemental analysis of carbon nanofibers stabilized at different temperatures. 54
5.11. Raman spectra and D/G ratio of carbon nanofibers stabilized at different temperatures 55
5.12. SEM images of carbon nanofibers stabilized at different temperatures . 56
5.13. Ar adsorption isotherms of carbon nanofibers stabilized at different stabilization temperatures 57
5.14. CO_2 isotherms, Monte-Carlo pore size distribution and combined pore size distribution based on DFT and Monte-Carlo calculations 58
5.15. Simultaneous TGA-DSC measurements of PAN-based nanofibers stabilized in air and nitrogen 60
5.16. IR spectra and elemental analysis of stabilized nanofibers in nitrogen and air 61
5.17. Raman spectrum and D/G ratio of carbon nanofibers stabilized in air and nitrogen 63
5.18. Ar isotherms and pore size distribution of carbon nanofibers stabilized in air and N_2 64
5.19. CO_2 adsorption isotherms at 273 K and cumulative pore volume at different atmospheres. 66
5.20. Correlations of cyclization indicators to the pore formation 67

6.1. Scheme of the applied heat treatment for post-treatment investigations . 70
6.2. TGA-DSC experiments at high O_2-flow post-treatment conditions 71
6.3. TGA-DSC experiments at low O_2-flow post-treatment conditions 74
6.4. Emitted CO_2 during high and low O_2-flow post-treatment 75
6.5. Raman spectrum of carbon nanofibers after low O_2-flow post-treatment 77
6.6. SEM images of carbon nanofibers after high and low O_2-flow post-treatment. 78
6.7. Ar isotherms on carbon nanofibers treated at high and low O_2-flow post-treatment 79
6.8. CO_2 adsorption isotherms and pore size distribution of carbon nanofibers treated at low and high O_2-flow post-treatment 80
6.9. Isosteric enthalpy of adsorption and adsorption kinetics of CO_2 on carbon nanofibers treated at high and low O_2-flow post-treatment 82
6.10. TGA-DSC results for various carbon reference materials 84
6.11. Comparison of inhouse carbon nanofibers to commercial nanofibers . . 85

7.1. SEM images of KOH-activated carbon nanofiber pellets 88
7.2. Elemental composition of KOH-activated carbon nanofibers at different KOH:Fiber ratios 89
7.3. Ar isotherms on KOH-activated carbon nanofibers 90
7.4. Pore size distribution of KOH-activated carbon nanofibers based on DFT calculations 91
7.5. CO_2 adsorption isotherms at 273 K on KOH-activated carbon nanofibers 92
7.6. Pore size distribution of KOH-activated carbon nanofibers based on Monte-Carlo calculations and isosteric enthalpy of adsorption 94
7.7. H_2O adsorption isotherms at 298 K on KOH-activated carbon nanofibers 96

8.1. CO_2 and N_2 isotherms at 298 K for KOH-activated carbon nanofibers . . 98
8.2. Toth isotherm fits of CO_2 and N_2 adsorption isotherms 100
8.3. IAST CO_2/N_2 selectivity values for a binary CO_2/N_2 mixture on KOH-activated carbon nanofibers 100
8.4. Breakthrough curves of CO_2 and N_2 in a binary CO_2/N_2 mixture 102
8.5. Experimental CO_2/N_2 selectivity and comparison of the selectivity to reference materials 104
8.6. Comparison of IAST and experimental selectivities on KOH-activated carbon nanofibers 105
8.7. High pressure N_2 adsorption isotherm up to 10 bar 106
8.8. Ideal working capacity of the adsorbent and scheme of a simplified PSA cycle 108
8.9. Working capacity of the adsorbent in a simplified PSA cycle 109

A.1. Raman spectra of the D and G band region of carbon nanofibers stabilized at different temperatures 134
A.2. Raman spectra of the D and G band region of carbon nanofibers stabilized at different durations 135
A.3. Calcium oxalate monohydrate calibration of the mass spectrometer . . . 137

List of Tables

4.1. Investigated stabilization parameters 29
4.2. Electrospinning parameters on IME electrospinner 30
4.3. Overview on reference materials used for investigations discussed in chapter 6. 32
4.4. Overview on used adsorptives 35
4.5. Parameters of breakthrough experiments 38

5.1. Pore size distribution and BET area of carbon nanofibers stabilized at different durations 49
5.2. BET area and pore size distribution of carbon nanofibers stabilized at 200, 225, 250, 275 and 300 °C 57
5.3. BET area and pore size distribution of carbon nanofibers stabilized in air compared to in N_2 65

6.1. Elemental composition of carbon nanofibers treated at high and low O_2-flow post-treatment 75
6.2. BET area and pore size distribution on carbon nanofibers treated at high and low O_2-flow post-treatment 79

7.1. BET area and pore size distribution of KOH-activated carbon nanofibers at different activation ratios 93

8.1. Toth isotherm fit parameters used for IAST calculations 99
8.2. Necessary pressures to obtain equal spreading pressures on both adsoption isotherms 105

A.1. Potassium content of KOH-activated carbon nanofibers 133
A.2. Raman fit data for variation of the duration during thermal stabilization . 136
A.3. Raman fit data for variation of the temperature during thermal stabilization 136
A.4. Ion fragmentation of CO_2 in mass spectrometry 137